UNRAVELING THE ROLE OF HYDROGEN INSERTION IN ENHANCING ELECTROCHEMICAL PERFORMANCE OF VANADIUM PENTOXIDE CATHODE FOR MAGNESIUM-ION BATTERIES: A FIRST-PRINCIPLES STUDY

PANUPOL UNTARABUT

มหาวิทยาลัยเทคโนโลยีสุรนารี

A Thesis Submitted in Partial Fulfillment of the Requirements for the
Degree of Master of Science in Physics
Suranaree University of Technology
Academic Year 2023

การศึกษาบทบาทของการแทรกไฮโดรเจนในการเพิ่มประสิทธิภาพทางเคมีไฟฟ้าของแคโทดวาเนเดียมเพนทอกไซด์ สำหรับแบตเตอรีชนิดแมกนีเซียมไอออน โดยวิธีเฟิร์สท์พรินซิเพิล

นายภาณุพล อันทรบุตร

มหาวิทยาลัยเทคโนโลยีสุรนารี

วิทยานิพนธ์นี้เป็นส่วนหนึ่งของการศึกษาตามหลักสูตรปริญญาวิทยาศาสตรมหาบัณฑิต
สาขาวิชาฟิสิกส์
มหาวิทยาลัยเทคโนโลยีสุรนารี
ปีการศึกษา 2566

UNRAVELING THE ROLE OF HYDROGEN INSERTION IN ENHANCING ELECTROCHEMICAL PERFORMANCE OF VANADIUM PENTOXIDE CATHODE FOR MAGNESIUM-ION BATTERIES: A FIRST-PRINCIPLES STUDY

Suranaree University of Technology has approved this thesis submitted in partial fulfillment of the requirements for a Master's Degree.

Thesis Examining Committee

(Dr. Anchalee Junkaew)
Chairperson

(Assoc. Prof. Dr. Suwit Suthirakun)
Member (Thesis Advisor)

(Dr. Ittipon Fongkaew)
Member (Thesis Co-Advisor)

(Assoc. Prof. Dr. Sirichok Jungthawan)
Member

(Assoc. Prof Dr. Kamonwad Ngamchuea)
Member

(Assoc. Prof. Dr. Yupaporn Ruksakulpiwat)
Vice Rector for Academic Affairs
and Quality Assurance

(Prof. Dr. Santi Maensiri)
Dean of the Institute of Science

มหาวิทยาลัยเทคโนโลยีสุรนารี

ภาณุพล อันทรบุตร : การศึกษาบทบาทของการแทรกไฮโดรเจนในการเพิ่มประสิทธิภาพทางเคมีไฟฟ้าของแคโทดวาเนเดียมเพนทอกไซด์ สำหรับแบตเตอรีชนิดแมกนีเซียมไอออน โดยวิธีเฟิร์สท์พรินซิเพิล (UNRAVELING THE ROLE OF HYDROGEN INSERTION IN ENHANCING ELECTROCHEMICAL PERFORMANCE OF VANADIUM PENTOXIDE CATHODE FOR MAGNESIUM-ION BATTERIES: A FIRST-PRINCIPLES STUDY)
อาจารย์ที่ปรึกษา : รองศาสตราจารย์ ดร.สุวิทย์ สุธีรากุล, 111 หน้า.

คำสำคัญ: อิเล็กโทรไลต์ที่เป็นน้ำ วาเนเดียมเพนทอกไซด์ ทฤษฎีฟังก์ชันนอลความหนาแน่น การคำนวณหลักการแรก แบตเตอรีชนิดแมกนีเซียมไอออน การแทรกไฮโดรเจน

วิทยานิพนธ์นี้ได้ดำเนินการคำนวณโดยวิธีหลักการแรก อาศัยระเบียบวิธีทฤษฎีฟังชันนอลความหนาแน่น เพื่อศึกษาผลกระทบของการแทรกไฮโดรเจน ต่อการนำไฟฟ้า จลนศาสตร์การแพร่กระจายของแมกนีเซียม และความเสถียรของโครงสร้างตามการแทรกสอดของแมกนีเซียม ในโครงสร้างขั้วไฟฟ้าแคโทดแบบวาเนเดียมเพนทอกไซด์ ผลลัพธ์แสดงให้เห็นว่าการแทรกไฮโดรเจน ที่ความเข้มข้นสูงในโครงสร้างวาเนเดียมเพนทอกไซด์ ทำให้ช่องว่างของแถบพลังงานลดลงอย่างเห็นได้ชัด และค่าการนำไฟฟ้าทางอิเล็กทรอนิกส์ของวัสดุวาเนเดียมเพนทอกไซด์เพิ่มขึ้นอย่างมาก โดยไฮโดรเจนที่ใส่เข้าไปสามารถทำหน้าที่เป็นตัวพาประจุ ซึ่งช่วยเพิ่มความจุของแคโทดได้อย่างมีประสิทธิภาพ จลนพลศาสตร์ของการแพร่ของไฮโดรเจน นั้นเร็วกว่ามากเมื่อเทียบกับแมกนีเซียม ในระหว่างการคายประจุ คาดว่าแคโทดจะมีความเข้มข้นสูงของไฮโดรเจน ก่อนการแทรกแมกนีเซียม โครงสร้างไฮโดรเจนที่ใส่ไว้ล่วงหน้าจะช่วยเร่งการแพร่กระจายของแมกนีเซียม โดยการลดอุปสรรคการแพร่จาก 0.93 เป็น 0.23 eV นอกจากนี้ แคโทดวาเนเดียมเพนทอกไซด์ที่ถูกโปรตอนเติมเต็มจะยับยั้งการเปลี่ยนเฟสแอลฟาเป็นเฟสเดลตา ซึ่งเป็นเฟสที่ไม่สามารถย้อนกลับได้ อย่างมีประสิทธิภาพ ซึ่งถือเป็นสาเหตุหลักของความจุที่ลดลงในแบตเตอรี จลนพลศาสตร์การขนส่งไอออนที่ดีขึ้นและการยับยั้งการเปลี่ยนเฟสเกิดขึ้นจากปฏิกิริยาระหว่างไฟฟ้าสถิตที่อ่อนลงระหว่างแมกนีเซียมไอออน และวาเนเดียมเพนทอกไซด์ เมื่อแทรกไฮโดรเจน การค้นพบที่สำคัญเหล่านี้ให้ข้อมูลเชิงลึกที่มีคุณค่าสำหรับการออกแบบกลยุทธ์เพื่อเพิ่มประสิทธิภาพทางเคมีไฟฟ้าของแคโทดวาเนเดียมเพนทอกไซด์ในแบตเตอรีชนิดแมกนีเซียมไอออน

สาขาวิชาฟิสิกส์ ลายมือชื่อนักศึกษา ภาณุพล.
ปีการศึกษา 2566 ลายมือชื่ออาจารย์ที่ปรึกษา สุวิทย์ สุธีรากุล
ลายมือชื่ออาจารย์ที่ปรึกษาร่วม อิทธิพล

PANUPOL UNTARABUT : UNRAVELING THE ROLE OF HYDROGEN INSERTION IN ENHANCING ELECTROCHEMICAL PERFORMANCE OF VANADIUM PENTOXIDE CATHODE FOR MAGNESIUM-ION BATTERIES: A FIRST-PRINCIPLES STUDY.
THESIS ADVISOR : ASSOC. PROF. SUWIT SUTHIRAKUN, Ph.D. 111 PP.

Keyword: Aqueous electrolyte, Vanadium pentoxide, density functional theory, first principles calculation, Magnesium-ion batteries, Hydrogen insertion

In this thesis, we conducted first-principles computations to study the effects of hydrogen (H) insertion on electronic conductivity, magnesium (Mg) diffusion kinetics, and structural stability upon Mg intercalation. Our findings demonstrate that the insertion of H at high concentrations leads to a remarkable reduction in the band gap and a substantial increase in the electronic conductivity of the vanadium pentoxide (V_2O_5) material. This inserted H can act as a charge carrier, effectively enhancing the cathode's capacity. Moreover, we observed that the transport kinetics of H are significantly faster compared to Mg. During discharge, it is expected that the cathode will contain a high concentration of H before Mg intercalation. The pre-inserted H structure accelerates the Mg diffusion by lowering the diffusion barrier from 0.93 to 0.23 eV. Additionally, a fully protonated V_2O_5 cathode effectively suppresses the irreversible alpha to delta phase transition, which is considered the main cause of capacity fading in these batteries. The improved ion transport kinetics and the suppression of phase transformation arise from the weakened electrostatic interaction between the Mg-ion and the lattice oxygen upon H insertion. These significant findings provide valuable insights for the rational design of strategies to enhance the electrochemical performance of V_2O_5 cathodes in Mg-ion batteries. By leveraging this knowledge, we can move closer to unlocking the full potential of Mg-ion batteries as a promising energy storage solution.

School of Physics
Academic Year 2023

Student's Signature ภานุพล .
Advisor's Signature สุวิทย์ สุธีรกุล
Co-Advisor's Signature

ACKNOWLEDGEMENTS

I am deeply grateful to my thesis advisor, Asst. Prof. Dr. Suwit Suthirakun, and co-advisors, Dr. Anchalee Junkaew and Dr. Ittipon Fongkaew, for their unwavering patience, kind support, invaluable guidance, stimulating discussions, and continuous encouragement throughout my thesis journey. Their expertise and dedication have been instrumental in shaping the success of this research. I would like to extend my heartfelt appreciation to Assoc. Prof. Dr. Sirichok Jungthawan and Dr. XXX XXX for generously contributing their time and expertise as members of the thesis-examining committees. Furthermore, I am deeply grateful to the Development and Promotion of Science and Technology Talents Project (DPST, THAILAND) for awarding me the scholarship that made pursuing my master's degree program possible. This research and innovation activity has been made possible through generous financial support from the National Research Council of Thailand (NRCT) and Suranaree University of Technology (SUT). Their support has been indispensable in carrying out this study. I am also thankful to the NSTDA Supercomputer Center (ThaiSC) and the Institute of Science, Suranaree University of Technology, for providing access to computational resources, which were vital for the success of this research. I extend my sincere appreciation to the faculty and staff of the School of Physics, Institute of Science, Suranaree University of Technology, for their guidance, camaraderie, and encouragement throughout my academic journey. Special thanks go to Sirisak Singsen and Lappawat Ngamwongwan for their valuable time spent teaching and offering invaluable suggestions on computational techniques. I am equally grateful to my friends in the Computational Materials Science and Catalysis (COMSCAT) Group for their support, collaboration, and friendship. Lastly, none of this would have been possible without the unwavering love, kind support, and encouragement of my family. Their constant presence and belief in me have been my source of strength and motivation.

Panupol Untarabut

CONTENTS

Page

ABSTRACT IN THAI I

ABSTRACT IN ENGLISH II

ACKNOWLEDGEMENTS III

CONTENTS IV

LIST OF TABLES VII

LIST OF FIGURES VIII

LIST OF ABBREVIATIONS XIII

CHAPTER

I INTRODUCTION 1

1.1 Magnesium-ion batteries 1

1.2 Vanadium pentoxide (V_2O_5)-based cathode materials 7

1.3 Aqueous electrolytes 11

1.4 Research objectives 13

1.5 Scope and limitations 14

1.6 References 15

II CALCULATION DETAILS 21

2.1 Schrödinger equation for many particles problem 21

2.2 Variational principle 23

2.3 Hartree approximation 24

2.4 Hartree-Fock approximation 25

2.5 Density functional theory 26

2.5.1 The Hohenberg-Kohn theorems 26

2.5.2 The Kohn-Sham equation 27

2.5.3 Exchange-correlation functional 29

2.5.4 Pseudopotential 31

2.5.5 Self-Consistent Field approach 34

CONTENTS (Continued)

Page

2.6 Geometry optimization 35
2.7 DFT+U 38
2.8 vdW correction 39
2.9 Climbing image nudged elastic band method 40
2.10 Ab initio molecular dynamics 42
2.11 Open circuit voltage calculation 44
2.12 Summary of computational details 45
2.13 References 46

III STRUCTURAL AND ELECTRONIC PROPERTIES OF V_2O_5 49

3.1 Crystal Structure of α-V_2O_5 49
3.2 Electronic properties 51
3.3 References 53

IV THE INSERTION OF HYDROGEN AND MAGNESIUM INTO V_2O_5 55

4.1 H Intercalation in V_2O_5 55
4.2 Effect of H Concentration on $H_xV_2O_5$ 59
4.3 Thermal Stability Investigation of $H_2V_2O_5$ Structure 67
4.4 Mg Intercalation in V_2O_5 69
4.5 References 74

V DIFFUSION KINETICS OF ION MIGRATION IN V_2O_5 CATHODE 75

5.1 Kinetics of H Diffusion in V_2O_5 Cathode 75
5.2 Kinetics of Mg Diffusion in V_2O_5 Cathode 78
5.3 Effect of H Insertion on Mg Diffusion Kinetics 82
5.4 References 85

VI EFFECT OF HYDROGEN INSERTION ON THE STRUCTURAL STABILITY 87

6.1 Influence of H Insertion on Structural Stability 87
6.2 The effect of H Insertion on the Discharge Voltage Profiles 90

CONTENTS (Continued)

Page

6.3 References....93

VII CONCLUSIONS....95

APPENDIX....97

CURRICULUM VITAE....111

มหาวิทยาลัยเทคโนโลยีสุรนารี

LIST OF TABLES

Table **Page**

2.1 Assorted constants for PZ correlation energy calculations.....29

3.1 Lattice parameters and V-O bond distances of α-V_2O_5 obtained from experimental characterizations and computations (values in angstroms unit).....50

3.2 Calculated band gaps of α-V_2O_5 using different methods.....52

6.1 Compared OCV value of low Mg concentration in V_2O_5-based cathode.....92

มหาวิทยาลัยเทคโนโลยีสุรนารี

LIST OF FIGURES

Figure **Page**

1.1 Operational mechanism of rechargeable batteries: red, blue, and brown arrows depict electron, current, and ion movements respectively, Illustrated for (a) Discharge Cycle and (b) Charging Cycle.....3

1.2 Distribution of chemical element abundance (atom fraction) in Earth's upper continental crust as a function of atomic number.....5

1.3 Comparison of cathode material performance in Li-ion and Mg-ion batteries. (a) Discharge profile on graphene-based cathode for Li-ion and Mg-ion batteries. Charge and discharge profiles on MnO_2-baed cathode for (b) Li-ion and (c) Mg-ion batteries. (d) Rate performance on V_2O_5-based cathode for Mg-ion batteries.....6

1.4 The synthesized V_2O_5 presented as (a) TEM image, (b) HRTEM image and (c) SAED pattern (d) Structural model of V_2O_5 with red spheres representing oxygen atoms and grey spheres representing vanadium atoms.....8

1.5 Cycling characteristics of the V_2O_5 electrode demonstrating repeated cycles between 2.5 and 4.0 V vs. Li/Li^+. (a) Galvanostatic cycling response. (b) Successive cycling at varied specific currents.....9

1.6 Galvanostatic cycling of α-V_2O_5 versus carbon coin cell in a 1 M Mg(TFSI)2/G2 electrolyte at 20 $mAcm^{-2}$ under two different water concentrations: (a) 2600 ppm H_2O and (b) 15 ppm H_2O.....11

1.7 (a) X-ray diffraction pattern of $H_xV_2O_5$. (b) Structure of $H_xV_2O_5$. (c) Galvanostatic charge-discharge (GCD) curves of $H_xV_2O_5$ at 0.1 Ag^{-1}. (d) GCD curves of $H_xV_2O_5$ at different current densities. (e) Energy barrier for Zn^{2+} diffusion in $H_xV_2O_5$.....13

2.1 Contrast between wavefunctions in nuclear coulomb potential (blue) and pseudopotential (red).....32

LIST OF FIGURES (Continued)

Figure **Page**

2.2 The schematic of self-consistency iteration for solving the Kohn-Sham equation and determining the calculated total energy and other properties.....34

2.3 The schematic of optimization in DFT calculations.....37

2.4 Schematic of the potential energy surface (PES) and NEB Calculation. White and black lines denote the initial guess and optimized reaction pathways.....41

3.1 Illustrations of (a) VO_5 units, each containing three distinct oxygen atoms denoted as follows: vanadyl oxygen (O1), bridging oxygen (O2), and edge-sharing oxygen (O3) with the bond distance presented in Å unit and (b) an α-V_2O_5 supercell in a 1x2x2 arrangement. The red and grey represent the oxygen and vanadium atom.....50

3.2 (a) The projected density of states and (b) energy band structure of V_2O_5 structure show a non-magnetic semiconducting character with an indirect band gap of 2.17 eV. The red and gray solid lines represent the state of oxygen and vanadium, respectively.....51

4.1 Representation of various hydrogen insertion configurations in V_2O_5.....56

4.2 Demonstration of minor distortion of a VO_5 unit, accompanied by electron localization at the V center, commonly referred to as a small polaron. The labeled numbers correspond to their respective bond distances in angstrom. The yellow isosurface at 0.032 e $Å^{-3}$ highlights the electron localization.....57

4.3 A visual representation of a gap state within both the projected density of states and the band structure for the $HV_{16}O_{40}$ structure.....58

LIST OF FIGURES (Continued)

Figure **Page**

4.4 The density of state (DOS) of V_2O_5 before and after H insertion. the total DOS was show in gray filled color and the partial DOS projecte on s, p and d state of V atom was represented in red, green and blue solid line, respectively.....59

4.5 The formation energy profile of H insertion into V_2O_5.....60

4.6 Illustratration of the impact of varying hydrogen content on the local structures of α-V_2O_5, focusing on V-O bond lengths, O1-O1' distances, and V-V' distances in the [100] direction, as well as H-O1 bond lengths.....62

4.7 (a) The electronic structures in the projected density of states of HxV_2O_5 structure. It is evident that increasing hydrogen content leads to a reduction in band gaps. (b) The additional electrons resulting from the inserted hydrogen occupy V centers, creating states located at the uppermost portion of the valence band. This phenomenon is visually represented by the yellow isosurface at 0.032 e $Å^{-3}$.....64

4.8 The polaron localized at each V_2O_5 layer for (a) $H_{0.125}V_2O_5$, (b) $H_{0.25}V_2O_5$, and (c) $H_{0.25}V_2O_5$. The projected density of states of (d) $H_{0.125}V_2O_5$, (e) $H_{0.25}V_2O_5$, and (f) $H_{0.25}V_2O_5$. the gray, red, and white colors represented vanadium, oxygen, and hydrogen, respectively.....66

4.9 (a) The thermal stability investigation in total energy evolution using AIMD simulation at 300K, 600K and 900K. (b) The RDF of the O-H bond in $H_2V_2O_5$ at the last time frame for 300K, 600K and 900K. The blue, orange, and green line represented for 300K, 600K and 900K, respectively.....68

4.10 Electron localized configuration for Mg insertion into $V_{16}O_{40}$. (a) two configurations of electron localized. (b) total energy of each configuration. (c) bond distance of V-O in Å unit of the most stable configuration.....69

LIST OF FIGURES (Continued)

Figure **Page**

4.11 Sketches of Mg Insertion and its Impact on α-V_2O_5. (a) Depicts the local structure after Mg insertion into α-V_2O_5. Upon insertion, Mg ionizes and generates two polarons at neighboring VO_5 units, represented by the yellow isosurface. (b) Shows the corresponding gap states in the projected density of states resulting from the formation of these polarons. (c) Demonstrates the effect of high Mg concentrations on the α-V_2O_5 phase transition, as characterized by the puckering angle of O1-O2-O1. (d) Displays how the puckering angle decreases with increasing Mg concentration. (e) Depicts the structural transformation from the α-phase to the α-phase as a consequence of Mg insertion.....71

4.12 Density of state of $Mg_yV_{16}O_{40}$ (y=2,4,6 and 8). The red, grey and green line represented oxygen, vanadium and magnesium state.....73

5.1 The Schematic of H and polaron separated migration configuration. (a) The proton diffusion preceding polaron transfer and (b) polaron transfer preceding proton diffusion. The white sphere represented H atom and yellow isosurface represented polaron localized.....76

5.2 Energy profile of H and polaron migration in the α-V_2O_5 structure, involving three migration configurations: (a) H-coupled polaron transfer, (b) H Migration preceding polaron transfer, and (c) polaron transfer preceding H Migration. The insets schematically depict the sequence of migration events, where the α-V_2O_5 structure is represented by squares, H by cyan circles, and polarons by yellow diamonds.....77

5.3 The possible Mg migration pathway in V_2O_5 structure. (a) P1, P2 and P3 represented the Mg migration pathway in [010], [110] and [001], respectively. (b) minimum energy pathway of Mg migration.....78

LIST OF FIGURES (Continued)

Figure **Page**

5.4 The ion and polaron migration configuration of one Mg and two polarons migration. (a) Mg diffusion preceding two polaron transfer, (b) one polaron transfer preceding Mg diffusion and (c) two polaron transfer preceding Mg diffusion. The red, green and grey sphere represented oxygen, magnesium and vanadium, respectively. The yellow isosurface at 0.032 e $Å^{-3}$ highlights the polaron localization.....80

5.5 Energy Profile of Mg-Two-Polaron Migration: (a) Coupled Migration of Mg and Two Polarons, (b) Sequential Mg Migration Followed by Polaron Migration, (c) Mg Migration Following a Single Polaron Migration, and (d) Mg Migration After Two Polaron Migrations. The accompanying diagrams provide a visual depiction of the migration sequence, where squares denote the α-V_2O_5 structure, green circles represent Mg, and yellow diamonds depict polarons.....81

5.6 (a) Energy profiles for Mg diffusion along the [010] direction in V_2O_5 and $H_2V_2O_5$. (b) Transition state structures for Mg diffusion in the protonated variants with noticeable relaxation, resulting in longer Mg–O Distances. The annotated bond distances are presented in angstroms.....83

5.7 O-environmental atom during Mg migration in V_2O_5 and $H_2V_2O_5$. IS, TS and FS represent initial, transition and final state, respectively.....84

6.1 (a) Conceptual representation depicting the characterization of the α to δ phase transition through puckering and layered angles. The correlation between intercalated Mg concentrations and (b) puckering as well as (c) layered angles. The introduction of hydrogen prevents the α–δ phase transition.....88

6.2 Voltage profile of $H_xV_2O_5$ during Mg insertion. The blue, orange and green line represented the voltage profile of $H_xV_2O_5$-based cathode where x=0, 1 and 2, respectively.....91

LIST OF ABBREVIATIONS

H	= Hydrogen
Li	= Lithium
Mg	= Magnesium
CV	= Current-voltage
MIB	= Mg-ion batteries
HRTEM	= High-resolution transmission electron microscopy
TEM	= Transmission electron microscopy
SAED	= Selected area electron diffraction
ORR	= Oxygen reduction reaction
HER	= Hydrogen evolution reaction
DFT	= Density functional theory
AIMD	= Ab-initio molecular dynamics
VASP	= Vienna ab initio simulation package
GGA	= Generalized gradient approximation
PDOS	= Projected density of states
XPS	= X-ray photoelectron spectra
LDA	= Local density approximation
PAW	= Projector-augmented wave
PBE	= Perdew-Burke-Ernzerhof
CI-NEB	= Climbing image-nudged elastic band
MEP	= Minimum energy pathway
TS	= Transition state
XC	= Exchange-correlation
VBM	= Valence band maximum
CBM	= Conduction band minimum
NEB	= Nudged elastic band
MD	= Molecular dynamics

มหาวิทยาลัยเทคโนโลยีสุรนารี

CHAPTER I
INTRODUCTION

1.1 Magnesium-ion batteries

Global civilization's increasing energy consumption, driven by population growth, urbanization, and industrialization, demands the ongoing development of efficient energy devices. Moreover, the implications of this increasing energy consumption on the environment cannot be ignored. Fossil fuel combustion (Gurney et al., 2009), a primary source of electricity generation, releases greenhouse gases (Shen et al., 2020), contributing to climate change and its subsequent adverse effects on the planet. As a result, there is a global responsibility to transition towards clean and renewable energy sources, including solar (Kannan et al., 2016), wind (Joselin Herbert et al., 2007), hydroelectric (Sims, 1991), and nuclear power (Abu-Khader, 2009), to mitigate the impact on the environment and ensure a sustainable energy future. In this transition, energy storage becomes vital. We need good energy storage devices, like rechargeable batteries, to keep our energy supply stable and dependable. Several energy storage technologies are currently in use, such as rechargeable batteries (J. B. Goodenough et al., 2013), thermal energy storage (Alva et al., 2018), fuel cells (Nørskov et al., 2004) and compressed air energy storage (Lund et al., 2009), among others. Among these options, rechargeable batteries have gained widespread popularity due to their lightweight, compact size, and high energy density when compared to other alternatives (John B. Goodenough, 2012).

Rechargeable batteries, notably lithium-ion batteries, have transformed modern life by providing power to an extensive array of portable electronic devices, including smartphones, laptops, and tablets. These rechargeable batteries comprise four essential components:

(1) Electrode: Comprising both a cathode and anode, the electrode plays a pivotal role in the battery's operation.

(2) Separator: Serving as a barrier, the separator ensures that the cathode and anode do not come into direct contact, thus preventing short-circuits.

(3) Electrolyte: This critical component consists of an ion-conducting solution that permits ion migration while blocking the flow of electrons.

(4) Current Collector: The current collector facilitates the flow of electrons through the external electrical circuit, allowing the battery to discharge and charge effectively.

The functioning of rechargeable batteries hinges on electrochemical reactions, which are divided into two main processes: charge and discharge.

In the discharge process, as illustrated in Figure 1.1(a), a spontaneous reaction occurs. Cations migrate from the anode materials and intercalate into the cathode materials, while electrons flow through the external circuit into the anode materials. This process is activated when an electronic device is in use.

Conversely, during the charge process, depicted in Figure 1.1(b), an external voltage is applied to the battery, inducing chemical reactions within. Cations exit the cathode materials, traversing through the electrolyte and separator, before intercalating into the anode materials. Simultaneously, electrons must flow from the cathode materials to the anode materials through the external circuit to maintain charge equilibrium. This process takes place when there is a need to store electrical power in the batteries.

มหาวิทยาลัยเทคโนโลยีสุรนารี

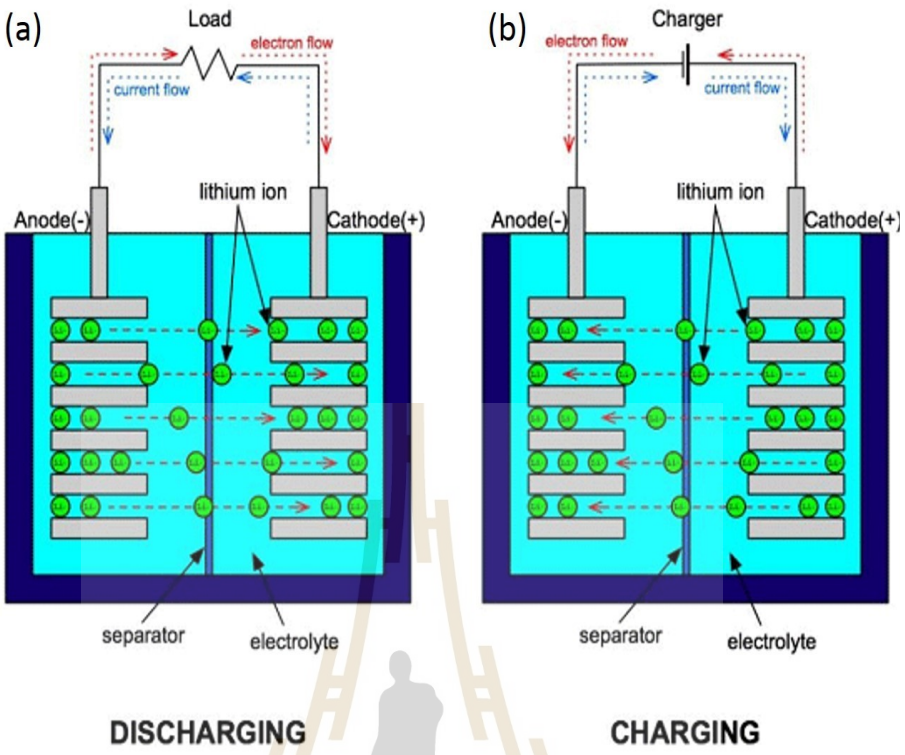

Figure 1.1 Operational mechanism of rechargeable batteries: red, blue, and brown arrows depict electron, current, and ion movements respectively, Illustrated for (a) Discharge Cycle and (b) Charging Cycle (J. B. Goodenough et al., 2013).

Rechargeable batteries have become the preferred choice for applications where size and weight constraints are crucial, because of compact design and high energy storage capacity. As the demand for high-performance rechargeable batteries continues to surge in the field of renewable energy storage, magnesium-ion batteries have emerged as promising candidates, offering potential advantages over conventional lithium-ion batteries (Massé et al., 2015).

Magnesium-ion batteries (Mg-ion batteries or MIBs) have emerged as a promising alternative that has the potential to replace traditional lithium-ion batteries. Compared to lithium-ion cells, Mg-ion batteries have a superior specific capacity of around 2000 $mAhg^{-1}$ and a volumetric capacity of ~3800 $mAhmL^{-1}$. These findings are supported by studies conducted by Shah et al. (Shah et al., 2021) and You et al. (You et al., 2020). This increased capacity allows Mg-ion batteries to store more energy within the same

volume and weight constraints, making them an interesting choice for various applications.

When we explore the electrochemical details of Mg-ion batteries, it becomes clear that Li undergoes an oxidation process during operation. This process leads to the generation of Li^+ ions and the release of a single electron. On the other hand, Mg atoms exhibit a divalent nature, giving rise to Mg^{2+} ions and the release of two electrons as part of their electrochemical transformation. The fundamental difference between Li and Mg is magnesium's higher electron count per cation. This unique characteristic enhances the volumetric capacity of Mg-ion batteries (MIBs) when compared to their lithium-ion batteries. This advantage further solidifies the appeal of MIBs in the field of advanced energy storage technologies, especially as the need for higher capacity and more sustainable battery solutions continues to rise.

$$Li \longrightarrow Li^+ + e^- \quad (1.1)$$

$$Mg \longrightarrow Mg^{2+} + 2e^- \quad (1.2)$$

One of the most notable advantages of Mg-ion batteries is their enhanced safety profile, a crucial factor for the widespread adoption of energy storage technologies. These batteries exhibit remarkable safety characteristics, reducing the risk of fire or explosion during charging and discharging processes (Davidson et al., 2018; Y. Zhao et al., 2022). This safety aspect gains utmost significance, particularly in applications where safety is a top priority, such as in electric vehicles and grid energy storage systems. Moreover, the abundance of magnesium sources presents a notable advantage, as shown in Figure 1.2, ensuring a steady and reliable supply for battery production (Bae et al., 2021; Pavčnik et al., 2021). Unlike lithium, which is often extracted from limited sources, magnesium can be sourced from various locations, making Mg-ion batteries a more sustainable and environmentally friendly option.

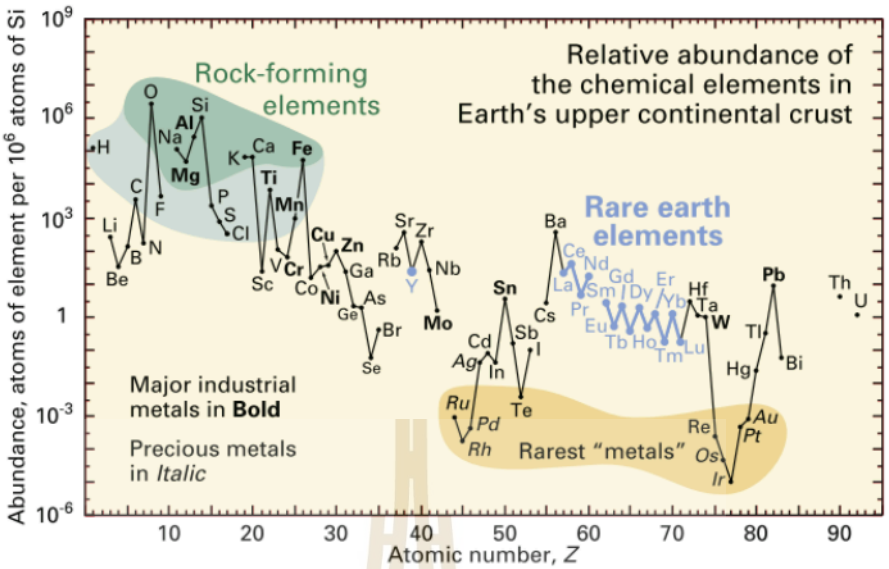

Figure 1.2 Distribution of chemical element abundance (atom fraction) in Earth's upper continental crust as a function of atomic number (Massé et al., 2015).

The comparison of cathode material performance in Li-ion and Mg-ion batteries is depicted in Figure 1.3. In the case of MoO_3-based cathodes for Li-ion batteries, the discharge voltage, capacity, and retention are observed to be 2.4 V, 65 $mAhg^{-1}$, and 92%, respectively, after 15 cycles (Huie et al., 2015). In contrast, for Mg-ion batteries, these cathodes exhibit a higher discharge voltage of 2.8 V, a greater capacity of 143 $mAhg^{-1}$, but a reduced retention of 50% after 300 cycles (Jiang et al., 2017). When examining V_2O_5-based cathodes for Li-ion batteries, they demonstrate a discharge voltage of 2.3 V, a capacity of 147 $mAhg^{-1}$, and a retention rate of 80% after 40 cycles (Rashad et al., 2020). Comparatively, in Mg-ion batteries, the same cathodes provide a lower discharge voltage of 1.73 V, a higher capacity of 250 $mAhg^{-1}$, but a retention rate of 70% after 100 cycles (Rashad et al., 2020). These experimental findings suggest that, when comparing cathode materials for both Li-ion and Mg-ion batteries, Mg-ion systems offer a notable advantage in terms of capacity. However, they tend to exhibit a shorter lifecycle, as evidenced by the lower retention rates over a small number of charge-discharge cycles. This trade-off between capacity and cycling stability should be considered when selecting cathode materials for specific battery applications. Additional research into the electrochemical mechanisms underlying these

performance differences is needed to enhance the efficiency of both Li-ion and Mg-ion battery systems.

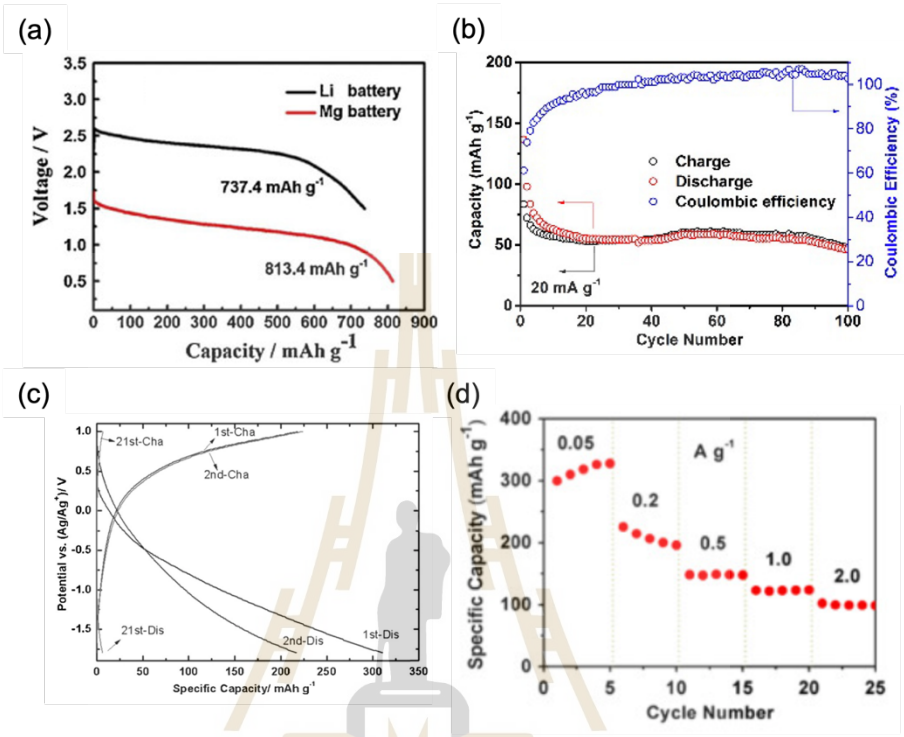

Figure 1.3 Comparison of cathode material performance in Li-ion and Mg-ion batteries. (a) Discharge profile on graphene-based cathode for Li-ion and Mg-ion batteries (Rashad et al., 2020). Charge and discharge profiles on MnO_2-based cathode for (b) Li-ion and (c) Mg-ion batteries (Huie et al., 2015; Jiang et al., 2017). (d) Rate performance on V_2O_5-based cathode for Mg-ion batteries (Rashad et al., 2020).

However, several challenges must be addressed for Mg-ion batteries to reach their full potential. A critical issue pertains to the interaction between divalent Mg^{2+} ions and the host cathode material. The strong interaction between these ions and the cathode poses hindrances to charge transport kinetics, resulting in slower charging and discharging rates (Tian et al., 2017). Additionally, the low ion utilization further limits overall battery performance.

To overcome these challenges and enhance the performance of Mg-ion batteries, researchers are exploring suitable cathode materials that exhibit a moderate interaction with Mg-ions. Finding the right cathode materials is instrumental in

improving charge transport kinetics and increasing ion utilization, thereby enhancing the battery's overall efficiency and energy storage capabilities.

In conclusion, Mg-ion batteries exhibit significant promise as an alternative to conventional Li-ion cells, with superior specific and volumetric capacities, enhanced safety features, and the advantage of abundant magnesium sources. Nonetheless, unlocking their full potential necessitates dedicated research efforts to identify cathode materials that can mitigate the strong interaction between Mg^{2+} ions and the cathode, propelling improved battery performance and broader adoption of this promising energy storage technology. To optimize the performance of Mg-ion batteries, a crucial focus lies on the choice of cathode materials, with V_2O_5 emerging as a promising candidate due to its unique properties and potential to enhance the overall electrochemical performance of these advanced battery systems.

1.2 Vanadium pentoxide-based cathode materials

Vanadium pentoxide (V_2O_5) has emerged as a promising cathode material for various metal-ion batteries, including magnesium-ion batteries (Andrews et al., 2018; Murata et al., 2019; Zhang et al., 2017). The synthesis of V_2O_5 materials involves a wide range of methods. For example, the polyol-assisted solvothermal method, accompanied by thermal treatment at 500 °C, has been employed to achieve controlled formation of V_2O_5 nanorods. This synthetic strategy leverages solvothermal conditions and the reduction of the vanadium precursor within the presence of a polyol and a reducing agent (Umeshbabu et al., 2016).

As elucidated in Figure 1.4(a), transmission electron microscopy (TEM) imagery reveals the distinctive nanorod morphology characteristic of synthesized V_2O_5. Furthermore, high-resolution transmission electron microscopy (HRTEM) imagery, also depicted in Figure 1.4(b), provides detailed insights into the layered structure inherent to V_2O_5. The selected area electron diffraction (SAED) pattern of the synthesized V_2O_5, as shown in Figure 1.4(c), substantiates the single crystalline nature of the V_2O_5 nanorods. The layered structure of vanadium pentoxide, as exemplified in Figure 1.4(d), underscores its classification as a prototypical intercalation compound. This structural trait is pivotal to its suitability as a cathode material in metal-ion batteries, facilitating

the efficient insertion and extraction of ions during the charge and discharge processes. It is imperative to acknowledge that these findings contribute to the growing body of knowledge surrounding V_2O_5's potential utility in advancing metal-ion battery technology.

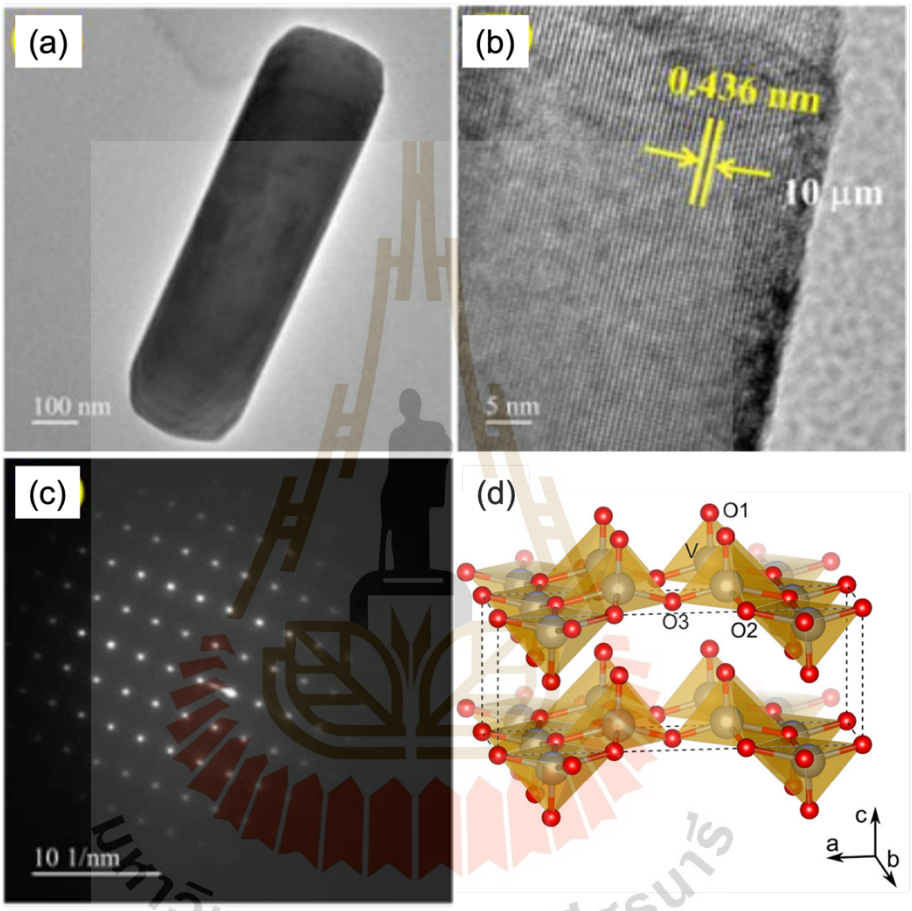

Figure 1.4 The synthesized V_2O_5 presented as (a) TEM image, (b) HRTEM image and (c) SAED pattern (Umeshbabu et al., 2016). (d) Structural model of V_2O_5 with red spheres representing oxygen atoms and grey spheres representing vanadium atoms. (Roginskii et al., 2021).

Researchers have explored its potential as it accommodates Mg ions, leading to the formation of $Mg_xV_2O_5$ compounds (Rocquefelte et al., 2003), which has shown favorable characteristics for energy storage applications. O The V2O5 cathode boasts a remarkable specific capacity of up to 427 $mAhg^{-1}$, a key advantage. Additionally, it exhibits a high Coulombic efficiency of 82% even after 2000 charge-discharge cycles

(Drosos et al., 2018), indicating its excellent reversibility and long-term stability as a cathode material. Figure 1.5 offer a deeper insight into the performance of V_2O_5 nanoparticle-based electrodes (S. Liang et al., 2014), a subject of considerable interest in the field. These figures display the electrode's remarkable capability to maintain a consistent specific capacity of 110 $mAhg^{-1}$ over the course of 100 charge-discharge cycles, all conducted at a current density of 100 mAg^{-1}. It is worth noting that the power performance of these materials exhibits an intriguing size-dependent behavior. When comparing nanostructured electrodes to their microstructure counterparts, the former exhibit superior rate capabilities. Even when subjected to the demanding rate of 20 ℃ (2000 mAg^{-1}), nanostructured electrodes deliver a specific capacity of approximately 100 $mAhg^{-1}$. These findings provide robust evidence that V_2O_5 nanoparticles reduce the diffusion length for Li^+ ions within the electrode material. Consequently, this reduction in diffusion length plays a pivotal role in the observed enhanced rate capabilities of V_2O_5 nanoparticles when compared to V_2O_5 microparticles. This observation underscores the critical role of nano structuring as a means to optimize the performance of V_2O_5-based materials in the context of energy storage applications.

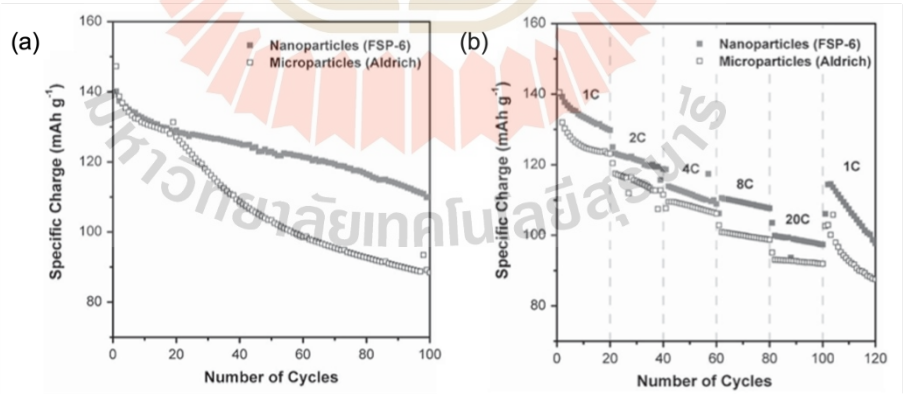

Figure 1.5 Cycling characteristics of the V_2O_5 electrode demonstrating repeated cycles between 2.5 and 4.0 V vs. Li/Li^+. (a) Galvanostatic cycling response. (b) Successive cycling at varied specific currents. (S. Liang et al., 2014).

However, despite these benefits, there are critical issues that need to be addressed to unlock the potential of V_2O_5 as a cathode material for Mg-ion batteries.

The primary challenge lies in the sluggish diffusion kinetics of magnesium ions within the V_2O_5 structure (Wang et al., 2017). Unlike lithium ions, magnesium ions face higher migration barriers, with a migration barrier of approximately 1.26 eV in α- V_2O_5, as opposed to the lower migration barriers of lithium (0.35 - 0.37 eV) in the same material (B. Zhou et al., 2014). This slower diffusion of Mg ions impacts the charging and discharging rates of the battery, leading to reduced overall performance. Furthermore, another critical problem associated with V_2O_5 as a cathode material is the capacity fading observed at high Mg contents. This capacity fading is caused by irreversible phase transformations occurring within the cathode during repeated cycling, resulting in a decline in the battery's capacity over time (X. Zhao et al., 2016). To overcome these challenges and improve the performance of V_2O_5-based cathodes for magnesium-ion batteries, further research and development efforts are necessary. Scientists are exploring various strategies, such as nano structuring the V_2O_5 material (Johnson et al., 2021), introducing dopants (Ngamwongwan et al., 2021), or using composite materials (J. Liu et al., 2009), to enhance the diffusion kinetics of magnesium ions within the cathode structure. These approaches aim to reduce the migration barriers for Mg ions and thereby improve the overall rate capability of the battery. Additionally, to address the issue of capacity fading, researchers are investigating ways to stabilize the V_2O_5 structure during repeated charge-discharge cycles. This involves designing cathode architectures and electrode formulations that can mitigate the irreversible phase transformations, ensuring better cyclability and longer battery lifetime.

In conclusion, V_2O_5 holds great promise as a cathode material for magnesium-ion batteries, offering a high specific capacity and good reversibility. However, the sluggish diffusion kinetics of magnesium ions and capacity fading due to irreversible phase transformations remain significant challenges. With ongoing research and innovative approaches, it is anticipated that these issues can be overcome, leading to further improvements in the performance of V_2O_5-based cathodes and advancing the development of efficient magnesium-ion battery technologies.

มหาวิทยาลัยเทคโนโลยีสุรนารี

1.3 Aqueous electrolytes

The addition of aqueous electrolytes has proven to be an effective strategy for enhancing the electrochemical properties of V_2O_5 cathodes in metal-ion batteries, including Mg-ion batteries (Karapidakis et al., 2021; Y. Liang et al., 2017; Wu et al., 2019). By incorporating a small amount of water into the electrolyte, the capacity and stability of the V_2O_5 cathode can be significantly improved, as supported by various experimental and computational studies. The research of Niya Sa (Sa et al., 2016) unveils a noteworthy breakthrough in achieving compatibility between Mg anodes and α-V_2O_5 cathodes. This compatibility is achieved through the utilization of magnesium bis (trifluoromethane sulfonyl) imide in diglyme electrolytes, albeit at notably low water levels. The electrolytes with higher water content fail to facilitate reversible Mg deposition. However, these electrolytes seem to provide enhanced capacities upon α-V_2O_5 cathodes, reaching approximately 300 $mAhg^{-1}$ and 20 $mAhg^{-1}$ for high and low water content, respectively, during the first cycle, as demonstrated in Figure 1.6.

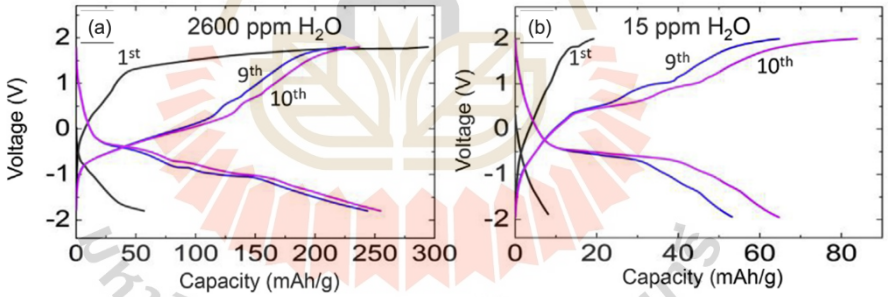

Figure 1.6 Galvanostatic cycling of α-V_2O_5 versus carbon coin cell in a 1 M $Mg(TFSI)_2$/G2 electrolyte at 20 $mAcm^{-2}$ under two different water concentrations: (a) 2600 ppm H_2O and (b) 15 ppm H_2O (Sa et al., 2016).

The precise role of water additives in the electrolyte has been the subject of extensive investigation. One proposed mechanism suggests that water can be inserted into the lattice of the V_2O_5 cathode, stabilizing its layered structure by forming a water pillar (Xu et al., 2019). This structural stabilization contributes to better performance and longer cycling life of the cathode. Recent research has put forth another explanation, indicating that water can dissociate at the electrode/electrolyte interface,

leading to the generation of H^+ ions and electrons (Kim et al., 2021; Park et al., 2020; Q. Zhao et al., 2020; L. Zhou et al., 2021). The dissociated H^+ ions and electrons then diffuse into the V_2O_5 structure, where they protonate lattice oxygen atoms, resulting in the formation of $H_xV_2O_5$. This formed $H_xV_2O_5$ compound acts as an intermediate during the charge-discharge process, improving the capacity of the cathode. Moreover, supporting experiments have confirmed the occurrence of water dissociation during the discharge process, leading to the alkalization of the electrolyte. The loss of H^+ ions and electrons upon insertion into the cathode further validates the proposed mechanism and highlights the importance of water as a critical component in the electrolyte to facilitate improved cathode performance (X. Liu et al., 2020). Recent computational studies have also provided valuable insights into the role of hydrogen (H) insertion in enhancing Mg intercalation within the V_2O_5 structure (Ni et al., 2019). By reducing the ion diffusion barriers, H insertion contributes to faster and more efficient Mg-ion transport within the cathode material, thus addressing one of the major challenges associated with the sluggish diffusion kinetics of magnesium ions. The benefits of incorporating water additives become apparent in the long-term cycling performance of the V_2O_5 cathode. The presence of the synthesized $H_xV_2O_5$ material is depicted in Figure 1.7(a), where X-ray diffraction (XRD) patterns and structural modeling are showcased in Figure 1.7(b). Remarkably, the synthesized $H_xV_2O_5$ exhibits exceptional capacity retention, retaining 91.3% of its initial capacity (425 $mAhg^{-1}$) even after an impressive 5,000 charge-discharge cycles, as depicted in Figure 1.7(c), and (d). Computational analysis further supports these findings, suggesting a reduced energy barrier for metal-ion migration attributable to the influence of proton insertion as shown in Figure 1.7(e) (Cao et al., 2022).

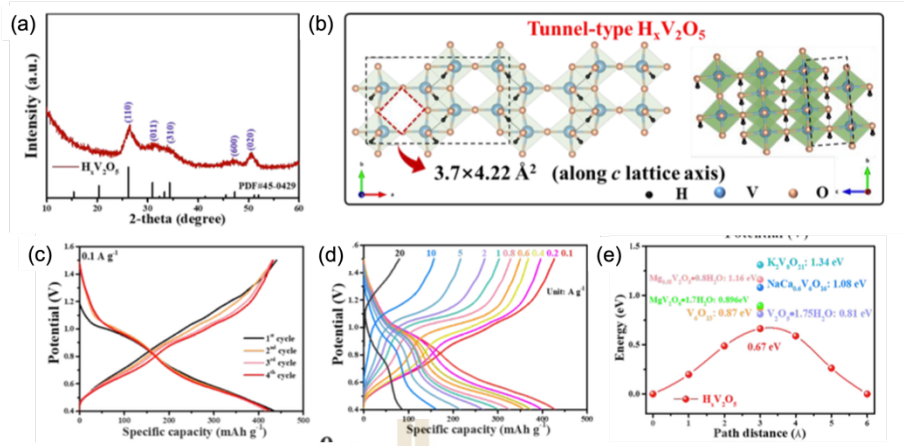

Figure 1.7 (a) X-ray diffraction pattern of $H_xV_2O_5$. (b) Structure of $H_xV_2O_5$. (c) Galvanostatic charge-discharge (GCD) curves of $H_xV_2O_5$ at 0.1 Ag^{-1}. (d) GCD curves of $H_xV_2O_5$ at different current densities. (e) Energy barrier for Zn^{2+} diffusion in $H_xV_2O_5$. (Cao et al., 2022).

In conclusion, the addition of aqueous electrolytes and the role of water additives have been instrumental in enhancing the electrochemical properties of V_2O_5 cathodes in metal-ion batteries, particularly for Mg-ion batteries. Water additives contribute to structural stabilization, facilitate the formation of $H_xV_2O_5$, and improve the capacity retention of the cathode during prolonged cycling. The dissociation of water at the electrode/electrolyte interface plays a crucial role in providing H^+ ions and electrons that protonate lattice oxygen, leading to improved cathode performance. Further advancements in this area hold significant promise for the continued development and optimization of efficient and high-performance Mg-ion battery technologies.

1.4 Research objectives

In light of the existing experimental and computational studies, the impact of H insertion on the structural stability of the V_2O_5 cathode remains unexplored. Therefore, the main objective of this research is to employ first-principles tools to conduct a systematic investigation into the role of H insertion and its influence on the enhanced electrochemical properties of the V_2O_5 cathode. Specifically, we will analyze its effect on the electronic structures and the overall electronic conductivity of the

material. By conducting calculations of Mg diffusion barriers, considering both ion and polaron transport, our research aims to propose how H insertion can lead to improvements in Mg-ion diffusion kinetics. Furthermore, through structural analysis, we will explore how H insertion can prevent the formation of irreversible phases of V_2O_5 structure, which is critical for maintaining the stability and performance of the cathode. The insights gained from this research will contribute to the development of strategies to enhance the overall performance of Mg-ion batteries. By understanding the underlying mechanisms and interactions involved in H insertion, this knowledge can help design and improve V_2O_5 cathodes, which in turn can help make better Mg-ion batteries.

1.5 Scope and limitations

The computational in this thesis employs the spin-polarized Density Functional Theory (DFT) method with the plane-wave technique as implemented in the Vienna ab initio Simulation Package (VASP 5) (Kresse et al., 1993). The electron-ion interaction is treated using the frozen-core projector-augmented wave (PAW) approach (Amadon et al., 2008). For the exchange-correlation functional, the Perdew-Burke-Ernzerhof (PBE) generalized gradient approximation is chosen. While DFT calculations yield accurate results for total energy and mechanical properties, it is essential to acknowledge that electronic properties, especially the band gap, might be underestimated compared to experimental reports due to the intrinsic self-interaction error in the PBE approximation. Nonetheless, electronic density of state (DOS) and band structure calculations still provide valuable insights into the electronic features of electron states and other essential characteristics. It is crucial to recognize that DOS-related electronic structures might not directly correspond to macroscopic conductivity. To analyze charge distribution on atoms and the amount of charge transfer, we employed the Bader charge calculation method, considering the Bader volume of an atom to estimate the zero flux regions and determine the net charge on particles. However, it should be noted that the assigned charge may not be represented by an integer number, necessitating careful consideration when interpreting the results. Specifically, we employed the Nudged Elastic Band (NEB) approach (Henkelman et al., 2000) for

the migration path of Mg-ion and H-ion. By combining these computational techniques, we can study the properties and behavior of the material. This helps us understand the electronic structure and how charges are spread out in the system. This method helps us get to know the material better, and it's important for making energy storage materials better in the future.

1.6 References

Abu-Khader, M. M. (2009). Recent advances in nuclear power: A review. *Progress in Nuclear Energy, 51*(2), 225-235.

Alva, G., Lin, Y., and Fang, G. (2018). An overview of thermal energy storage systems. *Energy, 144*, 341-378.

Amadon, B., Lechermann, F., Georges, A., Jollet, F., Wehling, T. O., and Lichtenstein, A. I. (2008). Plane-wave based electronic structure calculations for correlated materials using dynamical mean-field theory and projected local orbitals. *Physical Review B, 77*(20).

Andrews, J. L., Mukherjee, A., Yoo, H. D., Parija, A., Marley, P. M., Fakra, S., Prendergast, D., Cabana, J., Klie, R. F., and Banerjee, S. (2018). Reversible Mg-Ion Insertion in a Metastable One-Dimensional Polymorph of V_2O_5. *Chem, 4*(3), 564-585.

Bae, J., Park, H., Guo, X., Zhang, X., Warner, J. H., and Yu, G. (2021). High-performance magnesium metal batteries via switching the passivation film into a solid electrolyte interphase. *Energy & Environmental Science, 14*(8), 4391-4399.

Cao, J., Zhang, D., Yue, Y., Pakornchote, T., Bovornratanaraks, T., Zhang, X., Zeng, Z., Qin, J., and Huang, Y. (2022). Boosting Zn^{2+} Diffusion via Tunnel-Type Hydrogen Vanadium Bronze for High-Performance Zinc Ion Batteries. *ACS Appl Mater Interfaces, 14*(6), 7909-7916.

Davidson, R., Verma, A., Santos, D., Hao, F., Fincher, C., Xiang, S., Van Buskirk, J., Xie, K., Pharr, M., Mukherjee, P. P., and Banerjee, S. (2018). Formation of Magnesium Dendrites during Electrodeposition. *ACS Energy Letters, 4*(2), 375-376.

Drosos, C., Jia, C., Mathew, S., Palgrave, R. G., Moss, B., Kafizas, A., and Vernardou, D. (2018). Aerosol-assisted chemical vapor deposition of V_2O_5 cathodes with high

rate capabilities for magnesium-ion batteries. *Journal of Power Sources, 384*, 355-359.

Goodenough, J. B. (2012). Rechargeable batteries: challenges old and new. *Journal of Solid State Electrochemistry, 16*(6), 2019-2029.

Goodenough, J. B., and Park, K. S. (2013). The Li-ion rechargeable battery: a perspective. *Journal of the American Chemical Society, 135*(4), 1167-1176.

Gurney, K. R., Mendoza, D. L., Zhou, Y., Fischer, M. L., Miller, C. C., Geethakumar, S., and de la Rue du Can, S. (2009). High Resolution Fossil Fuel Combustion CO_2 Emission Fluxes for the United States. *Environmental Science & Technology, 43*(14), 5535-5541.

Henkelman, G., Uberuaga, B. P., and Jónsson, H. (2000). A climbing image nudged elastic band method for finding saddle points and minimum energy paths. *The Journal of Chemical Physics, 113*(22), 9901-9904.

Huie, M. M., Bock, D. C., Takeuchi, E. S., Marschilok, A. C., and Takeuchi, K. J. (2015). Cathode materials for magnesium and magnesium-ion based batteries. *Coordination Chemistry Reviews, 287*, 15-27.

Jiang, J., Li, H., Huang, J., Li, K., Zeng, J., Yang, Y., Li, J., Wang, Y., Wang, J., and Zhao, J. (2017). Investigation of the Reversible Intercalation/Deintercalation of Al into the Novel Li_3VO_4@C Microsphere Composite Cathode Material for Aluminum-Ion Batteries. *ACS Applied Materials & Interfaces, 9*(34), 28486-28494.

Johnson, I. D., Stapleton, N., Nolis, G., Bauer, D., Parajuli, P., Yoo, H. D., Yin, L., Ingram, B. J., Klie, R. F., Lapidus, S., Darr, J. A., and Cabana, J. (2021). Control of crystal size tailors the electrochemical performance of alpha-V_2O_5 as a Mg^{2+} intercalation host. *Nanoscale, 13*(22), 10081-10091.

Joselin Herbert, G. M., Iniyan, S., Sreevalsan, E., and Rajapandian, S. (2007). A review of wind energy technologies. *Renewable and Sustainable Energy Reviews, 11*(6), 1117-1145.

Kannan, N., and Vakeesan, D. (2016). Solar energy for future world: - A review. *Renewable and Sustainable Energy Reviews, 62*, 1092-1105.

Karapidakis, E., and Vernardou, D. (2021). Progress on V_2O_5 Cathodes for Multivalent Aqueous Batteries. *Materials (Basel), 14*(9).

Kim, S., Shan, X., Abeykoon, M., Kwon, G., Olds, D., and Teng, X. (2021). High-Capacity Aqueous Storage in Vanadate Cathodes Promoted by the Zn-Ion and Proton Intercalation and Conversion-Intercalation of Vanadyl Ions. *ACS Appl Mater Interfaces, 13*(22), 25993-26000.

Kresse, G., and Hafner, J. (1993). Ab initio molecular dynamics for liquid metals. *Phys Rev B Condens Matter, 47*(1), 558-561.

Liang, S., Qin, M., Tang, Y., Zhang, Q., Li, X., Tan, X., and Pan, A. (2014). Facile synthesis of nanosheet-structured V_2O_5 with enhanced electrochemical performance for high energy lithium-ion batteries. *Metals and Materials International, 20*(5), 983-988.

Liang, Y., Jing, Y., Gheytani, S., Lee, K. Y., Liu, P., Facchetti, A., and Yao, Y. (2017). Universal quinone electrodes for long cycle life aqueous rechargeable batteries. *Nat Mater, 16*(8), 841-848.

Liu, J., Xia, H., Xue, D., and Lu, L. (2009). Double-Shelled Nanocapsules of V_2O_5-Based Composites as High-Performance Anode and Cathode Materials for Li Ion Batteries. *Journal of the American Chemical Society, 131*(34), 12086-12087.

Liu, X., Euchner, H., Zarrabeitia, M., Gao, X., Elia, G. A., Groß, A., and Passerini, S. (2020). Operando pH Measurements Decipher H^+/Zn^{2+} Intercalation Chemistry in High-Performance Aqueous Zn/δ-V_2O_5 Batteries. *ACS Energy Letters, 5*(9), 2979-2986.

Lund, H., and Salgi, G. (2009). The role of compressed air energy storage (CAES) in future sustainable energy systems. *Energy Conversion and Management, 50*(5), 1172-1179.

Massé, R. C., Uchaker, E., and Cao, G. (2015). Beyond Li-ion: electrode materials for sodium- and magnesium-ion batteries. *Science China Materials, 58*(9), 715-766.

Murata, Y., Takada, S., Obata, T., Tojo, T., Inada, R., and Sakurai, Y. (2019). Effect of water in electrolyte on the Ca^{2+} insertion/extraction properties of V_2O_5. *Electrochimica Acta, 294*, 210-216.

Ngamwongwan, L., Fongkaew, I., Jungthawan, S., Hirunsit, P., Limpijumnong, S., and Suthirakun, S. (2021). Electronic and thermodynamic properties of native point defects in V_2O_5: a first-principles study. *Physical Chemistry Chemical Physics, 23*(19), 11374-11387.

มหาวิทยาลัยเทคโนโลยีสุรนารี

Ni, D., Shi, J., Xiong, W., Zhong, S., Xu, B., and Ouyang, C. (2019). The effect of protons on the Mg^{2+} migration in an alpha-V_2O_5 cathode for magnesium batteries: a first-principles investigation. *Physical Chemistry Chemical Physics, 21*(14), 7406-7411.

Nørskov, J. K., Rossmeisl, J., Logadottir, A., Lindqvist, L., Kitchin, J. R., Bligaard, T., and Jonsson, H. (2004). Origin of the overpotential for oxygen reduction at a fuel-cell cathode. *The Journal of Physical Chemistry B, 108*(46), 17886-17892.

Park, M. J., Yaghoobnejad Asl, H., and Manthiram, A. (2020). Multivalent-Ion versus Proton Insertion into Battery Electrodes. *ACS Energy Letters, 5*(7), 2367-2375.

Pavčnik, T., Bitenc, J., Pirnat, K., and Dominko, R. (2021). Electrochemical Performance of Mg Metal‐Quinone Battery in Chloride‐Free Electrolyte. *Batteries & Supercaps, 4*(5), 815-822.

Rashad, M., Asif, M., Ahmed, I., He, Z., Yin, L., Wei, Z. X., and Wang, Y. (2020). Quest for carbon and vanadium oxide based rechargeable magnesium-ion batteries. *Journal of Magnesium and Alloys, 8*(2), 364-373.

Rocquefelte, X., Boucher, F., Gressier, P., and Ouvrard, G. (2003). First-Principle Study of the Intercalation Process in the $Li_xV_2O_5$ System. *Chemistry of Materials, 15*(9), 1812-1819.

Roginskii, E. M., Smirnov, M. B., Smirnov, K. S., Baddour-Hadjean, R., Pereira-Ramos, J.-P., Smirnov, A. N., and Davydov, V. Y. (2021). A Computational and Spectroscopic Study of the Electronic Structure of V2O5-Based Cathode Materials. *The Journal of Physical Chemistry C, 125*(10), 5848-5858.

Sa, N., Wang, H., Proffit, D. L., Lipson, A. L., Key, B., Liu, M., Feng, Z., Fister, T. T., Ren, Y., Sun, C.-J., Vaughey, J. T., Fenter, P. A., Persson, K. A., and Burrell, A. K. (2016). Is alpha-V_2O_5 a cathode material for Mg insertion batteries? *Journal of Power Sources, 323*, 44-50.

Shah, R., Mittal, V., Matsil, E., and Rosenkranz, A. (2021). Magnesium-ion batteries for electric vehicles: Current trends and future perspectives. *Advances in Mechanical Engineering, 13*(3).

Shen, M., Huang, W., Chen, M., Song, B., Zeng, G., and Zhang, Y. (2020). (Micro)plastic crisis: Un-ignorable contribution to global greenhouse gas emissions and climate change. *Journal of Cleaner Production, 254*, 120138.

Sims, G. P. (1991). Hydroelectric energy. *Energy Policy, 19*(8), 776-786.

Tian, H., Gao, T., Li, X., Wang, X., Luo, C., Fan, X., Yang, C., Suo, L., Ma, Z., Han, W., and Wang, C. (2017). High power rechargeable magnesium/iodine battery chemistry. *Nat Commun, 8*, 14083.

Umeshbabu, E., and Ranga Rao, G. (2016). A Vanadium(V) Oxide Nanorod Promoted Platinum/Reduced Graphene Oxide Electrocatalyst for Alcohol Oxidation under Acidic Conditions. *Chemphyschem, 17*(21), 3524-3534.

Wang, F., Fan, X., Gao, T., Sun, W., Ma, Z., Yang, C., Han, F., Xu, K., and Wang, C. (2017). High-Voltage Aqueous Magnesium Ion Batteries. *ACS Cent Sci, 3*(10), 1121-1128.

Wu, X., and Ji, X. (2019). Aqueous batteries get energetic. *Nat Chem, 11*(8), 680-681.

Xu, Y., Deng, X., Li, Q., Zhang, G., Xiong, F., Tan, S., Wei, Q., Lu, J., Li, J., An, Q., and Mai, L. (2019). Vanadium Oxide Pillared by Interlayer Mg^{2+} Ions and Water as Ultralong-Life Cathodes for Magnesium-Ion Batteries. *Chem, 5*(5), 1194-1209.

You, C., Wu, X., Yuan, X., Chen, Y., Liu, L., Zhu, Y., Fu, L., Wu, Y., Guo, Y.-G., and van Ree, T. (2020). Advances in rechargeable Mg batteries. *Journal of Materials Chemistry A, 8*(48), 25601-25625.

Zhang, X., Wang, J. G., Liu, H., Liu, H., and Wei, B. (2017). Facile Synthesis of V_2O_5 Hollow Spheres as Advanced Cathodes for High-Performance Lithium-Ion Batteries. *Materials (Basel), 10*(1).

Zhao, Q., Liu, L., Yin, J., Zheng, J., Zhang, D., Chen, J., and Archer, L. A. (2020). Proton Intercalation/De-Intercalation Dynamics in Vanadium Oxides for Aqueous Aluminum Electrochemical Cells. *Angew Chem Int Ed Engl, 59*(8), 3048-3052.

Zhao, X., Zhang, X., Wu, D., Zhang, H., Ding, F., and Zhou, Z. (2016). Ab initio investigations on bulk and monolayer V_2O_5 as cathode materials for Li-, Na-, K- and Mg-ion batteries. *Journal of Materials Chemistry A, 4*(42), 16606-16611.

Zhao, Y., Zhang, X., Xiao, J., Fan, H., Zhang, J., Liu, H., Liu, Y., Yuan, H., Fan, S., and Zhang, Y. (2022). Effect of Mg Cation Diffusion Coefficient on Mg Dendrite Formation. *ACS Appl Mater Interfaces, 14*(5), 6499-6506.

มหาวิทยาลัยเทคโนโลยีสุรนารี

Zhou, B., Shi, H., Cao, R., Zhang, X., and Jiang, Z. (2014). Theoretical study on the initial stage of a magnesium battery based on a V_2O_5 cathode. *Phys Chem Chem Phys, 16*(34), 18578-18585.

Zhou, L., Liu, L., Hao, Z., Yan, Z., Yu, X.-F., Chu, P. K., Zhang, K., and Chen, J. (2021). Opportunities and challenges for aqueous metal-proton batteries. *Matter, 4*(4), 1252-1273.

มหาวิทยาลัยเทคโนโลยีสุรนารี

CHAPTER II
CALCULATION DETAILS

In this chapter, we exploded the theoretical and computational methods used in our study. To begin, we introduced the basics of computational quantum materials, focusing on the Schrödinger equation for systems with many particles (section 2.1). To find approximate solutions to the Schrödinger equation, the variational principle was described in section 2.2. Subsequently, we explored the historical development of computational quantum materials science (covered in sections 2.3 and 2.4). Following that, we explained the key concepts of density functional theory (section 2.5). Moving forward, we detailed the methodology employed for achieving structural optimization, crucial for identifying stable structures (section 2.6). We then delved into the techniques used to rectify errors arising from density functional theory calculations (discussed in sections 2.7 and 2.8). An overview of the climbing image-nudged elastic band (CI-NEB) method used for kinetic investigations is provided in section 2.9. Expanding on the dynamic aspects, we introduced the ab-initio molecular dynamics (AIMD) simulation technique (section 2.10). To understand the battery's character, the open circuit voltage profile was explained (section 2.11). Finally, we concluded this chapter with a summary of the calculation details employed in this work. These methodologies are implemented using the Vienna Ab initio Simulation Package (VASP), and this summary is presented in section 2.12.

2.1 Schrödinger equation for many particles

At the heart of understanding the quantum behavior of systems with multiple particles lies the Schrödinger equation. This fundamental equation, first formulated by Erwin Schrödinger in the 1920s, provides a mathematical framework for describing the wavefunctions of complex systems as described by

$$\hat{H}\Psi(\vec{R_i}, \vec{r_j}) = E\Psi(\vec{R_i}, \vec{r_j}) \tag{2.1}$$

The equation (2.1) represents an eigen equation, where $\hat{H}$ is the Hamiltonian operator that describes the kinetic and potential energy operators of a quantum system. The Ψ is the wave function, and it is a functional dependent on the coordinates of the nucleus index i ($\vec{R_i}$) and the electron index j ($\vec{r_j}$). The E denotes the eigenvalue, representing the energy of the system. The Hamiltonian operator consists of the kinetic energy operators of nucleus (T_N) and electron (T_e) and potential energy operators of nucleus-nucleus interaction (V_{NN}), nucleus-electron interaction (V_{Ne}) and electron-electron interaction (V_{ee}). Therefore, the Hamiltonian operator can be written as

$$\begin{aligned}\hat{H} &= T_N + T_e + V_{NN} + V_{Ne} + V_{ee} \\ &= -\sum_{i=1}^{N} \frac{\hbar^2}{2M_i}\nabla_{R_i}^2 - \sum_{j=1}^{n} \frac{\hbar^2}{2m_j}\nabla_{r_j}^2 + \frac{1}{2}\sum_{i=1}^{N}\sum_{i'=1}^{N} \frac{1}{4\pi\epsilon_0}\frac{Z_i Z_{i'} e^2}{|R_i - R_{i'}|} \\ &\quad - \sum_{i=1}^{N}\sum_{j=1}^{n} \frac{1}{4\pi\epsilon_0}\frac{Z_i e^2}{|R_i - r_j|} + \frac{1}{2}\sum_{j=1}^{n}\sum_{j'=1}^{n} \frac{1}{4\pi\epsilon_0}\frac{e^2}{|r_j - r_{j'}|}\end{aligned} \tag{2.2}$$

According to the Born-Oppenheimer approximation (Born et al., 1927), The assumption of motion of atomic nuclei and the motion of electrons in a molecule occur on vastly different time scales. In other words, it treats the electronic and nuclear motions as if they are decoupled or independent of each other. By treating the electronic and nuclear motions separately, and position of the nuclear is fixed. So, we can focus on solving the electronic Schrödinger equation for a fixed set of nuclear coordinates. Therefore, the most calculation cost is the Schrödinger equation for electrons using equation (2.1) as expanded following

$$\begin{pmatrix} -\sum_{j=1}^{n} \frac{\hbar^2}{2m_j}\nabla_{r_j}^2 & -\sum_{i=1}^{N}\sum_{j=1}^{n} \frac{1}{4\pi\epsilon_0}\frac{Z_i e^2}{|R_i - r_j|} \\ & +\frac{1}{2}\sum_{j=1}^{n}\sum_{j'=1}^{n} \frac{1}{4\pi\epsilon_0}\frac{e^2}{|r_j - r_{j'}|} \end{pmatrix} \Psi(\vec{r_j}) = E\Psi(\vec{r_j}) \tag{2.3}$$

This assumption allows us to determine the electronic energy levels and electronic wave functions of the molecule. Once the electronic structure is known, it

becomes possible to calculate various molecular properties, such as bond lengths, bond angles, vibrational frequencies, and more.

2.2 Variational principle

The variational principle is a concept used to find approximate solutions to the Schrödinger equation. The energy from solving the Schrödinger equation using any normalized wave function is always greater than or equal to ground state energy. The mathematical expression is as follows

$$\epsilon_0 \leq E = \langle \psi | \hat{H} | \psi \rangle \tag{2.4}$$

Where ϵ_0 is the ground state energy, E is the expectation value of the Hamiltonian operator of the system and ψ is the total wave function (eigenvector). The total wave function is a linear combination of the basis wave function as follow.

$$\psi = \sum_n c_n \phi_n \tag{2.5}$$

The expectation value can be solved using the equation as follow

$$E = \frac{\int dr^3 (\sum_n c_n^* \phi_n^*) \hat{H} (\sum_n c_m \phi_m)}{\int dr^3 (\sum_n c_n^* \phi_n^*)(\sum_n c_m \phi_m)} \tag{2.6}$$

According to equation (2.6), the expectation value is function of set of probability amplitude. Using the variational principle, we have to find the minimum expectation value as a function of probability amplitude (c_l) following.

$$\frac{\partial}{\partial c_l} E = \frac{\partial}{\partial c_l} \frac{\int dr^3 (\sum_n c_n^* \phi_n^*) \hat{H} (\sum_n c_m \phi_m)}{\int dr^3 (\sum_n c_n^* \phi_n^*)(\sum_n c_m \phi_m)} \tag{2.7}$$

Solving the equation (2.7), we can determine the secular equation as follow

$$\hat{h}\vec{c} = E\hat{S}\vec{c} \tag{2.8}$$

Where $\vec{c}$ is the probability amplitude vector of basis wave function. The $\hat{h}$ and $\hat{S}$ are the core Hamiltonian and the overlap matric, respectively, the matric element in core Hamiltonian and the overlap matric as determined by

$$[\hat{h}] = h_{nm} = c_n^* c_m \int dr^3 \phi_n^* \hat{H} \phi_m \tag{2.9}$$

$$[\hat{S}] = S_{nm} = c_n^* c_m \int dr^3 \phi_n^* \phi_m \tag{2.10}$$

2.3 Hartree approximation

The Hartree approximation (Hartree, 1928), also referred to as the Hartree method, stands as a simplified quantum mechanical technique employed to elucidate the electronic structure of multi-electron systems, such as atoms and molecules. Devised by Douglas Hartree during the 1920s,

It is imperative to emphasize that the Hartree approximation represents a rudimentary model, falling short of a comprehensive depiction of the intricate electron-electron correlations inherent in actual systems.

Within the Hartree approximation, electrons are considered to move independently of one another within the mean electrostatic field established by the other electrons and the nucleus. Consequently, electron-electron interactions are approximated as an average or mean-field influence, omitting the complete quantum mechanical interplay among electrons. The Hartree method relies on employing a distinct single-electron wave function, known as an orbital, for each electron. These orbitals are used to depict the motion of individual electrons within the system, as explained below:

$$\Psi(\vec{r}_1, \vec{r}_2, \ldots, \vec{r}_n) = \psi_1(\vec{r}_1)\psi_2(\vec{r}_2)\cdots\psi_n(\vec{r}_n) \tag{2.11}$$

where Ψ is the total wave function of the N-electron system and ψ_i is the one-electron wave function for the i^{th} electron, which depends only on the coordinates of that electron.

It is essential to highlight that the Hartree approximation treats electrons as distinguishable entities and does not consider the anti-symmetry requirement imposed by the Pauli exclusion principle on the electron wave function. Consequently, it falls short of providing a comprehensive account of the intricate quantum mechanical behavior of electrons in systems characterized by significant electron-electron correlations.

2.4 Hartree-Fock approximation

The Hartree-Fock (HF) approximation (Fock, 1930; Hartree, 1928) represents a sophisticated quantum chemistry method employed to elucidate the electronic structure of atoms and molecules. It stands as a substantial improvement over the basic Hartree method, as it takes into consideration the effects of electron-electron correlations to a certain degree. The primary objective of the Hartree-Fock method revolves around identifying the optimal set of single-electron wave functions, often referred to as orbitals, that minimizes the total electronic energy of a system while adhering to the essential Pauli exclusion principle.

Within the framework of the Hartree-Fock method, the electronic wave function for a multi-electron system is approximated as a Slater determinant (Slater, 1930), also known as an anti-symmetrized product, of one-electron wave functions. This representation ensures the required anti-symmetry of the electron wave function, a fundamental mandate imposed by the Pauli exclusion principle. The specific mathematical expression for this Slater determinant can be denoted as equation (2.12).

$$\Psi^{HF} = \frac{1}{\sqrt{N!}} \begin{vmatrix} \psi_1(\vec{r}_1) & \psi_1(\vec{r}_2) & \cdots & \psi_1(\vec{r}_n) \\ \psi_2(\vec{r}_1) & \psi_2(\vec{r}_2) & \cdots & \psi_2(\vec{r}_n) \\ \vdots & \vdots & \ddots & \vdots \\ \psi_n(\vec{r}_1) & \psi_n(\vec{r}_2) & \cdots & \psi_n(\vec{r}_n) \end{vmatrix} \tag{2.12}$$

where Ψ^{HF} is the Slater determinant representing the quantum state of the N electrons and $\psi_i(\vec{r}_j)$ is the one-electron wave function (spatial orbital) for electron index j in spatial orbital index i

According to the HF approximation, the exchange energy term arises due to the enforced anti-symmetry of the electron wave function. Consequently, when examining systems with multiple particles using the HF approximation, it can be concluded that the total energy comprises the kinetic energy of electrons, the potential energy of electron-nuclei interactions, the potential energy of electron-electron interactions, and the exchange energy stemming from the HF approximation.

2.5 Density functional theory

The density functional theory (DFT) scheme is based on the concept of considering the total electron density, denoted as equation (2.13), rather than focusing on individual particles within the system. This approach leads to a more simplified approximation of the Schrödinger equation when compared to the Hartree-Fock approximation. The electron density can be expressed in terms of the wavefunction, representing a fundamental connection between the DFT method and the quantum mechanical description of electronic systems.

$$\rho(\vec{r}) = \sum_i \Psi_i^*(\vec{r})\Psi_i(\vec{r}) = \sum_i |\Psi(\vec{r})|^2 \tag{2.13}$$

2.5.1 The Hohenberg-Kohn theorems

The Hohenberg-Kohn theorems (Hohenberg et al., 1964) are fundamental principles in the field of quantum mechanics and DFT. They provide a theoretical foundation for DFT, a widely used method for predicting the electronic structure and properties of many-electron systems, such as atoms, molecules, and solids. The theorems were developed by Pierre Hohenberg and Walter Kohn in the 1960s. There are two Hohenberg-Kohn theorems, often referred to as the first and second theorems.

1. First Hohenberg-Kohn Theorem:

The first theorem states that the external potential, $V(r)$, uniquely determines the ground-state electron density, $\rho(r)$, and vice versa. In other words, if you know

the external potential, you can determine the electron density, and if you know the electron density, you can determine the external potential. This theorem provides the foundation for the idea that the total energy of a quantum system can be expressed as a functional of the electron density, $E[\rho]$, and the external potential, $V(r)$. The goal of DFT is to find the electron density that minimizes the total energy, as this corresponds to the ground-state electron density and energy.

2. Second Hohenberg-Kohn Theorem:

The second theorem focuses on the uniqueness of the ground-state electron density and total energy. It states that there is a one-to-one correspondence between the ground-state electron density, $\rho_0(r)$, and the external potential, $V_0(r)$, that leads to the same minimum value of the ground-state energy, E_0 In other words, there is only one ground-state electron density and one corresponding external potential that minimize the total energy. Mathematically, the second theorem can be expressed as:

$$E[\rho_0(r)] = \frac{\partial E[\rho(r)]}{\partial \rho}|_{\rho=\rho_o(r)} = min_{\rho\to\rho_0} E[\rho(r)] \qquad (2.14)$$

These theorems provide a rigorous foundation for the development of density functional theory, which seeks to find the electron density that minimizes the total energy of a quantum system. While the theorems themselves do not provide an explicit method for finding the ground-state electron density, they are crucial in establishing the theoretical framework for DFT and ensuring its accuracy and reliability in predicting the properties of many-electron systems.

2.5.2 The Kohn-Sham equation

According to the second Hohenberg-Kohn theorem, knowledge of the total energy of a quantum system provides the necessary information to determine the conditions for achieving the minimum total energy. In the context of the Kohn-Sham equation, which is a key component of DFT, the kinetic energy of electrons in a many-particle system can be separated into two distinct terms: (1) the kinetic energy of non-interacting electrons and (2) the contribution arising from electron-electron correlations, often referred to as the correlation effect on kinetic energy. Consequently,

the expression for the kinetic energy of electrons in a many-particle system can be formulated as follows:

$$T[\rho(r)] = T_{non}[\rho(r)] + T_{cor}[\rho(r)] \tag{2.15}$$

If we consider a many-particle system composed of N nuclei and N_e electrons, the kinetic energy of non-interacting electrons can be described as equation (2.16). This term accounts for the kinetic energy of electrons as if they were moving independently, neglecting electron-electron interactions.

$$T_{non}[\rho(r)] = \sum_{i}^{N_e} \langle \psi_i(r) | \frac{-\nabla^2}{2} | \psi_i(r) \rangle \tag{2.16}$$

The potential energy terms corresponding to electron-electron interactions and electron-nucleus interactions can be expressed as equation (2.17) and (2.18), respectively. These terms encapsulate the electrostatic forces between electrons (V_{ee}) and between electrons and nuclei (V_{Ne}), respectively, and are pivotal in determining the overall energy of the quantum system.

$$V_{ee} = \langle \psi_e(r) | \frac{1}{2} \sum_{i}^{N_e} \sum_{j}^{N_e} \frac{1}{|r_i - r_j|} | \psi_e(r) \rangle = \frac{1}{2} \int \int \frac{\rho(r)\rho(r')}{|r - r'|} dr dr' \tag{2.17}$$

$$V_{Ne} = \langle \psi_e(r) | \sum_{i}^{N} \sum_{j}^{N_e} \frac{-Z_i}{|R_i - r_j|} | \psi_e(r) \rangle = -\sum_{i=1}^{N} \int \frac{Z_I \rho(r)}{|R_I - r|} dr \tag{2.18}$$

In accordance with the Hartree-Fock approximation, the exchange energy naturally emerges due to the enforced anti-symmetry of the electron wave functions. However, it's important to note that the total energy computed using the Hartree-Fock approximation does not encompass the correlation energy. To address this limitation, DFT consolidates both the exchange and correlation energy components into a single term known as the exchange-correlation energy, as depicted below

$$E_{xc}[\rho(r)] = E_x[\rho(r)] + E_c[\rho(r)] \tag{2.19}$$

Therefore, the total energy of many particles system depicted below

$$E[\rho(r)] = T_{non}[\rho(r)] + \frac{1}{2}\int\int \frac{\rho(r)\rho(r')}{|r-r'|}drdr' - \sum_{i=1}^{N}\frac{Z_i\rho(r)}{|R_i - r|}dr + E_{xc}[\rho(r)] \quad (2.20)$$

According to the second Hohenberg-Kohn theorem, the ground state energy of a quantum system can be calculated through the minimization of the total energy functional with respect to the electron density. The condition that yields the minimum total energy can be expressed as

$$\left[-\frac{\nabla_i^2}{2} + V_{eff}[\rho(r)]\right]\psi_i^{KS}(r) = E_i\psi_i^{KS}(r) \quad (2.21)$$

Effective potential can be expressed as

$$\begin{aligned} V_{eff}[\rho(r)] &= V_H[\rho(r)] + V_{ext}[\rho(r)] + Vxc[\rho(r)] \\ &= \frac{1}{2}\int \frac{\rho(r')}{|r-r'|}dr' - \sum_{i=1}^{N}\frac{Z_i}{|R_i - r|} + V_{xc}[\rho(r)] \end{aligned} \quad (2.22)$$

2.5.3 Exchange-correlation functional

In DFT calculations, the exchange-correlation functional is a crucial component of the DFT approximation. It is a mathematical expression that accounts for the exchange and correlation effects of the electrons in a many particles system. These effects arise due to the interactions between electrons, and accurately modeling them is essential for predicting the electronic structure and properties of materials.

In present day, the widely used exchange-correlation functional have two type (1) the local density approximation (LDA) and (2) the generalized gradient approximation.

1. The local density approximation (LDA)

The local density approximation using the assumption that electron have equally distribution as homogeneous electron gas. The exchange energy can be written by

$$E_x^{LDA}[\rho(r)] = -\frac{3}{4}\left(\frac{3}{\pi}\right)^{1/3}\rho(r)^{1/3} \tag{2.23}$$

Currently, the true form of the correlation functional in DFT remains unknown, and as such, practical implementations often involve approximations. One common approach is to fit the DFT correlation functional to data obtained from quantum Monte Carlo simulations (QMC) (Ceperley et al., 1980) to achieve better accuracy. A widely used correlation functional in this context is the Perdew-Zunger (PZ) correlation functional (J. P. Perdew et al., 1981), which is described as follows

$$E_c^{PZ} = \begin{cases} \gamma/(1+\beta_1\sqrt{r_s}+\beta_2 r_s); & r_s > 1 \\ Alnr_s + B + Cr_s lnr_s + Dr_s; & 0 \le r_s \le 1 \end{cases} \tag{2.24}$$

When $r_s = \left(\frac{3}{4\pi\rho(r)}\right)^{1/3}$ and the associated parameters in equation (2.24), it is common practice to represent these values in a tabular format, as shown in Table 2.1.

Table 2.1 Assorted constants for PZ correlation energy calculations.

γ	β_1	β_2	A	B	C	D
-0.1423	1.0529	0.3334	0.0311	-0.0480	0.0020	-0.0116

The LDA functional is not always suitable due to its limitations in accurately describing non-local exchange-correlation effects, dispersion interactions, strongly correlated systems, and electronic properties, making it less reliable compared to more advanced exchange-correlation functionals like GGAs and hybrid functionals.

2. The generalized gradient approximation (GGA)

The generalized gradient approximation (GGA) takes into account not only the electron density at a given point in space but also its gradient, providing a better description of electron-electron interactions and often leading to more accurate predictions of electronic and structural properties in a wide range of materials and systems. One of the widely used exchange-correlation functionals for density DFT calculations is the Perdew-Burke-Ernzerhof (PBE) exchange-correlation functional (John

P. Perdew et al., 1996), which can be described by the following mathematical expression as

$$E_x^{PBE}[\rho(r), \nabla\rho(r)] = -\frac{3}{4}\left(\frac{3}{\pi}\right)^{1/3} \rho(r)^{1/3} F(x) \tag{2.25}$$

when

$$F(x) = 1 + a - \frac{a}{1 + bx^2}$$

$$x = \frac{|\nabla\rho(r)|}{\rho(r)^{4/3}}$$

The PBE functional enhances the LDA-based foundation for correlation energy by incorporating the gradient term.

$$E_c^{PBE}[\rho(r), \nabla\rho(r)] = E_c^{LDA}[\rho(r)] + H[\rho(r), \nabla\rho(r)] \tag{2.26}$$

when

$$H[\rho(r), \nabla\rho(r)] = cln\left[1 + dt^2\left(\frac{1 + At^2}{1 + At^2 + A^2t^4}\right)\right]$$

$$A = d\left[exp\left(-\frac{E_c^{LDA}[\rho(r)]}{c} - 1\right)\right]^{-1}$$

$$t = \frac{|\nabla\rho(r)|}{2(3\pi^2)^{1/3}\rho(r)^{4/3}}$$

มหาวิทยาลัยเทคโนโลยีสุรนารี

2.5.4 Pseudopotentials

Pseudopotentials represent a valuable approach to streamline complex calculations in computational chemistry. They serve as substitutes for the genuine potential of atomic nuclei, offering an effective potential meticulously tailored to emulate the behavior of valence (outermost) electrons while simplifying or ignoring the behavior of tightly bound inner-core electrons. This strategic simplification substantially reduces the computational intricacies associated with electronic structure calculations, all while yielding precise results for numerous properties of interest.

As depicted in Figure 2.1, the convergence of the pseudo and exact potential occurs when the interparticle distance surpasses the specified cutoff radius, r_c, as does the convergence of the pseudo (ψ_{pseudo}) and exact (ψ) wavefunctions. Notably, the authentic wavefunction exhibits oscillations within the lower r_c region. This oscillatory behavior poses a challenge in solving the Schrödinger equation effectively, as achieving a smooth wavefunction in this region is demanding, as illustrated by the red solid line. Employing a smoother wavefunction serves to reduce computational expenses while preserving accuracy. Consequently, the prerequisites for the pseudo wavefunction and potential are as follows:

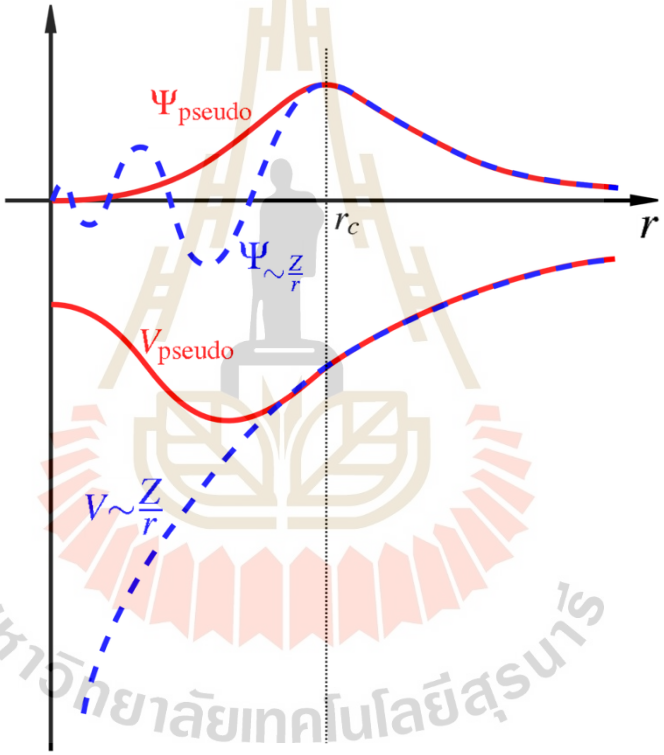

Figure 2.1 Contrast between wavefunctions in nuclear coulomb potential (blue) and pseudopotential (red).

1. At $r \geq r_c$, it is a requirement that the pseudo wavefunction aligns with the exact wavefunction, and the total energy of the pseudopotential matches that of the exact potential.

2. At $r = r_c$, it is imperative that the pseudo wavefunction and the exact wavefunction exhibit continuous properties, as articulated in the mathematical equation that follows

$$\left.\frac{1}{\psi_{pseudo}}\frac{d\psi_{pseudo}}{dr}\right|_{r=r_c} = \left.\frac{1}{\psi}\frac{d\psi}{dr}\right|_{r=r_c}$$
$$\left.\frac{dln\psi_{pseudo}}{dr}\right|_{r=r_c} = \left.\frac{dln\psi}{dr}\right|_{r=r_c} \quad (2.27)$$

3. The pseudo wavefunction is required to possess a total charge within a sphere of radius r_c that is equivalent to that of the exact wavefunction.

$$\int_0^{r_c} r^2|\psi_{pseudo}|^2 dr = \int_0^{r_c} r^2|\psi|^2 dr \quad (2.28)$$

4. The pseudopotential should exhibit transferability properties, meaning it can accurately describe both the isolated atom and its ions.

Within the realm of pseudopotentials, several distinct categories exist:

1. Norm-Conserving Pseudopotentials: This category of pseudopotentials is carefully crafted to maintain the norm, ensuring the conservation of the total number of electrons. Additionally, norm-conserving pseudopotentials offer accurate representations of valence electron wavefunctions.
2. Ultra-Soft Pseudopotentials: Specifically engineered for smoothness, ultra-soft pseudopotentials find extensive utility in plane-wave basis Density Functional Theory (DFT) calculations. Their smoothness facilitates efficient convergence and enhances the computational efficiency of simulations.
3. Projector-Augmented Wave (PAW) Pseudopotentials: PAW pseudopotentials (Amadon et al., 2008) stand out as highly precise and versatile tools in electronic structure calculations. Combining elements from both pseudopotentials and all-electron calculations, they enable a remarkably accurate representation of electron properties, allowing for in-depth investigations of various electronic phenomena.

2.5.5 Self-Consistent Field approach

In practical DFT calculations, the ground state energy can be determined through a self-consistent field calculation, as outlined in Figure 2.2.

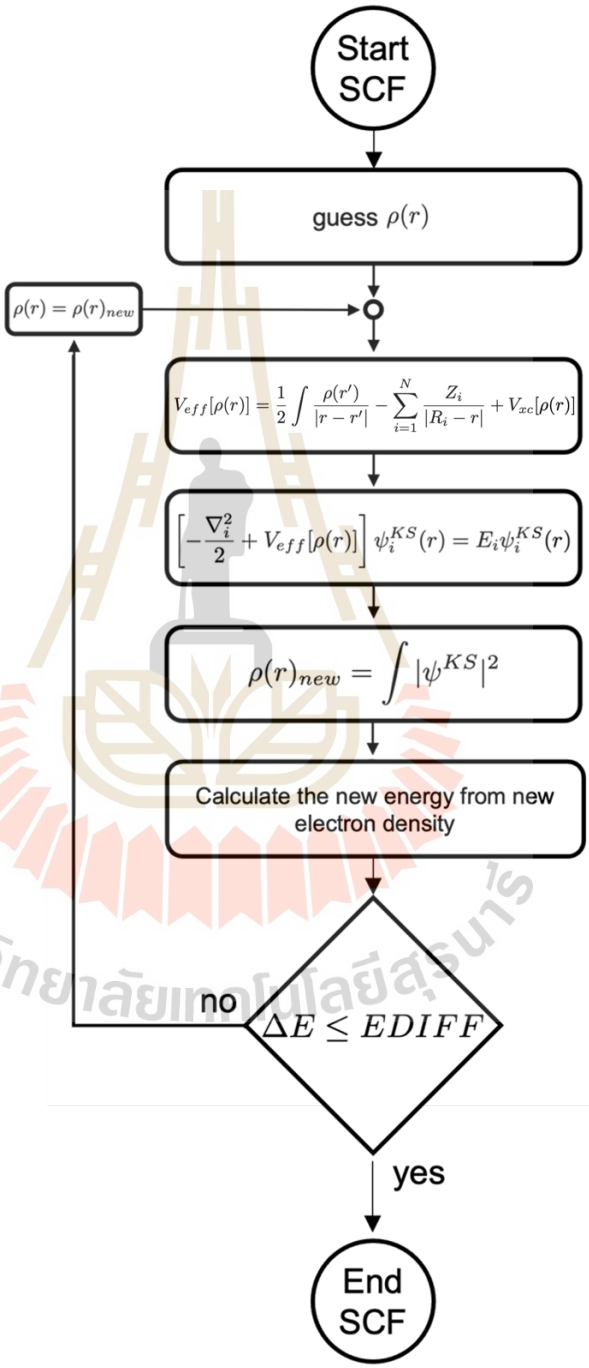

Figure 2.2 The schematic of self-consistency iteration for solving the Kohn-Sham equation and determining the calculated total energy and other properties.

This self-consistent field calculation involves the following steps:

1. Initial Electron Density Guess: Begin by making an initial guess for the electron density.
2. Effective Potential Calculation: Utilize the initial electron density to compute the effective potential.
3. Solving the Kohn-Sham Equation: Solve the Kohn-Sham equation to obtain the eigenvalues (total energy) and eigenvectors (wave functions).
4. New electron density calculation: Calculate a new electron density based on the obtained eigenvectors (wave functions).
5. New electronic energy calculation: Calculate a new energy using the Kohn-Sham Equation
6. Comparing energy
    a. If the difference of new and old electronic energy is lower than the energy criteria (EDIFF), terminate the calculation and use the resulting values.
    b. If the difference of new and old electronic energy is greater than the energy criteria (EDIFF), update the electron density with the new values and return to step 2 for further iterations. Repeat this process until convergence is achieved.

This iterative self-consistent field approach ensures that the electron density and effective potential converge to a consistent solution, ultimately yielding the ground state energy in DFT calculations. The energy criteria (EDIFF) used in this research is 10^{-6} eV.

2.6 Geometry optimization

Geometry optimization plays a pivotal role in DFT calculations, especially in the study of molecules and materials. This process involves seeking the most energetically favorable arrangement of atoms by minimizing the system's total energy while considering changes in atomic positions and, if applicable, unit cell dimensions.

Below is an overview of the geometry optimization process in DFT calculations (as you can see in Figure 2.3):

1. Initial Geometry: Provide the initial atomic coordinate.
2. Energy Calculation: Perform DFT calculation for energy of the system using the SCF calculation.
3. Forces and Gradients: Calculate the atomic force using the Hellmann-Feynman forces calculation.
4. Evaluate Convergence: Check all of atomic force.
    a. If atomic force is lower than the tolerance force, terminate the calculation and use the resulting values.
    b. If atomic force is greater than the tolerance force, atomic positions are adjusted based on the calculated forces and gradients. Optimization algorithms such as the conjugate gradient method (Dai et al., 2016) is employed for this purpose and return to SCF loop at step 2.

Geometry optimization is fundamental for accurate predictions of molecular and material properties, offering insights into atomic positions and total energy. These insights are essential for comprehending the behavior and stability of chemical systems.

มหาวิทยาลัยเทคโนโลยีสุรนารี

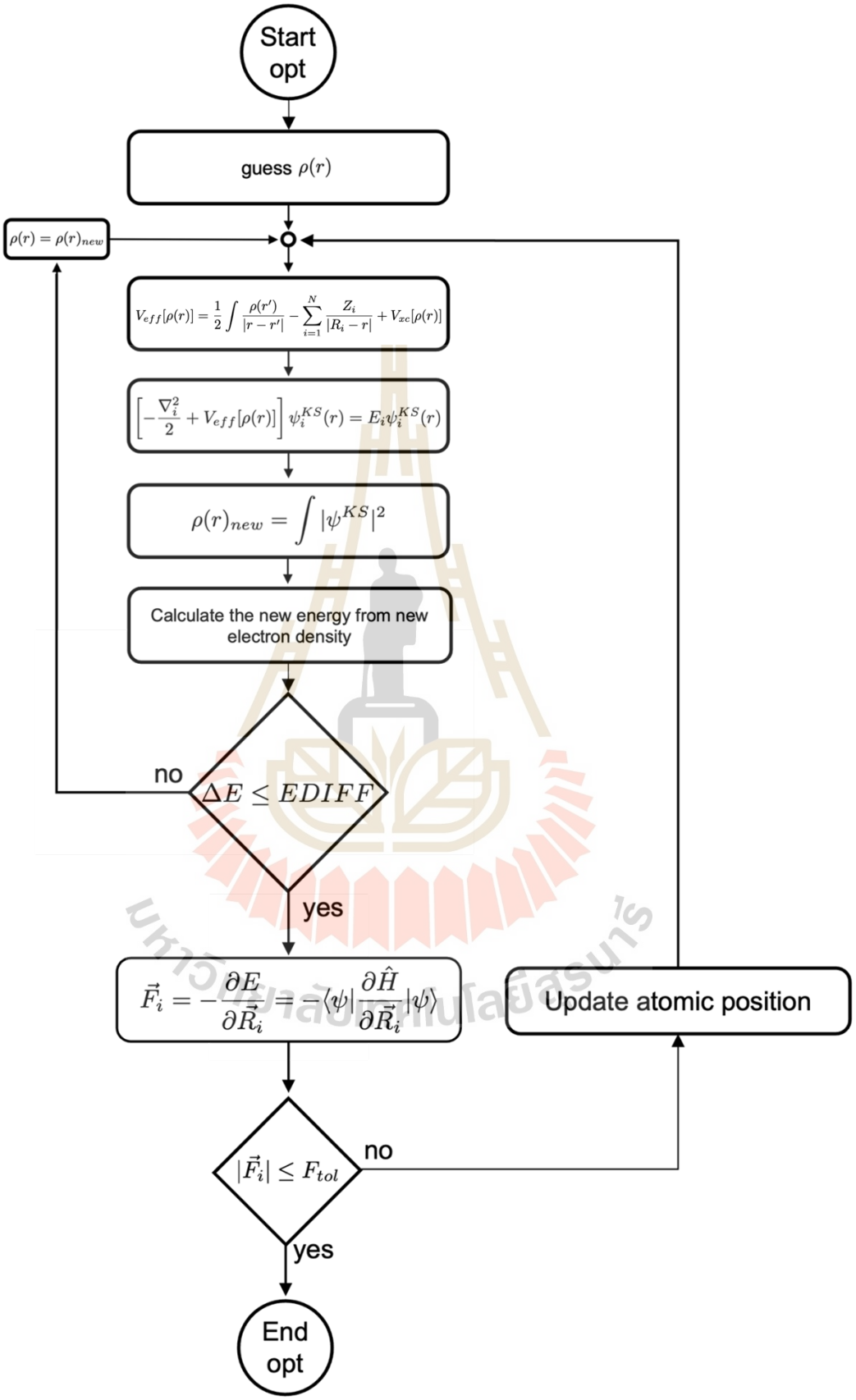

Figure 2.3 The schematic of optimization in DFT calculations.

2.7 DFT+U

DFT+U, short for Density Functional Theory + Hubbard U (Anisimov et al., 1991), is an extension of the conventional Density Functional Theory (DFT) method used in computational materials science and solid-state physics. DFT is a widely employed approach for calculating electronic properties and predicting the behavior of materials. However, it has limitations when it comes to accurately describing systems with localized electron interactions, such as transition metals and strongly correlated electron systems. The DFT calculates electronic properties by approximating the electron density of a system and minimizing the total energy. While it can provide reasonable results for many materials, it often struggles with accurately describing systems where electron-electron interactions are strongly localized and correlated. This is where DFT+U comes in.

The "+U" term represents an additional parameter introduced to account for the on-site Coulomb interactions (Hubbard U) between electrons on the same atomic orbital. In a transition metal oxide, for example, electrons in d orbitals can be strongly localized due to electron-electron repulsions. DFT+U introduces a correction to the energy functional to better capture these localized electron interactions. In essence, DFT+U aims to correct the electronic structure description provided by standard DFT, making it more suitable for systems with localized electron correlations. The Hubbard U term effectively adds a repulsive energy to the electrons occupying the same orbital, simulating the Coulomb repulsion between them. Mathematically, the DFT+U correction can be expressed as follows:

$$\frac{U-J}{2}\sum_{\sigma}\left[\sum_{j}\rho_{jj}^{\sigma}-\sum_{j,l}\rho_{jl}^{\sigma}\rho_{lj}^{\sigma}\right] \tag{2.29}$$

when U is the Hubbard U parameter, J is the Hund's exchange coupling parameter and ρ_{lj}^{σ} is the density matrix of d electrons.

It's important to note that DFT+U is not a universal solution and requires careful parameter tuning, specifically choosing appropriate values for the Hubbard U parameter for different elements and materials. The choice of U can have a significant impact on the results, so there's an element of empirical adjustment involved.

2.8 vdW correction

In DFT, one of the known limitations is its inability to accurately account for van der Waals (vdW) interactions. Van der Waals forces are weak, long-range interactions between molecules or atoms that arise due to fluctuations in electron density. Since standard DFT functionals, such as LDA and GGA, are designed to capture primarily local exchange and correlation effects, they often underestimate vdW interactions. To address this limitation, various vdW correction methods have been developed to incorporate vdW interactions into DFT calculations. One common approach is the use of the DFT-D3 method developed by Grimme (Grimme et al., 2010). The method employed in this study is optPBE-vdW (Optimized Perdew-Burke-Ernzerhof with van der Waals) (Klimes et al., 2010), which is a modification of DFT aimed at incorporating vdW interactions in a more systematic and accurate manner. Unlike the standard PBE functional, optPBE-vdW incorporates a correction term that addresses long-range vdW interactions, enhancing the applicability of DFT for investigating systems where vdW forces are of significant importance, such as molecular complexes, layered materials, and intermolecular interactions.

The optPBE-vdW correction introduces a pairwise vdW interaction term to the conventional PBE exchange-correlation functional, expressed as follows:

$$E_{disp}^{optPBE-vdW} = \sum_{AB} \frac{C_{6AB}}{R_{AB}^6} f_{damp}(R_{AB}) \tag{2.30}$$

when $E_{disp}^{optPBE-vdW}$ is the dispersion energy correction, $\sum_{AB}$ represents a sum over all atom pairs A and B in the system, C_{6AB} is the dispersion coefficient for the atom pair A and B, determined empirically based on the atom types involved, R_{AB} is the distance between the atom pair A and B and $f_{damp}(R_{AB})$ is a damping function that ensures the correction decreases smoothly at long distances to avoid unphysical divergences. The damping function is often modeled as:

$$f_{damp}(R_{AB}) = 1 - exp(-\alpha(R_{AB} - R_S)^2) \tag{2.31}$$

when α is a damping parameter controlling the rate of decay and R_S is a cutoff radius beyond which the correction becomes negligible.

The C_{6AB} coefficients for various atom pairs are typically obtained from empirical databases or parameterization. These coefficients represent the strength of dispersion interactions between different atom types.

2.9 Climbing image-nudged elastic band method

The climbing image-nudged elastic band (CI-NEB) (Henkelman et al., 2000) is a valuable technique in DFT calculations for identifying transition states and elucidating reaction pathways. It extends the Nudged Elastic Band (NEB) method by introducing a "climbing" image that automatically converges toward the transition state, improving accuracy in locating the highest energy points along a reaction coordinate. Key aspects and mathematical expressions of the CI-NEB method include:

1. Nudged Elastic Band (NEB)

NEB depicts the reaction pathway by employing a series of intermediate configurations (images) that link the initial and final states, each characterized by specific atomic coordinates. The elastic band, consisting of N+1 images, can be represented as [R_0, R_1, R_2, ..., R_N], where R_0 and R_N remain fixed. The overall force exerted on the atom at each image index i is the summation effect of the spring force in the local tangent direction and the true force perpendicular to the local tangent, denoted as:

$$\vec{F}_i^{NEB} = \vec{F}_i^{s||} - \nabla E(\vec{R}_i)^{\perp} \tag{2.32}$$

Where the true force is given by

$$\nabla E(\vec{R}_i)^{\perp} = \nabla E(\vec{R}_i) - \nabla E(\vec{R}_i) \cdot \hat{\tau}_i \tag{2.33}$$

Here, E is the energy of the system as function of all the atomic coordinates, and $\hat{\tau}_i$ is the normalized local tangent at image index i. The spring force is represented as

$$\vec{F}_i^{s||} = k(|\vec{R}_{i+1} - \vec{R}_i| - |\vec{R}_i - \vec{R}_{i-1}|)\hat{\tau}_i \tag{2.34}$$

where k is the spring constant. An optimization algorithm is used to move the images according to the NEB force in equation (2.32). The images converge on the minimum

energy pathway with the NEB force must lower than the force criteria. Note that, the force criteria for NEB calculation in this thesis is 0.05 eV/Å.

2. Climbing Image

The climbing image nudged elastic band method represents a minor adaptation of the NEB method. While preserving information about the shape of the minimum energy pathway, it ensures convergence to a saddle point. Following several iterations with the standard NEB, the image with the highest energy (i_{max}) is determined. The force acting on that image is not determined by equation (2.32) but rather by

$$\vec{F}_{i_{max}} = -\nabla E(\vec{R}_{i_{max}}) + 2\nabla E(\vec{R}_{i_{max}}) \cdot \hat{\tau}_{i_{max}} \tag{2.35}$$

The maximum energy image is not affected by the spring forces at all.

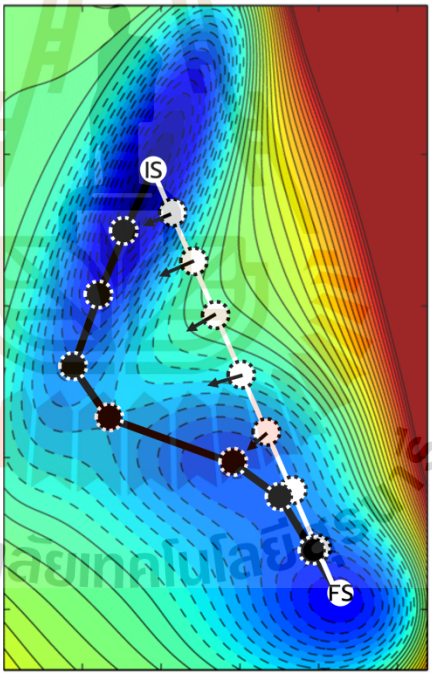

Figure 2.4 Schematic of the potential energy surface (PES) and NEB Calculation. White and black lines denote the initial guess and optimized reaction pathways.

In summary, the CI-NEB method combines NEB principles with the concept of a climbing image to efficiently pinpoint transition states and calculate energy barriers for chemical reactions. Widely used in computational chemistry, CI-NEB aids in studying

reaction mechanisms and understanding complex reaction pathways, ensuring accurate positioning of the transition state along the reaction coordinate.

2.10 Ab initio molecular dynamics

Ab initio molecular dynamics (AIMD) is a computational technique used in the field of quantum chemistry and materials science to simulate the motion of atoms and molecules over time. AIMD combines molecular dynamics (MD) with quantum mechanical calculations, typically using DFT or other ab initio methods, to accurately describe the electronic structure and interactions among particles.

In AIMD simulations, the positions and velocities of all atoms in a system are propagated through time using classical molecular dynamics equations, such as the Verlet algorithm (Verlet, 1967). However, instead of using classical force fields to calculate interatomic forces, AIMD employs quantum mechanical calculations to determine the forces acting on the atoms. The mathematical model of AIMD comprises several fundamental components:

1. Quantum mechanical calculations

AIMD incorporates quantum mechanical calculations, using DFT, at each time step. These calculations determine the forces acting on each atom based on the electronic structure.

$$\vec{F}_i = -\langle\psi|\frac{\partial\hat{H}}{\partial\vec{R}_i}|\psi\rangle \tag{2.36}$$

2. Newton's equations of motion

These classical equations describe the time-dependent evolution of atomic positions (r) and velocities (v).

$$m_i\frac{d^2\vec{r}_i}{dt^2} = \vec{F}_i \tag{2.37}$$

มหาวิทยาลัยเทคโนโลยีสุรนารี

3. Integration Scheme

Numerical integration methods, such as the Verlet algorithm, are employed to integrate the equations of motion. These methods update the positions and velocities of atoms at each time step.

$$\begin{aligned} \vec{a}_i(t+\Delta t) &= \frac{\vec{F}_i(t+\Delta t)}{m_i} \\ \vec{v}_i(t+\Delta t) &= \vec{v}_i(t) + \frac{1}{2}(\vec{a}_i(t) + \vec{a}_i(t+\Delta t)) \\ \vec{R}_i(t+\Delta t) &= \vec{R}_i(t) + \vec{v}_i(t)\Delta t + \frac{1}{2}\vec{a}_i(t)\Delta t^2 \end{aligned} \tag{2.38}$$

4. Boundary Conditions

AIMD simulations often employ periodic boundary conditions, replicating the simulation cell periodically in all directions to mimic an effectively infinite system. This ensures an accurate representation of interactions between atoms.

5. Temperature Control

AIMD simulations may incorporate thermostats to control the system's temperature, enabling simulations at a constant temperature, e.g., through the use of the Nose-Hoover thermostat (Hoover, 1985; Nosé, 1984).

6. Time Steps

The choice of the time step (Δt) for integration is crucial. It must strike a balance between accuracy and computational efficiency. It must be small enough to capture atomic motion accurately but not so small as to render the simulation computationally prohibitive.

The AIMD simulations are tools for investigating dynamic processes in chemistry and materials science, encompassing phenomena like chemical reactions, and vibrational dynamics. They offer insights into atomic and molecular behavior at the quantum mechanical level, playing a vital role in comprehending complex molecular and material dynamics.

2.11 Open circuit voltage calculation

The voltage of the battery, which can be measured using a voltmeter inserted between the anode and the cathode in an open circuit, can be determined by utilizing equation (2.39) (Van der Ven et al., 2020)

$$V = -\frac{\eta_{e^-}^{C} - \eta_{e^-}^{A}}{e} \tag{2.39}$$

In the provided equation, $\eta_{e^-}^{C}$ and $\eta_{e^-}^{A}$ represent the electrochemical potential of electrons on the cathode and anode, respectively, while e denotes the elementary charge of an electron (~ 1.602×10^{-19} C).

The electrochemical potentials provide a means of quantifying how the energy of cathode or anode materials changes when a charged species is introduced. These electrochemical potentials can be directly linked to the chemical potentials for neutral species. In the specific case of the neutral Mg chemical potential within the cathode or anode materials, it is defined as the change in energy that occurs upon the addition of neutral Mg atoms, and it is expressed by the equation:

$$\mu_{Mg}^{\alpha} = \frac{\partial E^{\alpha}}{\partial N_{Mg}^{\alpha}} = \frac{\partial E^{\alpha}}{\partial N_{Mg^{2+}}^{\alpha}} \frac{\partial N_{Mg^{2+}}^{\alpha}}{\partial N_{Mg}^{\alpha}} + \frac{\partial E^{\alpha}}{\partial N_{e^-}^{\alpha}} \frac{\partial N_{e^-}^{\alpha}}{\partial N_{Mg}^{\alpha}} = \eta_{Mg^{2+}}^{\alpha} + 2\eta_{e^-}^{\alpha} \tag{2.40}$$

In this equation, $\eta_{Mg^{2+}}^{\alpha}$ represents the electrochemical potential of Mg^{2+} ions in the cathode or anode material, and $\eta_{e^-}^{\alpha}$ denotes the electrochemical potential of electrons within the same material. This equation establishes a fundamental relationship between the electrochemical potentials and the chemical potential of neutral Mg species, shedding light on the intricate energy changes occurring during the electrochemical processes within the battery.

Utilizing equation (2.40), we can express equation (2.39) as:

$$V = -\frac{\frac{1}{2}\left(\mu_{Mg}^{C} - \eta_{Mg^{2+}}^{C}\right) - \frac{1}{2}\left(\mu_{Mg}^{A} - \eta_{Mg^{2+}}^{A}\right)}{e} \tag{2.41}$$

In an open-circuit and equilibrium state, it is crucial for the Mg^{2+} electrochemical potential to remain uniform throughout the entire battery, which implies $\eta^{C}_{Mg^{2+}} = \eta^{A}_{Mg^{2+}}$. This condition allows us to simplify equation (2.41) to

$$V = -\frac{\mu^{C}_{Mg} - \mu^{A}_{Mg}}{2e} \tag{2.42}$$

To calculate the voltage, we will apply the definition of the chemical potential of neutral Mg in the context of the cathode ($H_xV_2O_5$) and anode (pure Mg metal) materials. Specifically, we will focus on $H_xV_2O_5$ as the cathode material and pure Mg metal as the anode material. Thus, equation (2.42) can be expressed as follows:

$$\begin{aligned} V(y) &= -\frac{\left(\frac{E_{Mg_yH_xV_2O_5} - E_{H_xV_2O_5}}{y}\right) - E_{Mg}}{2e} \\ &= -\frac{E_{Mg_yH_xV_2O_5} - E_{H_xV_2O_5} - yE_{Mg}}{y2e} \end{aligned} \tag{2.43}$$

Using equation (2.43), we conducted calculations to determine the open-circuit voltage (OCV) of Mg insertion into $H_xV_2O_5$-based cathodes with varying H concentrations as a function of Mg concentration.

2.12 Summary of computational details

In this thesis, the all calculations were conducted employing spin-polarized density functional theory (DFT) within the Vienna Ab Initio Simulation Package (VASP 5) (Kresse et al., 1993). Core electron and ion interactions were treated using the projector augmented wave method (Amadon et al., 2008), while valence electrons were expanded in the plane-wave basis set: H 1s, Mg 2s, O 2s2p, and V 3p3d4s, with a kinetic energy cutoff set at 500 eV. For the exchange-correlation functional term, the generalized gradient approximation (GGA) with the Perdew-Burke-Ernzerhof (PBE) approach was utilized. To mitigate self-interaction errors, an effective Hubbard U value of 3.5 eV was applied to the V 3d orbitals (Ngamwongwan et al., 2021; Porsev et al., 2014).

Incorporating van der Waals interactions between the V_2O_5 layers, we employed the optPBE-vdW method (Klimes et al., 2010; Klimeš et al., 2011; John P. Perdew et al., 1996). The insertion of ions was accomplished using a 1x2x2 V_2O_5 supercell. Structural optimization and electronic density of state (DOS) calculations involved a Monkhorst–Pack grid (Monkhorst et al., 1976) of 4×4×4 k-points and 12×12×12 k-points, respectively. A Gaussian smearing method with a width of 0.05 eV was applied. Convergence criteria were set at 10^{-6} eV for the self-consistent field and 0.02 eV/Å for optimization.

To investigate Mg and H diffusion behaviors, a larger 1x3x3 supercell with 4×4×4 k-point sampling was utilized for Brillouin zone coverage. The climbing image nudged elastic band (CI-NEB) method (Henkelman et al., 2000) was employed to determine diffusion paths and barriers. Bader charge analyses (Tang et al., 2009) were performed to ascertain relative charges on each atom.

2.13 References

Amadon, B., Lechermann, F., Georges, A., Jollet, F., Wehling, T. O., and Lichtenstein, A. I. (2008). Plane-wave based electronic structure calculations for correlated materials using dynamical mean-field theory and projected local orbitals. *Physical Review B, 77*(20).

Anisimov, V. I., Zaanen, J., and Andersen, O. K. (1991). Band theory and Mott insulators: Hubbard U instead of Stoner I. *Physical Review B, 44*(3), 943-954.

Born, M., and Oppenheimer, R. (1927). Zur Quantentheorie der Molekeln. *Annalen der Physik, 389*(20), 457-484.

Ceperley, D. M., and Alder, B. J. (1980). Ground State of the Electron Gas by a Stochastic Method. *Physical Review Letters, 45*(7), 566-569.

Dai, X., Liu, Z., and Zhou, A. (2016). A Conjugate Gradient Method for Electronic Structure Calculations. *SIAM Journal on Scientific Computing, 39*.

Fock, V. (1930). Näherungsmethode zur Lösung des quantenmechanischen Mehrkörperproblems. *Zeitschrift für Physik, 61*(1), 126-148.

Grimme, S., Antony, J., Ehrlich, S., and Krieg, H. (2010). A consistent and accurate ab initio parametrization of density functional dispersion correction (DFT-D) for the 94 elements H-Pu. *The Journal of Chemical Physics, 132*(15).

Hartree, D. R. (1928). The Wave Mechanics of an Atom with a Non-Coulomb Central Field. Part I. Theory and Methods. *Mathematical Proceedings of the Cambridge Philosophical Society, 24*(1), 89-110.

Henkelman, G., Uberuaga, B. P., and Jónsson, H. (2000). A climbing image nudged elastic band method for finding saddle points and minimum energy paths. *The Journal of Chemical Physics, 113*(22), 9901-9904.

Hohenberg, P., and Kohn, W. (1964). Inhomogeneous Electron Gas. *Physical Review, 136*(3B), B864-B871.

Hoover, W. G. (1985). Canonical dynamics: Equilibrium phase-space distributions. *Physical Review A, 31*(3), 1695-1697.

Klimes, J., Bowler, D. R., and Michaelides, A. (2010). Chemical accuracy for the van der Waals density functional. *Journal of Physics: Condensed Matter, 22*(2), 022201.

Klimeš, J., Bowler, D. R., and Michaelides, A. (2011). Van der Waals density functionals applied to solids. *Physical Review B, 83*(19).

Kresse, G., and Hafner, J. (1993). Ab initio molecular dynamics for liquid metals. *Phys Rev B Condens Matter, 47*(1), 558-561.

Monkhorst, H. J., and Pack, J. D. (1976). Special points for Brillouin-zone integrations. *Physical Review B, 13*(12), 5188-5192.

Ngamwongwan, L., Fongkaew, I., Jungthawan, S., Hirunsit, P., Limpijumnong, S., and Suthirakun, S. (2021). Electronic and thermodynamic properties of native point defects in V_2O_5: a first-principles study. *Physical Chemistry Chemical Physics, 23*(19), 11374-11387.

Nosé, S. (1984). A unified formulation of the constant temperature molecular dynamics methods. *The Journal of Chemical Physics, 81*(1), 511-519.

Perdew, J. P., Burke, K., and Ernzerhof, M. (1996). Generalized Gradient Approximation Made Simple. *Physical Review Letters, 77*(18), 3865-3868.

Perdew, J. P., and Zunger, A. (1981). Self-interaction correction to density-functional approximations for many-electron systems. *Physical Review B, 23*(10), 5048-5079.

Porsev, V. V., Bandura, A. V., and Evarestov, R. A. (2014). Hybrid Hartree–Fock-density functional theory study of V_2O_5 three phases: Comparison of bulk and layer stability, electron and phonon properties. *Acta Materialia, 75*, 246-258.

Slater, J. C. (1930). Note on Hartree's Method. *Physical Review, 35*(2), 210-211.

Tang, W., Sanville, E., and Henkelman, G. (2009). A grid-based Bader analysis algorithm without lattice bias. *Journal of Physics: Condensed Matter, 21*(8), 084204.

Van der Ven, A., Deng, Z., Banerjee, S., and Ong, S. P. (2020). Rechargeable Alkali-Ion Battery Materials: Theory and Computation. *Chemical Reviews, 120*(14), 6977-7019.

Verlet, L. (1967). Computer "Experiments" on Classical Fluids. I. Thermodynamical Properties of Lennard-Jones Molecules. *Physical Review, 159*(1), 98-103.

มหาวิทยาลัยเทคโนโลยีสุรนารี

CHAPTER III

STRUCTURAL AND ELECTRONIC PROPERTIES OF V_2O_5

Prior to looking into the effect of H insertion on V_2O_5-based cathodes for Mg-ion batteries, we investigated the atomistic configurations and electronic characteristics of the α-V_2O_5 structure. In our study, we used the 1x2x2 α-V_2O_5 supercell as the model for the cathode structure. This initial investigation included a thorough analysis of the geometric arrangement of α-V_2O_5, as presented in detail in section 3.1. Furthermore, we explored the examination of its electronic properties, with discussions provided in section 3.2. To check the geometric and electronic structures of our computational results, we performed a comparison between our findings with other computational calculations and experimental observations.

3.1 Crystal Structure of α-V_2O_5

In this study, we focused on utilizing the α-V_2O_5 phase, specifically the orthorhombic configuration characterized by the Pmmn space group, as a fundamental model. This phase is known for its durability and strength, particularly in the demanding conditions encountered in metal-ion batteries. This durability is because of its unique layered structure, which consists of a network of VO_5 square pyramids that are distorted and connected through both sharing their edges and corners, as depicted in Figure 3.1(a). This results in a notable two-dimensional (2D) layered structure that is limited to the ab plane, as illustrated in Figure 3.1(b).

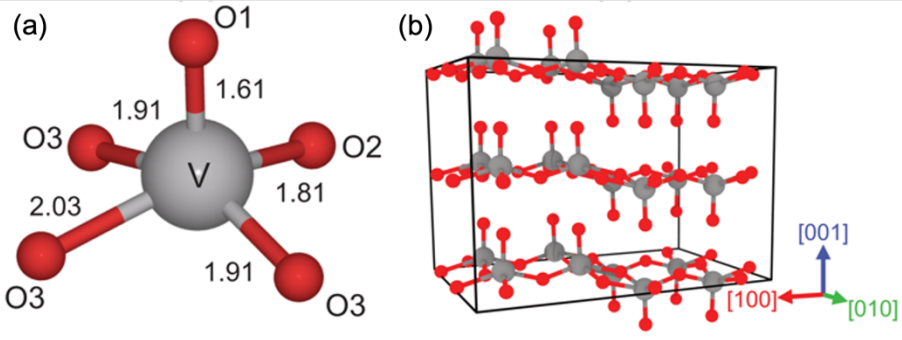

Figure 3.1 Illustrations of (a) VO_5 units, each containing three distinct oxygen atoms denoted as follows: vanadyl oxygen (O1), bridging oxygen (O2), and edge-sharing oxygen (O3) with the bond distance presented in Å unit and (b) an α-V_2O_5 supercell in a 1x2x2 arrangement. The red and grey represent the oxygen and vanadium atom.

Within each VO_5 unit, is characterized by the presence of three distinct oxygen atoms, each serving a specific role. The foremost is the vanadyl oxygen atom (terminal oxygen atom), labeled as O1, with a computed V-O1 bond distance ($d_{V\text{-}O1}$) amounting to 1.61 Å. Accompanying this is the bridging oxygen atom, denoted as O2, exhibiting a V-O2 bond distance ($d_{V\text{-}O2}$) of 1.81 Å. Additionally, a pair of oxygen atoms, O3, engage in an edge-sharing arrangement, resulting in V-O3 bond distances ($d_{V\text{-}O3}$) of 1.91 Å and 2.03 Å, respectively. The geometric arrangement of these oxygen atoms is depicted in Figure 3.1(a).

Our calculations not only provide these bond distances but also align well with both experimental results (Enjalbert et al., 1986) and the other DFT (Ni et al., 2019). Notably, the difference between our calculated values and experimental data is a 1.68% error, while a 1.90% error is with other DFT values. This comparison is highlighted in Table 3.1.

Table 3.1 Lattice parameters and V-O bond distances of α-V_2O_5 obtained from experimental characterizations and computations (values in angstroms unit).

α-V_2O_5	This work	Computations (PBE+U)	Experiment
a	11.60	11.64	11.69
b	7.27	7.15	7.26

Table 3.1 (Continued) Lattice parameters and V-O bond distances of α-V_2O_5 obtained from experimental characterizations and computations (values in angstroms unit).

α-V_2O_5	This work	Computations (PBE+U)	Experiment
c	4.48	4.43	4.42
V-O1	1.61	1.61	1.58
V-O2	1.81	1.80	1.78
V-O3	1.95	1.95	1.93

3.2 Electronic properties

Our research focuses on studying the electronic configuration of α-V_2O_5. We do this by analyzing its density of states (DOS) and band structure, as shown in Figure 3.2(a) and (b), Our calculations reveal that α-V_2O_5 is a semiconductor with an indirect band gap of 2.17 eV. The summary of these band gaps of this work and other computational work is listed in Table 3.2.

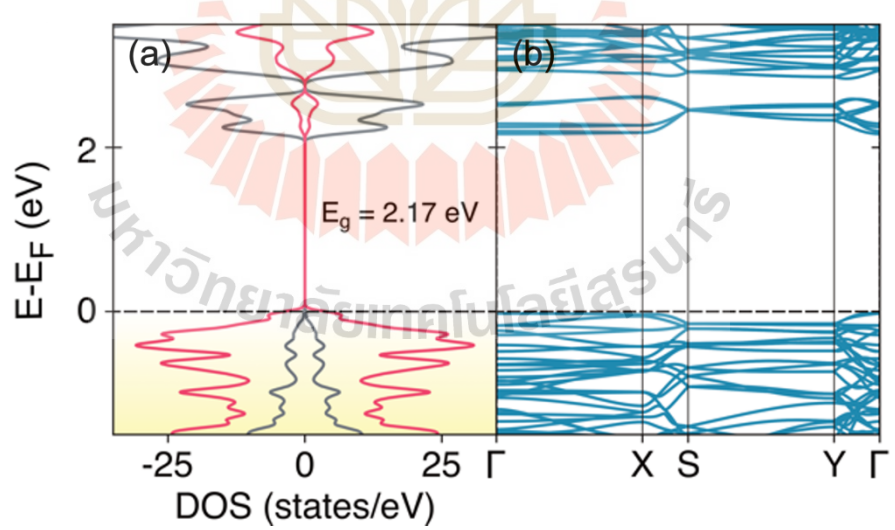

Figure 3.2 (a) The projected density of states and (b) energy band structure of V_2O_5 structure show a non-magnetic semiconducting character with an indirect band gap of 2.17 eV. The red and gray solid lines represent the state of oxygen and vanadium, respectively.

When we examine the projected density of states (PDOS), we see a non-magnetic profile. This means there are an equal number of states for both spin components, as shown in Figure 3.2(a). The valence band is mainly affected by O 2p orbitals, with some mixing involving V 3d states. On the other hand, the conduction band is dominated by V 3d states, with some mixing with O 2p orbitals. This unique band arrangement is a result of changes in the symmetry of the VO_5 units, which has been observed in previous research (Maganas et al., 2013) and (Tolhurst et al., 2016). This analysis of α-V_2O_5's electronic properties shows how its structural complexities significantly influence its electronic behavior.

An important observation to highlight is the capacity of the computational approach to yield more accurate electronic structures and enhance band gap predictions for various semiconducting materials. Notably, the Quasiparticle GW approximation and the utilization of hybrid functionals have proven invaluable in this regard.

In the case of V_2O_5, as shown in Table 3.2, only the Quasiparticle GW method is able to accurately match the experimental band gap value. This highlights the accuracy of the GW method in capturing the complex electronic behavior of V_2O_5, especially concerning its band gap characteristics. On the other hand, the use of hybrid functionals (PBE0) leads to overestimating the band gap.

Table 3.2 Calculated band gaps of α-V_2O_5 using different methods.

Method	E_g (eV)	References
DFT+U (U=3.5)	2.17	This work
DFT+U (U=4.0)	2.17	(Zhou et al., 2014)
DFT+U (U=2.0)	1.66	(Ni et al., 2019)
DFT+U (U=3.5)	2.18	(Ngamwongwan et al., 2021)
DFT+U (U=4.0)	2.26	(Scanlon et al., 2008)
PBE0	4.04	(Porsev et al., 2014)
GW	2.3	(Bhandari et al., 2015)
GW	2.89	(Roginskii et al., 2021)

Table 3.2 (Continued) Calculated band gaps of α-V_2O_5 using different methods.

Method	E_g (eV)	References
Experiment	2.3	(Enjalbert et al., 1986)

The contrast in the performance of different computational methods for V_2O_5 highlights the importance of choosing the method for studying specific materials. The unique electronic structure of V_2O_5, as revealed by these comparisons, offers insights into the material's complex behavior, demonstrating the interplay between theory and experimentation in the field of materials characterization.

In this chapter, we focused on the structural and electronic properties of α-V_2O_5, emphasizing its stable orthorhombic phase and its ability to host small cations within its layered structure, making it a promising candidate for cathodes in metal-ion batteries. This analysis provided crucial context for our research. Now, in the next chapter, we will explore the interactions of H and Mg within the α-V_2O_5 structure, elucidating their impacts on electronic conductivity, diffusion kinetics, and structural stability.

3.3 References

Bhandari, C., Lambrecht, W. R. L., and van Schilfgaarde, M. (2015). Quasiparticle self-consistent GW calculations of the electronic band structure of bulk and monolayer V_2O_5. *Physical Review B, 91*(12).

Enjalbert, R., and Galy, J. (1986). A refinement of the structure of V_2O_5. *Acta Crystallographica Section C, 42*(11), 1467-1469.

Maganas, D., Roemelt, M., Havecker, M., Trunschke, A., Knop-Gericke, A., Schlogl, R., and Neese, F. (2013). First principles calculations of the structure and V L-edge X-ray absorption spectra of V_2O_5 using local pair natural orbital coupled cluster theory and spin-orbit coupled configuration interaction approaches. *Physical Chemistry Chemical Physics, 15*(19), 7260-7276.

Ngamwongwan, L., Fongkaew, I., Jungthawan, S., Hirunsit, P., Limpijumnong, S., and Suthirakun, S. (2021). Electronic and thermodynamic properties of native point

defects in V_2O_5: a first-principles study. *Physical Chemistry Chemical Physics, 23*(19), 11374-11387.

Ni, D., Shi, J., Xiong, W., Zhong, S., Xu, B., and Ouyang, C. (2019). The effect of protons on the Mg^{2+} migration in an alpha-V_2O_5 cathode for magnesium batteries: a first-principles investigation. *Physical Chemistry Chemical Physics, 21*(14), 7406-7411.

Porsev, V. V., Bandura, A. V., and Evarestov, R. A. (2014). Hybrid Hartree–Fock-density functional theory study of V_2O_5 three phases: Comparison of bulk and layer stability, electron and phonon properties. *Acta Materialia, 75*, 246-258.

Roginskii, E. M., Smirnov, M. B., Smirnov, K. S., Baddour-Hadjean, R., Pereira-Ramos, J.-P., Smirnov, A. N., and Davydov, V. Y. (2021). A Computational and Spectroscopic Study of the Electronic Structure of V_2O_5-Based Cathode Materials. *The Journal of Physical Chemistry C, 125*(10), 5848-5858.

Scanlon, D. O., Walsh, A., Morgan, B. J., and Watson, G. W. (2008). An ab initio Study of Reduction of V_2O_5 through the Formation of Oxygen Vacancies and Li Intercalation. *The Journal of Physical Chemistry C, 112*(26), 9903-9911.

Tolhurst, T. M., Leedahl, B., Andrews, J. L., Marley, P. M., Banerjee, S., and Moewes, A. (2016). Contrasting 1D tunnel-structured and 2D layered polymorphs of V_2O_5: relating crystal structure and bonding to band gaps and electronic structure. *Physical Chemistry Chemical Physics, 18*(23), 15798-15806.

Zhou, B., Shi, H., Cao, R., Zhang, X., and Jiang, Z. (2014). Theoretical study on the initial stage of a magnesium battery based on a V_2O_5 cathode. *Physical Chemistry Chemical Physics, 16*(34), 18578-18585.

CHAPTER IV

THE INSERTION OF HYDROGEN AND MAGNESIUM INTO V_2O_5

In the previous chapter, we investigated the geometric structure of α-V_2O_5 and investigated its electronic properties, establishing its suitability as a cathode material for Mg-ion batteries. Now, we shift our focus to a study of the effects of H and Mg insertion into V_2O_5-based cathode materials on battery performance. Next, we further initiate our investigation by examining the insertion of a single H atom into V_2O_5, looking into the structural and electronic consequences of this insertion as discussed in section 4.1. Next, we investigate the impact of varying H concentrations in $H_xV_2O_5$ cathode materials, with a particular focus on their thermodynamic and electronic properties. This analysis involves calculating formation energies and analyzing bond distances to uncover the underlying mechanisms, as discussed in section 4.2. Afterward, we assess the stability of the fully H-inserted V_2O_5 structure under various temperature conditions using AIMD, as outlined in section 4.3. In the final part of our study, we investigate the intercalation of Mg ions into the V_2O_5 cathode, aiming to understand the structural and electronic implications of this insertion as discussed in section 4.4.

มหาวิทยาลัยเทคโนโลยีสุรนารี

4.1 H insertion into V_2O_5

The evidence supports the significant capacity enhancement of Mg-ion batteries when utilizing water-containing electrolytes, as demonstrated in various experimental studies (Karapidakis et al., 2021; Wang et al., 2017). In the discharge process of these batteries, water molecules present in the electrolyte undergo dissociation, resulting in the formation of H^+ and OH^- ions. Subsequently, both H^+ ions and Mg^{2+} ions exhibit the ability to intercalate into the V_2O_5 cathode structure, leading to a notable increase in its capacity (Pan et al., 2016; Wan et al., 2018). This phenomenon is corroborated by the observed rise in pH levels during the discharge process (Liu et al., 2020).

In this context, the present study aims to provide an insight into the influence of H^+ and Mg ion intercalation on the structural and electronic characteristics of the V_2O_5 cathode. To achieve this, we conducted ion insertion simulations within the 1x2x2 V_2O_5 supercell. Subsequently, we conducted a calculation of the local structure and density of states, paying specific attention to how these characteristics change with different ion concentrations. This investigation seeks to elucidate the mechanisms underlying the capacity enhancement observed in Mg-ion batteries utilizing aqueous-containing electrolytes.

Our primary objective was to determine the most favorable location for the insertion of H within the V_2O_5 structure. We directed our attention to the three distinct oxygen sites within V_2O_5. To quantify the insertion energy associated with these sites, we employed the following equation, denoted as (4.1)

$$E_{ins}^{H} = E_{HV_{16}O_{40}} - E_{V_{16}O_{40}} - 1/2\mu_{H_2} \tag{4.1}$$

When $E_{HV_{16}O_{40}}$ and $E_{V_{16}O_{40}}$ is the total energy of H-inserted V_2O_5 and V_2O_5 structure. The μ_{H_2} is the chemical potentials of hydrogen molecule.

The configurations for H insertion and their respective insertion energies are depicted in Figure 4.1. Our calculations yielded insertion energies of -0.64 eV for the O1 site, -0.30 eV for the O2 site, and -0.14 eV for the O3 site. Notably, these results imply that the insertion energy decreases as the number of bonds associated with the oxygen atom increases, leading to a more stable configuration.

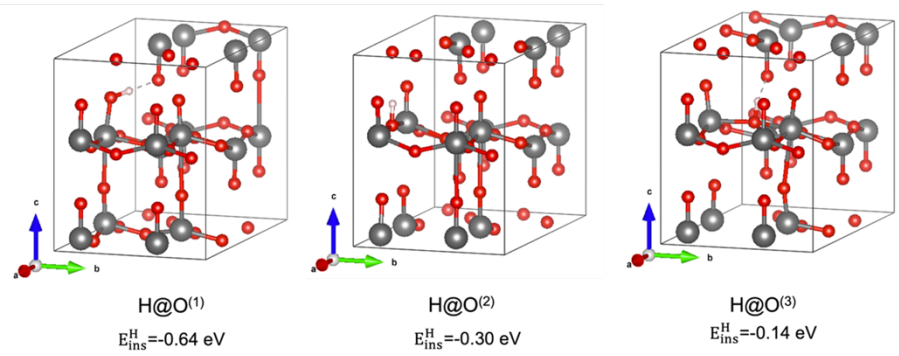

Figure 4.1 Representation of various hydrogen insertion configurations in V_2O_5.

This finding underlines the importance of considering the bonding environment of the oxygen atom when determining the optimal site for H insertion in V_2O_5. The lower insertion energies for sites with a greater number of oxygen bonds suggest that these configurations are energetically favorable and likely to occur in practice.

Our investigation revealed that H exhibits a preference for binding with the vanadyl oxygen O1 atom, forming an O-H bond with a distance of 0.99 Å and an insertion energy of -0.64 eV. This particular configuration is more stable than those observed at O2 and O3.

Furthermore, the direction of the O-H bond points towards the adjacent O1 atom, leading to the formation of a hydrogen bond (H-bond) at a distance of 0.99 Å, as illustrated in Figure 4.2. The H-bond causes a slight distortion in the VO_5 unit, leading to elongated V-O1, V-O2, and V-O3 bonds, with distances measuring 1.80 Å, 1.86 Å, and 1.96 Å, respectively. (refer to Figure 4.2). These findings highlight the specific structural changes and bonding interactions that occur upon H insertion into V_2O_5, highlighting the significance of the O1 site as the preferred location for H binding.

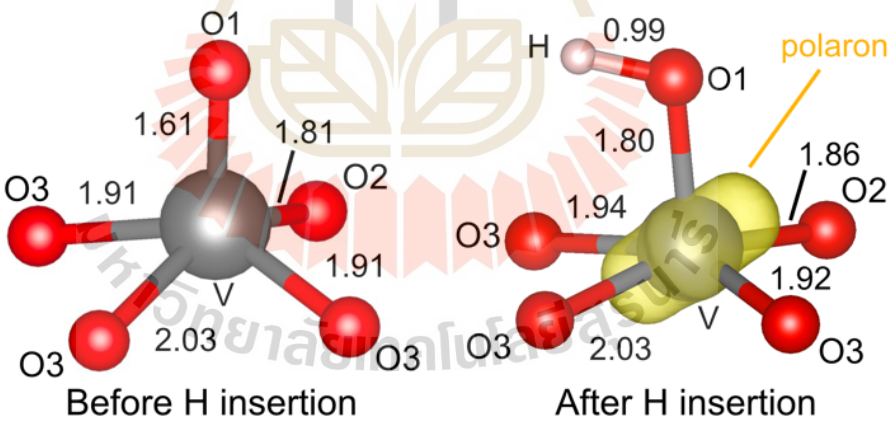

Figure 4.2 Demonstration of minor distortion of a VO_5 unit, accompanied by electron localization at the V center, referred to as a small polaron. The labeled numbers correspond to their respective bond distances in angstrom. The yellow isosurface at 0.032 e $Å^{-3}$ highlights the electron localization.

Our Bader charge analysis and spin density calculations have provided insights into the ionization behavior of the H atom upon insertion into the V_2O_5 structure.

Specifically, we observed that the H atom ionizes during this process, transforming into H^+ with 0.63 electrons transferred to become localized at the connected V center, as depicted in Figure 4.2.

Moreover, the examination of the gap state, which involves hybridized V 3d and O 2p orbitals, further supports the localization of this electron, as illustrated in Figure 4.3. This phenomenon of electron localization, accompanied by the concurrent local lattice distortion, is well-documented and recognized as the formation of a small polaron (De Jesus et al., 2018; Suthirakun et al., 2018).

These findings shed light on the electronic and structural changes that occur upon H insertion into the V_2O_5 cathode material, and they contribute to our understanding of the underlying mechanisms driving battery performance enhancement in Mg-ion batteries.

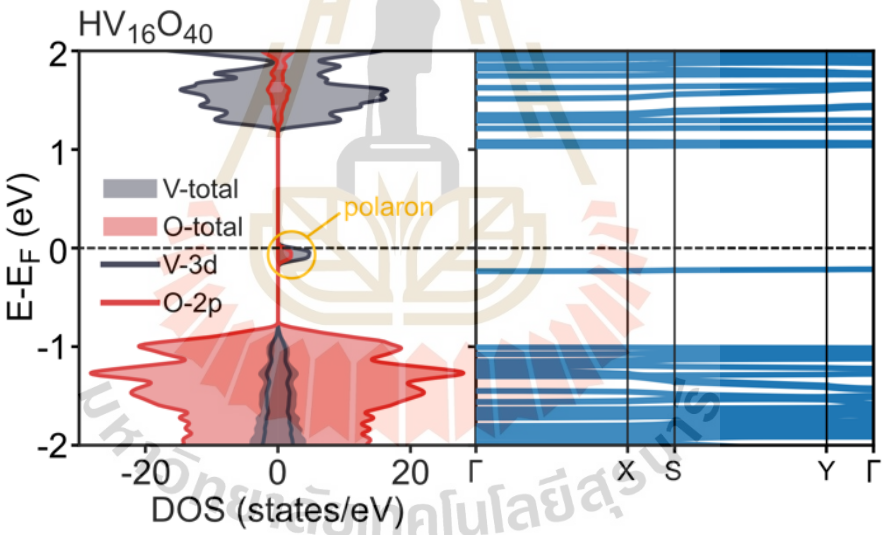

Figure 4.3 A visual representation of a gap state within both the projected density of states and the band structure for the $HV_{16}O_{40}$ structure.

The relationship between the d-orbitals of vanadium atoms and the formation of polarons at V centers due to hydrogen insertion into V_2O_5 can be elucidated through an analysis of the electronic structure and bonding characteristics of the system. When H ions are introduced into the V_2O_5 lattice, they have the capacity to induce localized

electronic states within the crystal structure, resulting in the creation of polarons, as depicted in Figure 4.4.

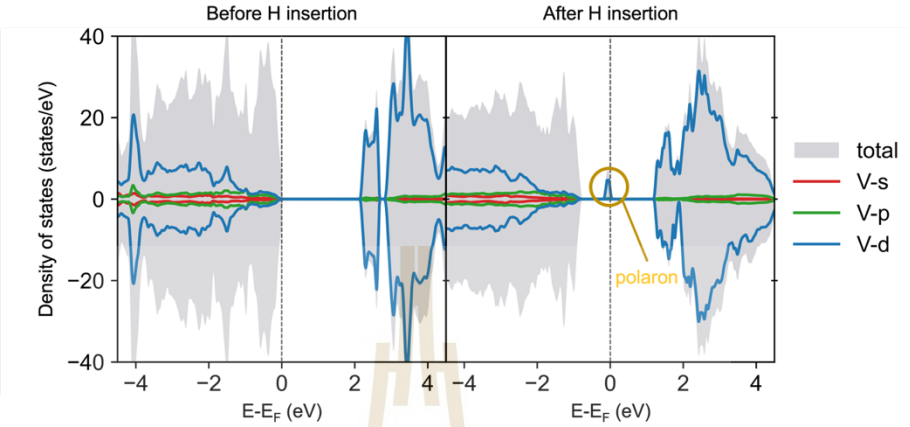

Figure 4.4 The density of state (DOS) of V_2O_5 before and after H insertion. the total DOS was show in gray filled color and the partial DOS projected on s, p and d state of V atom was represented in red, green and blue solid line, respectively.

As shown in Figure 4.4, after H insertion, the primary components of the gap state in the resulting polaron are the d-orbitals related to V atoms. These d-orbitals engage with the H ions and contribute to the bonding process during the insertion. This interaction between H ions and V atoms is crucial for generating new electronic states that become concentrated near the V centers.

The confinement of these electronic states, resulting from H insertion, is often linked to the engagement of V atom d-orbitals. This observation highlights the vital role of V atoms and their d-orbitals in the electronic structure and charge distribution dynamics during H insertion in V_2O_5. It enhances our understanding of the fundamental mechanisms that drive this process.

4.2 Effect of H Concentration on $H_xV_2O_5$

We conducted an investigation of the formation energy for H insertion at the O1 position within the α-V_2O_5 structure, using the following equation (4.2)

$$E_f(x) = \frac{E_{H_xV_2O_5} - E_{V_2O_5} - x/2\mu_{H_2}}{x} \quad (4.2)$$

where $E_{V_2O_5}$ and $E_{H_xV_2O_5}$ represent the total energies of the V_2O_5 supercell in the absence and presence of intercalated H atoms, respectively, and μ_{H_2} denotes the chemical potential of the isolate H_2 molecule.

Formation energy calculations can assess the energy required for the incorporation of H atoms into various O1 sites within the α-V_2O_5 structure. A lower formation energy value indicates greater thermodynamic stability, implying a more favorable configuration for H insertion at that specific concentration. Our formation energy calculations yielded the following values (in eV) for different H concentrations (x): $H_xV_2O_5$ with x = 0.5 (-0.81 eV), $H_xV_2O_5$ with x = 1 (-0.86 eV), $H_xV_2O_5$ with x = 1.5 (-0.92 eV) and $H_xV_2O_5$ with x = 2 (-0.91 eV).

As illustrated in Figure 4.5, these results reveal that the configuration denoted as $H_2V_2O_5$ exhibits a trend of increasing formation energy as the H concentration increases.

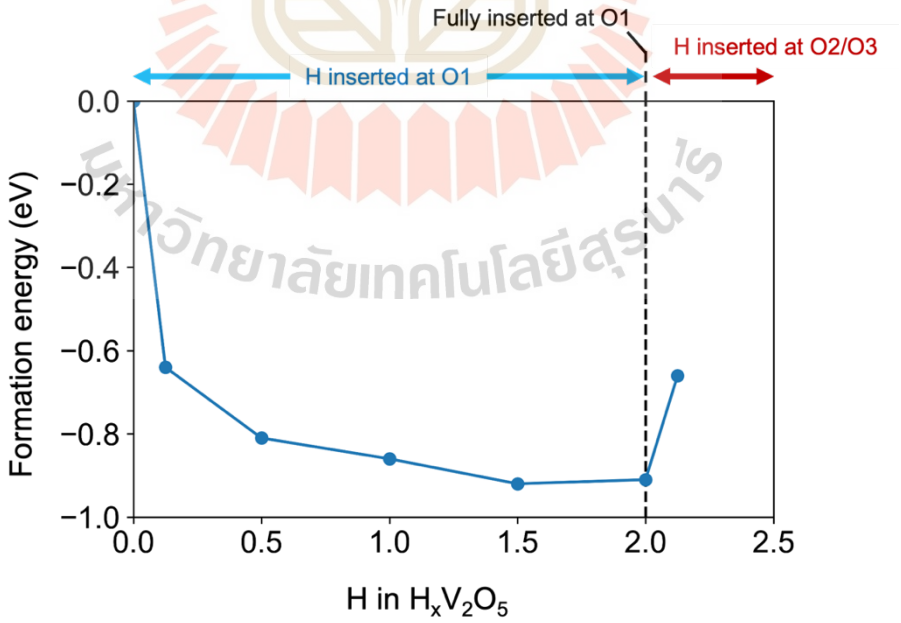

Figure 4.5 The formation energy profile of H insertion into V_2O_5.

Additionally, we computed the formation energy for inserting a single H atom into positions O2 and O3 of the fully hydrogenated V_2O_5 structure, represented as $H_2V_2O_5$. The calculated formation energies were -0.66 eV and -0.65 eV for the O2 and O3 positions, respectively. Notably, these results suggest a substantial increase in formation energy compared to that of $H_2V_2O_5$ (-0.91 eV), signifying a thermodynamically unfavorable trend, as detailed in Figure 4.5. This observation implies that the thermodynamic feasibility of further hydrogen insertion diminishes as the concentration exceeds x = 2 in $H_xV_2O_5$, leading to the formation of $H_2V_2O_5$ at maximum O1 sites. Consequently, the highest hydrogen insertion capacity is achieved at x = 2. Subsequent increases in the formation energy trend beyond x = 2 suggest a decreasing thermodynamic favorability for additional hydrogen insertion.

These findings provide insights into the thermodynamic stability of different H insertion configurations within V_2O_5. These results offer a better understanding of the thermodynamic stability of various H insertion in V_2O_5, revealing the ideal conditions for maximizing H insertion capacity in the material. It is indeed noteworthy that our calculated formation energies suggest that the H concentration in V_2O_5 can reach up to $H_2V_2O_5$, where the formation energy for H incorporation at O1 is highly negative (-0.92 eV). Beyond this point, further H insertion would necessitate protonation of O2 or O3 sites, which are energetically less stable with formation energies of -0.65 eV and -0.66 eV, respectively.

In our subsequent investigation, we increased the H concentrations in the supercell, varying the number of H atoms from 4 to 16, corresponding to $H_xV_2O_5$ with x ranging from 0.5 to 2. As depicted in Figure 4.6, we observed a notable trend: the average V-O bond distance increased with rising H concentrations. Specifically, the V-O1 bond distances exhibited a significant increase, transitioning from 1.61 Å (at x = 0) to 2.04 Å (at x = 2), while other V-O bonds exhibited only minor changes. In contrast, the O-H bond tended to shorten with increasing H concentration.

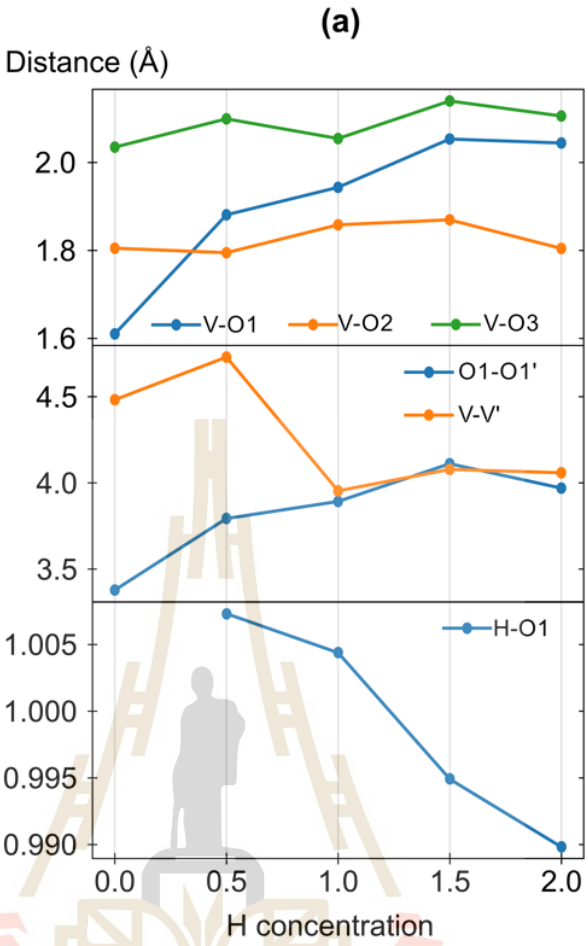

Figure 4.6 Illustratration of the impact of varying hydrogen content on the local structures of α-V_2O_5, focusing on V-O bond lengths, O1-O1' distances, and V-V' distances in the [100] direction, as well as H-O1 bond lengths.

These results imply that higher H concentrations within the V_2O_5 structure lead to stronger O-H bonds but weaker V-O bonds. Moreover, higher H concentrations affect the distortion of lattice parameters in the α-V_2O_5 host. The lattice parameters, a, b, and c, transitioned from 11.60 Å, 7.27 Å, and 8.96 Å to 12.29 Å, 7.54 Å, and 8.12 Å, respectively, in the case of $H_2V_2O_5$. However, as per the findings of Jesus and Sai (De Jesus et al., 2018; Sai Gautam et al., 2015), despite the changes in lattice parameters, the α-V_2O_5 phase remained unchanged, which was further confirmed by the puckering angle analysis. The puckering angle shifted from 77.43° to 88.65° in $H_2V_2O_5$, suggesting that the α-phase of V_2O_5 was maintained. This increased puckering angle in $H_2V_2O_5$ is

attributed to repulsive forces introduced by the H ions between the O1 atoms in the crystal lattice.

These findings offer insights into the structural and bonding changes induced by varying H concentrations in V_2O_5. Furthermore, the presence of intercalated H atoms plays a crucial role in widening the ion-diffusion pathways within the V_2O_5 cathode, especially in the [010] direction. This expansion is evident in the increased distance between the nearest O1-O1 sites, which goes from 3.37 Å to 3.53 Å. Such an expansion of the diffusion pathways has the potential to improve the ion transport kinetics of the cathode, a topic that will be explored further in chapter 5.

To gain a understanding of the electronic structures of $H_xV_2O_5$, we conducted an analysis of their PDOS. As illustrated in Figure 4.7(a), an increase in H concentrations correlates with a narrowing of the band gap. For instance, at x = 0.5, the additional electrons introduced by the inserted H atoms occupy multiple V centers, resulting in occupied extra states situated at the uppermost region of the valence band, as seen from the band decomposed charge density shown in Figure 4.7(b).

มหาวิทยาลัยเทคโนโลยีสุรนารี

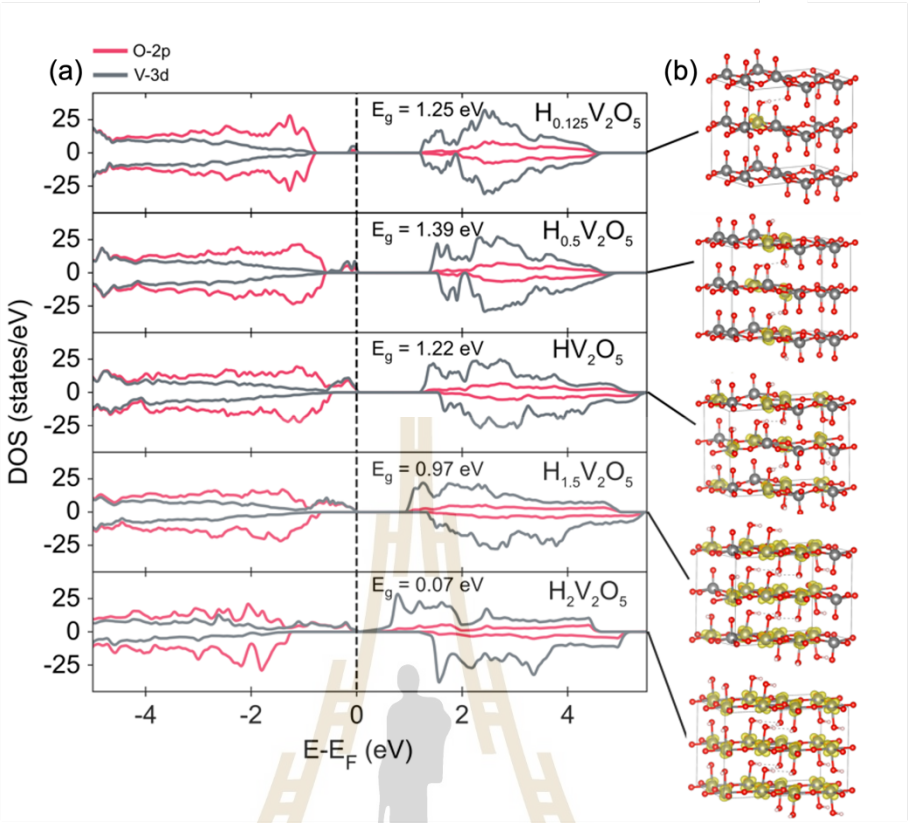

Figure 4.7 (a) The electronic structures in the projected density of states of $H_xV_2O_5$ structure. It is evident that increasing hydrogen content leads to a reduction in band gaps. (b) The additional electrons resulting from the inserted hydrogen occupy V centers, creating states located at the uppermost portion of the valence band. This phenomenon is represented by the yellow isosurface at 0.032 e $Å^{-3}$.

As H concentrations increase (x = 1 and 1.5), these additional occupied states extend towards the conduction band, resulting in smaller band gaps. When x reaches 2, the band gap is reduced to 0.07 eV, a value close to the thermal energy at room temperature (0.03 eV). This tiny band gap suggests that the material displays metal-like characteristics at room temperature. This metallic behavior is like the one observed in Li-intercalated V_2O_5 systems, where higher Li concentrations can induce itinerant behavior among the additional electrons (De Jesus et al., 2018). Consequently, the material is expected to demonstrate metallic properties at high H contents.

Based on our computational findings, it suggest that the electronic conductivity of V_2O_5 undergoes substantial improvement upon H intercalation during the discharge

process. This enhancement in electronic conductivity has the potential to significantly impact the overall performance of V_2O_5 as a cathode material in Mg-ion batteries.

Our calculation reveals that while there is a general trend of decreasing band gap with increasing H concentrations in $H_xV_2O_5$, certain arrangements of H atoms and their associated polarons can lead to non-symmetric distributions and localized structural distortions. The variation in the band gap of $H_xV_2O_5$ with increasing H concentrations is indeed a complex phenomenon influenced by multiple factors, including the electronic structure, lattice distortions, and changes in the local environment.

In the cases of $H_{0.5}V_2O_5$, HV_2O_5, $H_{1.5}V_2O_5$, and $H_2V_2O_5$, the observed decrease in the band gap with increasing H concentrations aligns with the general trend identified in our study. This suggests that the presence of H atoms at certain positions within the crystal structure promotes electronic conductivity that results in a narrower band gap.

However, for $H_{0.125}V_2O_5$ and $H_{0.25}V_2O_5$, where the H atoms exhibit non-symmetry between the V_2O_5 layers, as depicted in Figure 4.8(a) and (b), the trend of decreasing band gap with increasing H concentrations may not conform to the general trend observed, as shown in Figure 4.8(d)-(f). This variation in behavior can be attributed to the specific spatial arrangement of H atoms, which can introduce localized distortions or interactions that affect the electronic properties compared to symmetric configurations.

มหาวิทยาลัยเทคโนโลยีสุรนารี

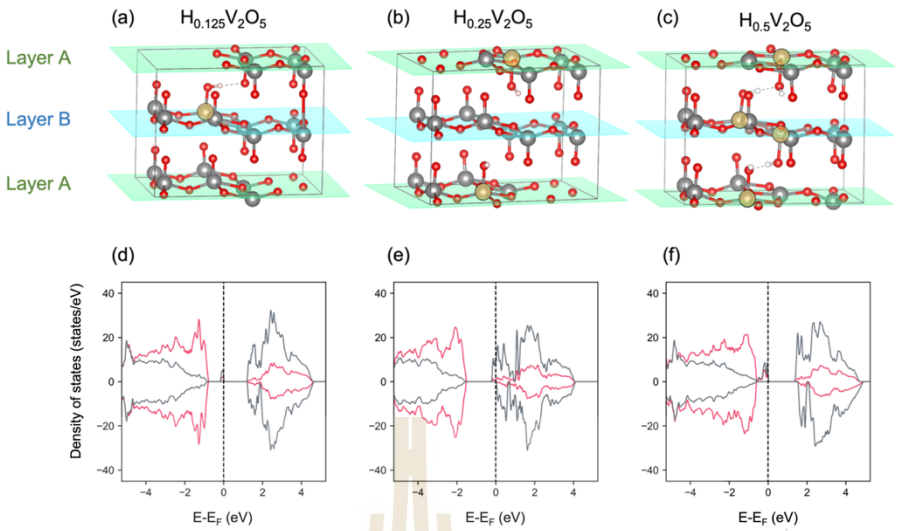

Figure 4.8 The polaron localized at each V_2O_5 layer for (a) $H_{0.125}V_2O_5$, (b) $H_{0.25}V_2O_5$, and (c) $H_{0.25}V_2O_5$. The projected density of states of (d) $H_{0.125}V_2O_5$, (e) $H_{0.25}V_2O_5$, and (f) $H_{0.25}V_2O_5$. the gray, red, and white colors represented vanadium, oxygen, and hydrogen, respectively.

The non-symmetric distribution of H atoms within the V_2O_5 layers can lead to the formation of asymmetric charge distributions, all of which can impact the electronic structure and modify the band gap. These findings underscore the relationship between the arrangement of H atoms, crystal symmetry, and resulting electronic properties within the $H_xV_{16}O_{40}$ structure, resulting in deviations from the expected trend of band gap reduction.

In summary, the band gap behavior in $H_xV_2O_5$ is not only determined by H concentrations but is also related to the specific arrangement of H atoms and resulting structural and electronic consequences. These complexities necessitate a detailed understanding of the interplay between H insertion, crystal structure, and electronic properties for the design and optimization of $H_xV_2O_5$ as a cathode material in Mg-ion batteries.

4.3 Thermal Stability Investigation of $H_2V_2O_5$ Structure

To investigate the thermal stability of the $H_2V_2O_5$ structure, we performed the AIMD simulations at different temperatures, specifically at 300, 600, and 900K. These simulations were conducted within a Nose-Hoover thermostat (Hoover, 1985; Nosé, 1984), employing an NVT ensemble with a total simulation duration of 1 picosecond and a time step of 0.5 femtoseconds. The k-points sampling method utilized the Gamma point.

To assess the bond distances of O-H pairs within the $H_2V_2O_5$ structure under varying temperatures, we employed the radial distribution function (RDF). The RDF is a pair correlation function that characterizes the spatial distribution of particles within a system. It provides insights into the finding of a particle at a specific distance from a reference particle. The RDF is mathematically defined as equation (4.3)

$$g(r) = \frac{V}{N}\frac{\Delta N(r)}{4\pi r^2 \Delta r} \tag{4.3}$$

where $g(r)$ is the radial distribution function as a function of the distance (r), N is the total number of particles in the system, V is the volume of the system, $\Delta N(r)$ is the number of particles found in the spherical shell of radius r to $r + \Delta r$ around a reference particle, and Δr is the differential distance.

By analyzing the RDF of O-H pairs at different temperatures, we gain insights into how the O-H bond distances within the $H_2V_2O_5$ structure evolve as a function of temperature. This data is essential for evaluating the material's thermal stability, especially in the context of its potential use as a cathode in Mg-ion batteries. Our AIMD simulations reveal that the $H_2V_2O_5$ structure maintains thermal stability even at high temperatures of 300, 600, and 900K, as shown in the thermal stability profile in Figure 4.9. Additionally, the RDF analysis of the O-H bond in $H_2V_2O_5$, as shown in Figure 4.9(b), reveals only minor changes in the bond distances with increasing temperature.

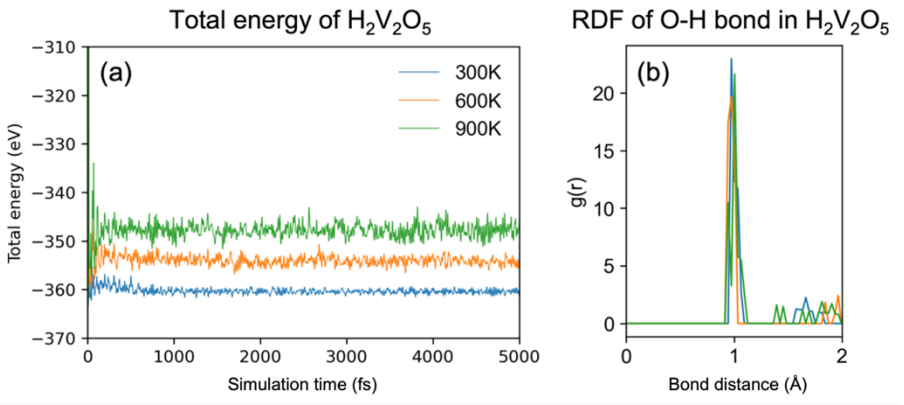

Figure 4.9 (a) The thermal stability investigation in total energy evolution using AIMD simulation at 300K, 600K and 900K. (b) The RDF of the O-H bond in $H_2V_2O_5$ at the last time frame for 300K, 600K and 900K. The blue, orange, and green line represented for 300K, 600K and 900K, respectively.

Specifically, the RDF calculations for the O-H pair exhibit peaks at approximately 0.99 Å, 0.99 Å, and 1.01 Å for temperatures of 300K, 600K, and 900K, respectively. These results suggest that the O-H bond remains stable even at high temperatures. While our thermal stability investigation may not directly elucidate the stability of $H_2V_2O_5$ in the context of the electrochemical process, it does imply that $H_2V_2O_5$ retains its structural stability even in challenging environments. This property underscores its potential suitability as a cathode material in Mg-ion batteries, where stability in non-friendly environments is a crucial factor for long-term performance.

มหาวิทยาลัยเทคโนโลยีสุรนารี

4.4 Mg Intercalation in V_2O_5

In our study of Mg insertion into the V_2O_5 structure, we explored two potential ion-polaron configurations. Given the presence of a divalent Mg atom, it has the capacity to donate two electrons, which can become localized at any of the eight V centers surrounding the Mg atom. To investigate the most stable configuration of electron localization resulting from Mg insertion into V_2O_5, we considered two distinct configurations of electron localization, as depicted in Figure 4.10.

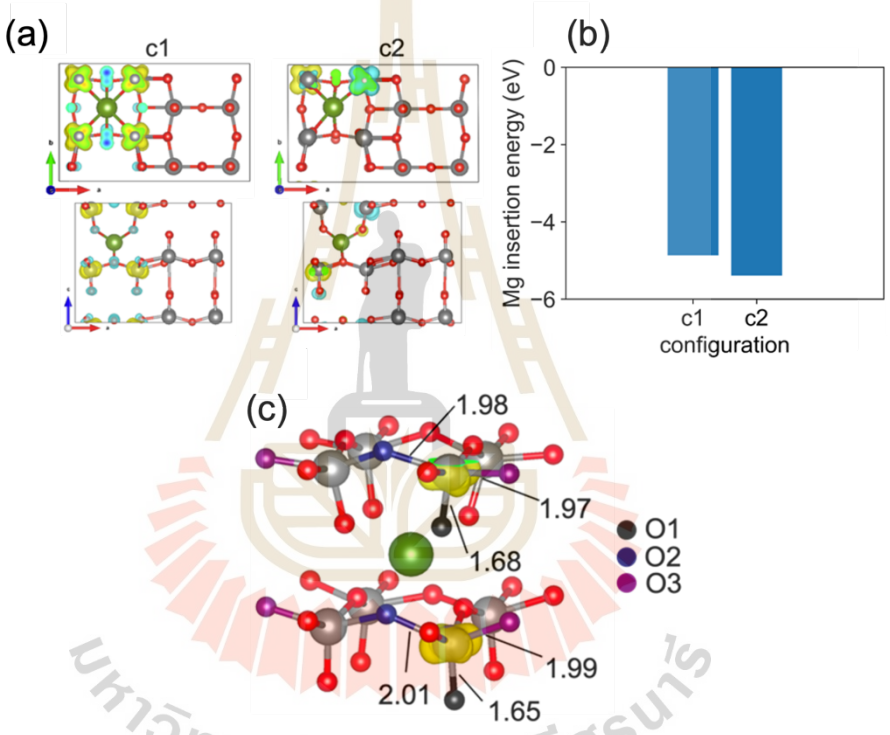

Figure 4.10 Electron localized configuration for Mg insertion into $V_{16}O_{40}$. (a) two configurations of electron localized. (b) total energy of each configuration. (c) bond distance of V-O in Å unit of the most stable configuration.

Our computational analysis revealed that the most stable configuration corresponds to the localization of the two electrons from the Mg atom at two V centers. This finding provides crucial insights into the preferred electron localization behavior associated with Mg insertion into V_2O_5, which is fundamental for understanding the charge distribution and electronic properties in this system.

Our investigation reveals that the most stable configuration of Mg insertion into V_2O_5 involves the localization of the two electrons provided by the Mg atom at two nearby V centers, resulting in the formation of two polarons. This configuration is associated with a favorable insertion energy of -5.39 eV, suggesting its thermodynamic stability.

Conversely, the alternative configuration, where the two electrons are distributed among eight V centers, is less stable, characterized by an insertion energy of -4.87 eV (as depicted in Figure 4.10).

These results imply that upon intercalation, the Mg atom ionizes and contributes two electrons, both of which become localized at the two adjacent V centers. This phenomenon is evident in the spin density (Figure 4.11(a)) and is further supported by the presence of localized gap states in the projected density of states (PDOS) plot (Figure 4.11(b)).

The formation of polarons has important implications for the electronic structure and charge distribution in the Mg-inserted V_2O_5 system, which is significant for understanding the material's behavior as a cathode material in Mg-ion batteries.

มหาวิทยาลัยเทคโนโลยีสุรนารี

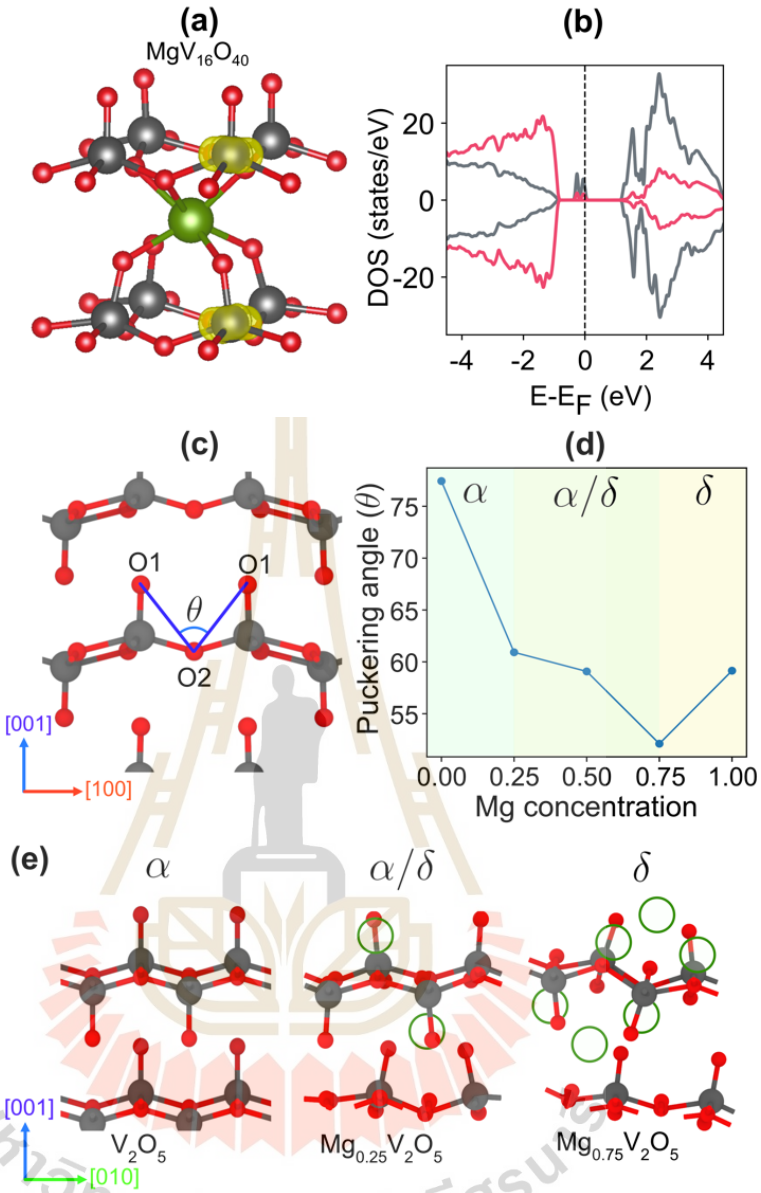

Figure 4.11 Sketches of Mg Insertion and its Impact on α-V_2O_5. (a) Depicts the local structure after Mg insertion into α-V_2O_5. Upon insertion, Mg ionizes and generates two polarons at neighboring VO_5 units, represented by the yellow isosurface. (b) Shows the corresponding gap states in the projected density of states resulting from the formation of these polarons. (c) Demonstrates the effect of high Mg concentrations on the α-V_2O_5 phase transition, as characterized by the puckering angle of O1-O2-O1. (d) Displays how the puckering angle decreases with increasing Mg concentration. (e) Depicts the structural transformation from the α-phase to the δ-phase as a consequence of Mg insertion.

Our investigation reveals that the insertion of Mg into V_2O_5 induces greater in-plane distortion compared to H insertion. The formation of two polarons and electrostatic interactions between Mg^{2+} ions and electronegative oxygen atoms contribute to this distortion. Specifically, the in-plane V-O2 and V-O3 bond lengths exhibit elongation greater than that observed during H insertion, with differences of up to 0.1 Å.

Nevertheless, it's crucial to highlight that H insertion leads to a more elongation of the V-O1 bond compared to Mg insertion (1.80 vs. 1.67 Å). This happens because the introduced H forms a chemical bond with O1, which subsequently weakens the V-O1 bond, resulting in a greater bond length.

Due to the in-plane distortion caused by Mg insertion, it is expected that increased Mg content could result in structural distortion over long distances and trigger a phase transition. To investigate this, we measured the puckering angle (θ) of O1-O2-O1 within the layer, as shown in Figure 4.11(c). It is known that α-V_2O_5 exhibits a puckering angle of 76°, which decreases to 54° when transitioning to the δ-phase (Sai Gautam et al., 2015). As depicted in Figure 4.11(c) , (d), and (e), we observed a decrease in the puckering angle from 76° to 52° and 60° as the Mg concentration increased from x = 0 to 0.75 and 1.00, respectively. These results suggest that the V_2O_5 phase transitions from α to δ at Mg concentrations higher than 0.75, as illustrated in Figure 4.11(d), which corresponds with the structures shown in Figure 4.11(e).

Notably, at higher Mg concentrations, the electronic structures are similar to those observed during H insertion. The band gap decreases with increasing Mg concentration, as demonstrated in Figure 4.12.

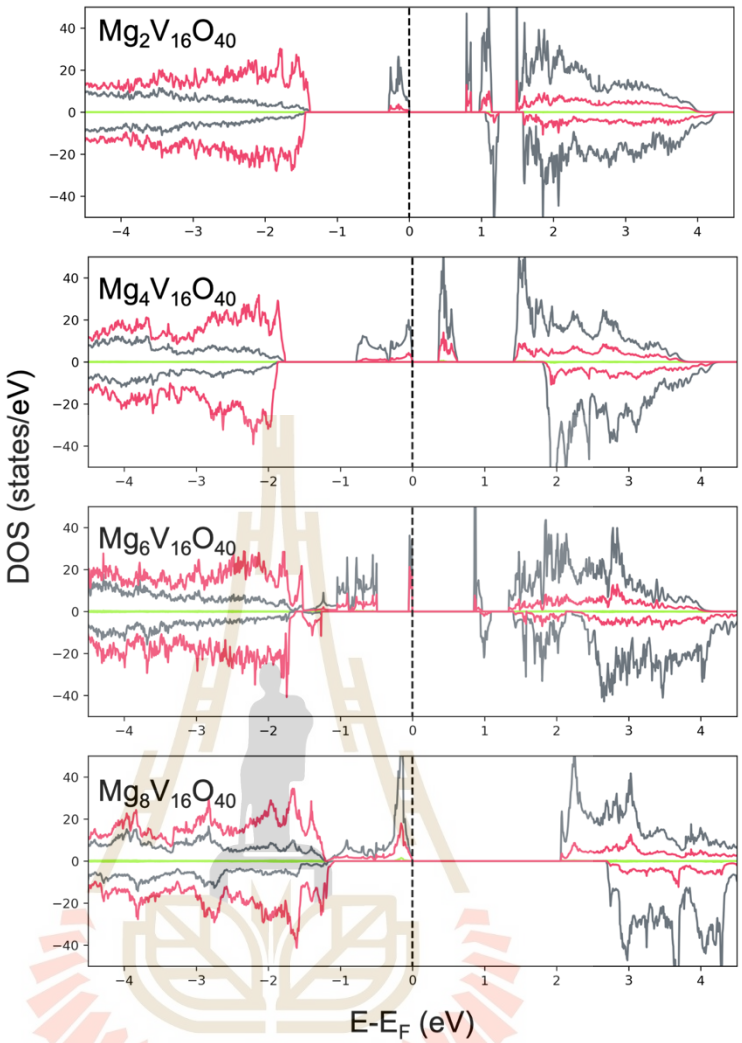

Figure 4.12 Density of state of $Mg_yV_{16}O_{40}$ (y=2,4,6 and 8). The red, grey and green line represented oxygen, vanadium and magnesium state.

In summary, our findings indicate a shift in the electronic properties of V_2O_5 from a high band gap semiconductor to a low band gap semiconductor at high H contents. This transition is primarily attributed to the emergence of additional states resulting from H insertion. Consequently, these insertions enhance the electronic conductivity of the cathode material. Additionally, phase transitions are expected to occur at high Mg concentrations, while the insertion of H, even at high concentrations, does not affect long-range lattice distortion. These insights are crucial for understanding and optimizing the behavior of V_2O_5 as a cathode material in Mg-ion batteries.

4.5 References

De Jesus, L. R., Andrews, J. L., Parija, A., and Banerjee, S. (2018). Defining Diffusion Pathways in Intercalation Cathode Materials: Some Lessons from V_2O_5 on Directing Cation Traffic. *ACS Energy Letters, 3*(4), 915-931.

Hoover, W. G. (1985). Canonical dynamics: Equilibrium phase-space distributions. *Physical Review A, 31*(3), 1695-1697.

Karapidakis, E., and Vernardou, D. (2021). Progress on V_2O_5 Cathodes for Multivalent Aqueous Batteries. *Materials (Basel), 14*(9).

Liu, X., Euchner, H., Zarrabeitia, M., Gao, X., Elia, G. A., Groß, A., and Passerini, S. (2020). Operando pH Measurements Decipher H^+/Zn^{2+} Intercalation Chemistry in High-Performance Aqueous Zn/δ-V_2O_5 Batteries. *ACS Energy Letters, 5*(9), 2979-2986.

Nosé, S. (1984). A unified formulation of the constant temperature molecular dynamics methods. *The Journal of Chemical Physics, 81*(1), 511-519.

Pan, H., Shao, Y., Yan, P., Cheng, Y., Han, K. S., Nie, Z., Wang, C., Yang, J., Li, X., Bhattacharya, P., Mueller, K. T., and Liu, J. (2016). Reversible aqueous zinc/manganese oxide energy storage from conversion reactions. *Nature Energy, 1*(5).

Sai Gautam, G., Canepa, P., Abdellahi, A., Urban, A., Malik, R., and Ceder, G. (2015). The Intercalation Phase Diagram of Mg in V_2O_5 from First-Principles. *Chemistry of Materials, 27*(10), 3733-3742.

Suthirakun, S., Genest, A., and Rösch, N. (2018). Modeling Polaron-Coupled Li Cation Diffusion in V_2O_5 Cathode Material. *The Journal of Physical Chemistry C, 122*(1), 150-157.

Wan, F., Zhang, L., Dai, X., Wang, X., Niu, Z., and Chen, J. (2018). Aqueous rechargeable zinc/sodium vanadate batteries with enhanced performance from simultaneous insertion of dual carriers. *Nature Communications, 9*(1), 1656.

Wang, F., Fan, X., Gao, T., Sun, W., Ma, Z., Yang, C., Han, F., Xu, K., and Wang, C. (2017). High-Voltage Aqueous Magnesium Ion Batteries. *ACS Central Science, 3*(10), 1121-1128.

CHAPTER V

DIFFUSION KINETICS OF ION MIGRATION IN V_2O_5 CATHODE

During the discharge process, the presence of water in the electrolyte leading to H intercalate into the V_2O_5 cathode. This observation is supported by several studies (Dong et al., 2020; Kim et al., 2021; Zhou et al., 2021). To elucidate the kinetics of their diffusion, we conducted calculations to determine their respective diffusion barriers within a 1 × 3 × 3 V_2O_5 supercell. The results of these calculations can help us understand how the insertion of H affects the kinetic of Mg. Our research begins with a thorough examination of how H migrates within the α-V_2O_5 structure, discussed in section 5.1. The study of Mg migration is detailed in section 5.2. Finally, we explored the impact of H concentration in the V_2O_5 structure on Mg migration, which is discussed in section 5.3. This approach allows us to gain a understanding of how H and Mg move within the α-V_2O_5 system during the discharge process.

5.1 Kinetics of H Diffusion in V_2O_5 Cathode

Our initial focus was on understanding how H diffuses within the system. As discussed in the previous chapter, H tends to bind with O1, causing its electrons to localize at the V center. This localization results in the formation of a polaron within the VO_5 unit and the simultaneous creation of H^+ ions. To examine the details of H diffusion, we considered both H and polaron migration from one VO_5 unit to another along the [010] direction. This particular direction is known to be the preferred migration pathway not only for H but also for other ions in V_2O_5, as previously investigated (Ni et al., 2019).

To account for the movements of these system, we explored three distinct scenarios: (i) proton-coupled polaron transfer, (ii) proton diffusion preceding polaron transfer, and (iii) polaron transfer preceding proton diffusion. These scenarios, schematically depicted in Figure 5.1, provide us with a framework for understanding how H and polarons interact within the V_2O_5 structure.

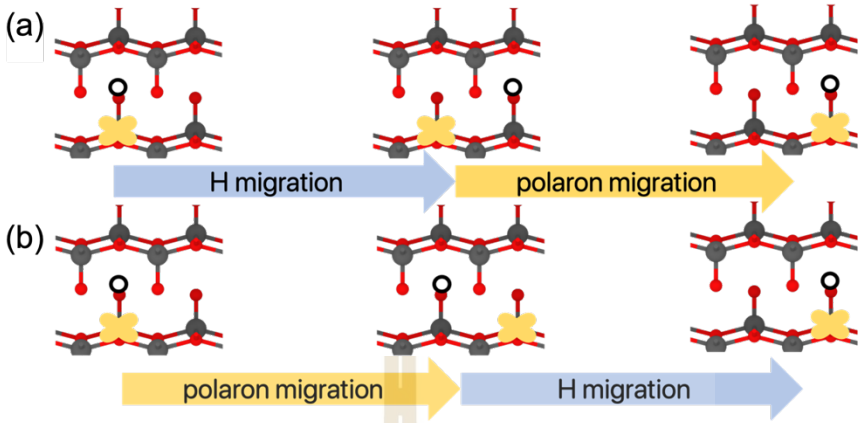

Figure 5.1 The Schematic of H and polaron separated migration configuration. (a) The proton diffusion preceding polaron transfer and (b) polaron transfer preceding proton diffusion. The white sphere represented H atom and yellow isosurface represented polaron localized.

As depicted in Figure 5.2, it is evident that all the considered scenarios exhibit comparable effective barriers, within the range of 0.5 to 0.6 eV. Notably, the first scenario, involving proton-coupled electron transfer (Figure 5.2(a)), appears to be the most favorable, with an energy barrier of 0.49 eV. In contrast, the other two scenarios, where H and the polaron undergo separate migrations, have slightly higher effective barriers. Specifically, scenario (ii) presents a barrier of 0.51 eV, while scenario (iii) has the highest barrier at 0.60 eV (Figure 5.2(b) and (c), respectively).

มหาวิทยาลัยเทคโนโลยีสุรนารี

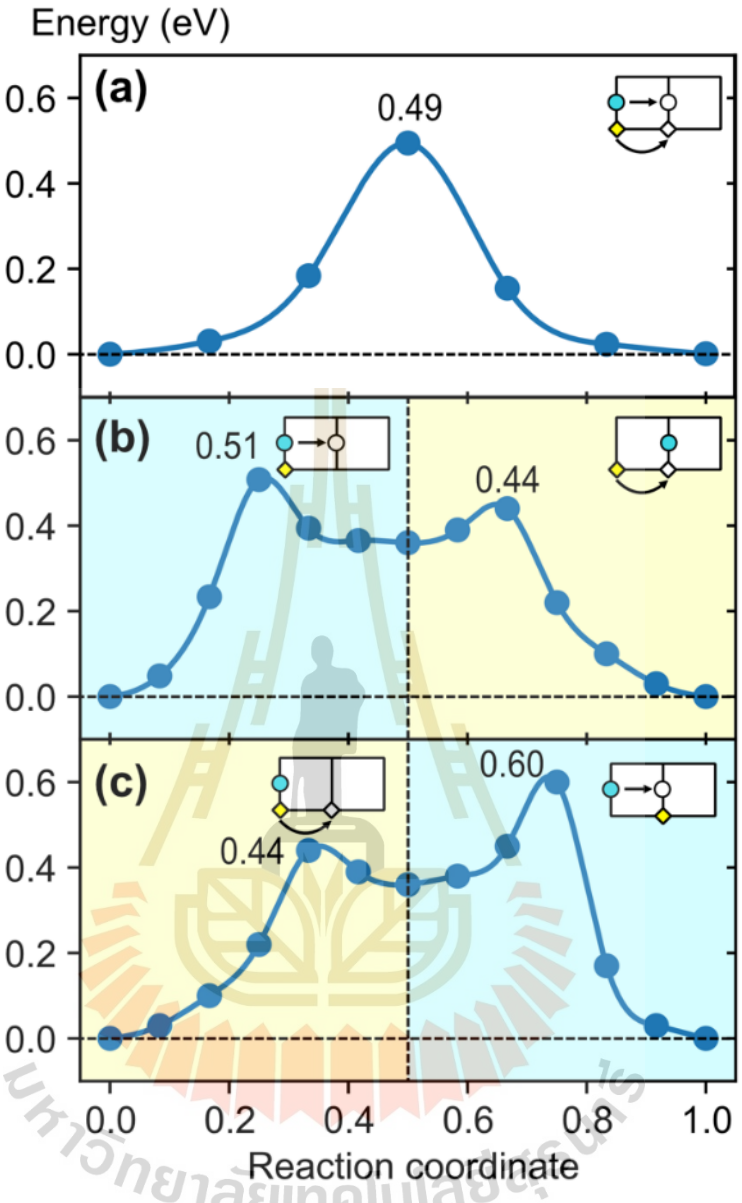

Figure 5.2 Energy profile of H and polaron migration in the α-V_2O_5 structure, involving three migration configurations: (a) H-coupled polaron transfer, (b) H Migration preceding polaron transfer, and (c) polaron transfer preceding H Migration. The insets schematically depict the sequence of migration events, where the α-V_2O_5 structure is represented by squares, H by cyan circles, and polarons by yellow diamonds.

These results suggest that H and its polaron tend to stay close to each other within the same VO_5 unit. As a result, scenarios where they move separately exhibit

less favorable dynamics, resulting in higher-energy configurations and less favorable outcomes. This behavior can be attributed to the Coulombic attraction between the ion and the electron, which penalizes their separation and leads to high energy barrier.

It's worth noting that these findings align with previous computational studies that have reported similar coupled movements of ions and polarons in materials like V_2O_5 (Suthirakun et al., 2018) and $LiFePO_4$ (Malik et al., 2013).

5.2 Kinetics of Mg Diffusion in V_2O_5 Cathode

Subsequently, our investigation shifted its focus to the migration of Mg within the V_2O_5 structure, along three distinct pathways labeled as P1, P2, and P3. These pathways correspond to the [010], [110] and [001] directions, as illustrated in Figure 5.3. Using the CI-NEB method, we gained insights into the energy barriers related to Mg migration within a 1x3x3 V_2O_5 supercell.

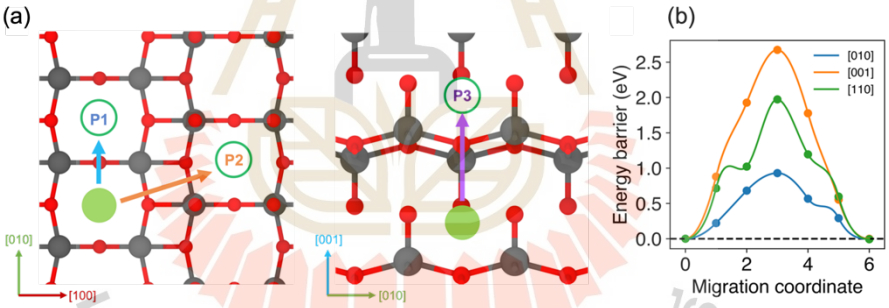

Figure 5.3 The possible Mg migration pathway in V_2O_5 structure. (a) P1, P2 and P3 represented the Mg migration pathway in [010], [110] and [001], respectively. (b) minimum energy pathway of Mg migration.

Our findings reveal that the energy barriers for Mg migration differ depending on the chosen migration pathway. Along the [010] direction, the energy barrier is measured at 0.93 eV, whereas the [110] direction presents a notably higher barrier of 1.98 eV. Meanwhile, the [001] direction exhibits the highest energy barrier, reaching 2.68 eV. These results highlight the directional sensitivity of Mg migration in V_2O_5, with the migration process being considerably more energetically favorable along the [010]

direction and requiring more energy for overcome the energy barrier along the [110] and [001] directions, respectively.

Our investigation further studies the diffusion of Mg within the V_2O_5 structure. Building upon the insights presented in chapter IV, where we established that an inserted Mg ionizes, yielding two polarons at the two VO_5 units, we conducted on a calculation of its diffusion behavior. Similar to the approach taken for H diffusion, we considered diffusion along the [010] direction due to its well-documented favorability (Xiao et al., 2018). We explored the migratory patterns of Mg and polarons in both coupled and separate manners, as represented in Figure 5.4. Our exploration contains four distinct scenarios: (i) Mg-coupled two polaron transfer, (ii) Mg diffusion preceding two polaron transfer (Figure 5.4(a)), (iii) One polaron transfer preceding Mg diffusion, followed by another polaron transfer (Figure 5.4(b)) and (iv) Two polaron transfer preceding Mg diffusion (Figure 5.4(c)).

มหาวิทยาลัยเทคโนโลยีสุรนารี

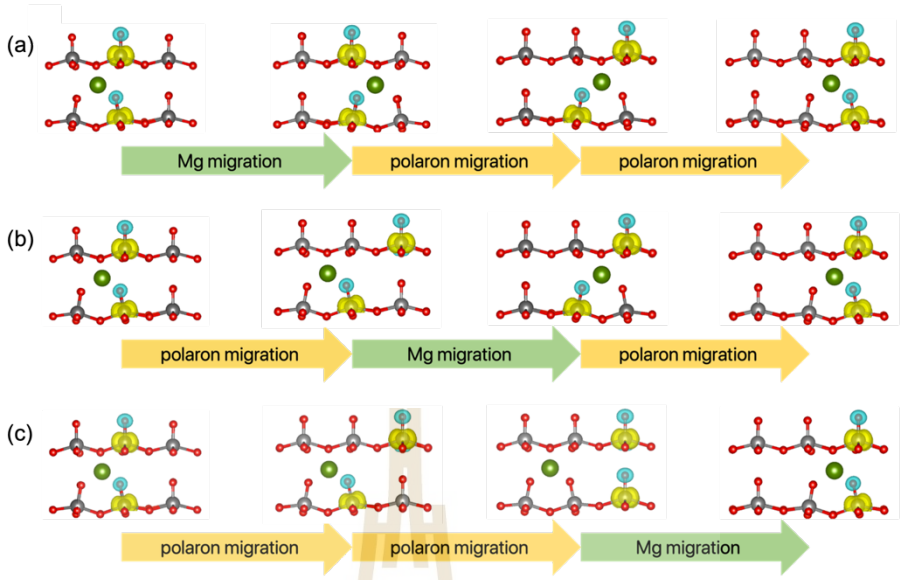

Figure 5.4 The ion and polaron migration configuration of one Mg and two polarons migration. (a) Mg diffusion preceding two polaron transfer, (b) one polaron transfer preceding Mg diffusion and (c) two polaron transfer preceding Mg diffusion. The red, green and grey sphere represented oxygen, magnesium and vanadium, respectively. The yellow isosurface at 0.032 e $Å^{-3}$ highlights the polaron localization.

Our findings suggest that the scenario involving the coupled transfer of Mg^{2+} ions and two polarons emerges as the most energetically favorable, characterized by an effective barrier of 0.93 eV (Figure 5.5(a)). This observation reviews the synergistic nature of Mg and polaron movement within the V_2O_5 structure, contributing to the overall understanding of their diffusion behavior.

In contrast to the coupled motion, the scenarios involving separate movements of ions and polarons, as depicted in Figure 5.5, leading to ion-polaron Coulombic interaction, resulting in slightly increased energy barriers spanning the range of 0.95 to 1.60 eV, as demonstrated in Figure 5.5(b), (c) and (d).

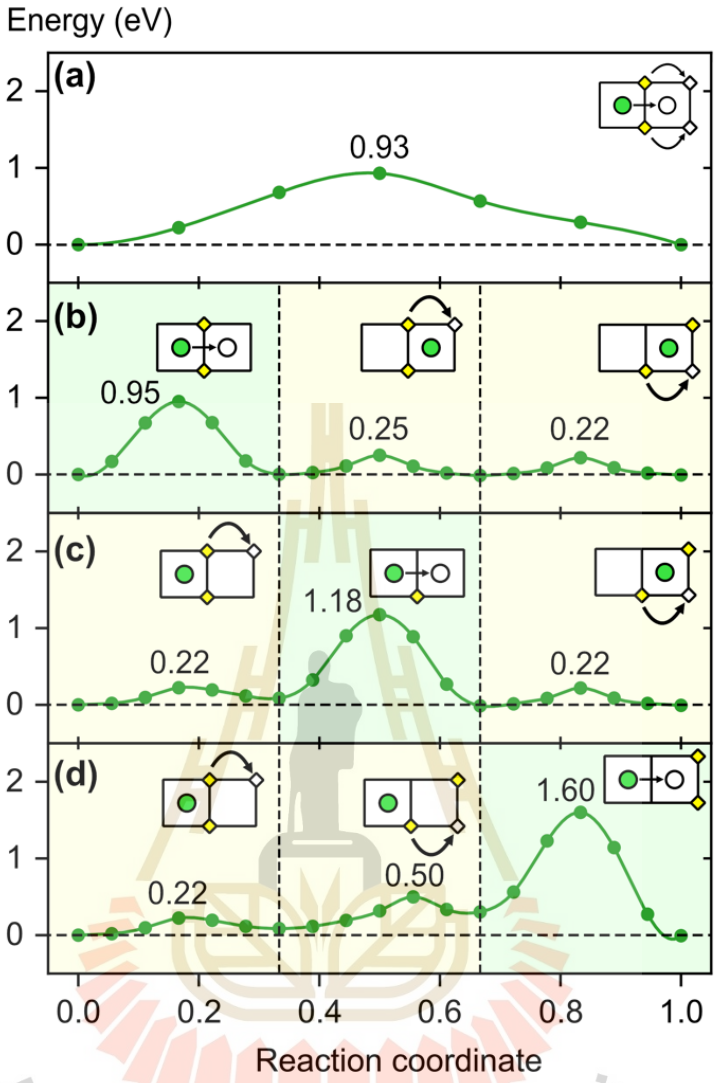

Figure 5.5 Energy Profile of Mg-Two-Polaron Migration: (a) Coupled Migration of Mg and Two Polarons, (b) Sequential Mg Migration Followed by Polaron Migration, (c) Mg Migration Following a Single Polaron Migration, and (d) Mg Migration After Two Polaron Migrations. The accompanying diagrams provide a visual depiction of the migration sequence, where squares denote the α-V_2O_5 structure, green circles represent Mg, and yellow diamonds depict polarons.

Specifically, Figure 5.5(b) illustrates that when the Mg ion migrates with two polarons, it exhibits only a higher barrier compared to the coupled motion scenario (0.95 eV vs. 0.93 eV). However, when the diffusion path lacks one or both polarons in close, the energy barrier of Mg ion's diffusion increases, leading to an energy barrier of

1.18 eV and 1.60 eV, respectively (Figure 5.5(c) and (d)). The difference in energy barrier heights can be attributed to the more significant Coulombic interaction by Mg^{2+} ions, which arises from their higher net charge when compared to H^+ ions. It's worth noting that our calculated energy barrier for the preferred diffusion scenario is lower than previously reported values of 1.28 eV (Ni et al., 2019) and 1.29 eV (Xiao et al., 2018). The origin of these differences remains unclear but is likely related to the absence of polaron configurations in previous computational studies.

In summary, our findings reveal a difference in the diffusion energy barriers between H and Mg, with effective energy barriers of 0.49 eV and 0.93 eV, respectively. These results imply that H diffusion occurs much more rapidly compared to Mg diffusion. As a result, it is plausible that in the early stages of the discharge process, H from dissociated water molecules within the electrolyte would intercalate into the V_2O_5 cathode material before the slower diffusion of Mg ions from the anode. This sequence of events suggests that the V_2O_5 structure may accumulate a substantial amount of H before Mg intercalation occurs. This deduction aligns well with observations from experimental studies involving aqueous electrolytes in V_2O_5-based cathodes for Zn-ion batteries (Dong et al., 2020; Liu et al., 2020). Furthermore, the stable insertion and rapid diffusion of H within the lattice have the potential to enhance the specific capacity of the cathode. Both the inserted H and its associated polarons can serve as charge carriers, contributing to improved electrochemical performance.

มหาวิทยาลัยเทคโนโลยีสุรนารี

5.3 Effect of H Insertion on Mg Diffusion Kinetics

As elucidated in the preceding section, the insertion of H from dissociated aqueous electrolytes into V_2O_5 occurs at a faster rate than Mg insertion, due to the low diffusion barriers associated with proton-coupled polaron transfer. Consequently, it is reasonable to anticipate the formation of H-inserted structures, denoted as $H_xV_2O_5$, prior to the intercalation of Mg during the discharge process. In light of this, our study focuses on how protonated structures affect the kinetic of Mg migration.

To assess this effect, we considered a scenario involving a high concentration of H, wherein all O1 atoms become protonated, thereby yielding the $H_2V_2O_5$ structure.

The diffusion path for Mg remains along the [010] direction. It is noteworthy that, in this analysis, we do not account for the migration of polarons, given the itinerant behavior of $H_2V_2O_5$, where additional electrons stemming from H are anticipated to delocalize throughout the lattice. This behavior has been previously observed in highly lithiated V_2O_5 (De Jesus et al., 2018).

As presented in Figure 5.6, when the H concentration is increased, the diffusion barrier for Mg decreases to 0.23 eV. This reduction in the energy barrier is substantial when compared to the diffusion barrier in the pristine structure, which is 0.93 eV. The decrease in the energy barrier can be attributed to the expansion of the diffusion channel along the [010] direction, a phenomenon discussed in chapter 4. Additional insights are derived from the transition state (TS) structures, which reveal that in the H-inserted system, the distances between Mg ions and their nearest oxygen atoms are 0.03 to 0.09 Å greater than those in the pristine system (Figure 5.6(b)). This observation highlights the structural modifications induced by the presence of H, which facilitate more effortless Mg diffusion within the lattice.

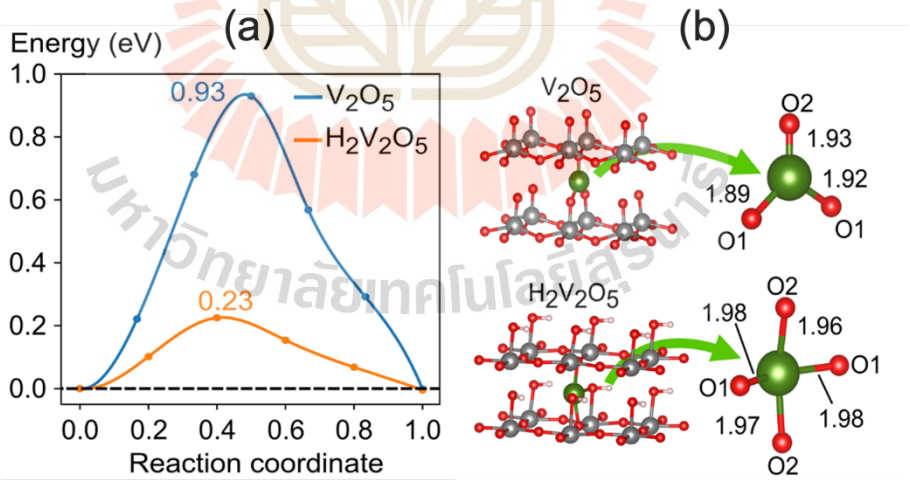

Figure 5.6 (a) Energy profiles for Mg diffusion along the [010] direction in V_2O_5 and $H_2V_2O_5$. (b) Transition state structures for Mg diffusion in the protonated variants with noticeable relaxation, resulting in longer Mg–O Distances. The annotated bond distances are presented in angstroms.

Furthermore, we have included a visual representation of the Mg-O distances throughout the Mg migration process in Figure 5.7. This illustration helps us better understand how the diffusion happens inside the V_2O_5 structure.

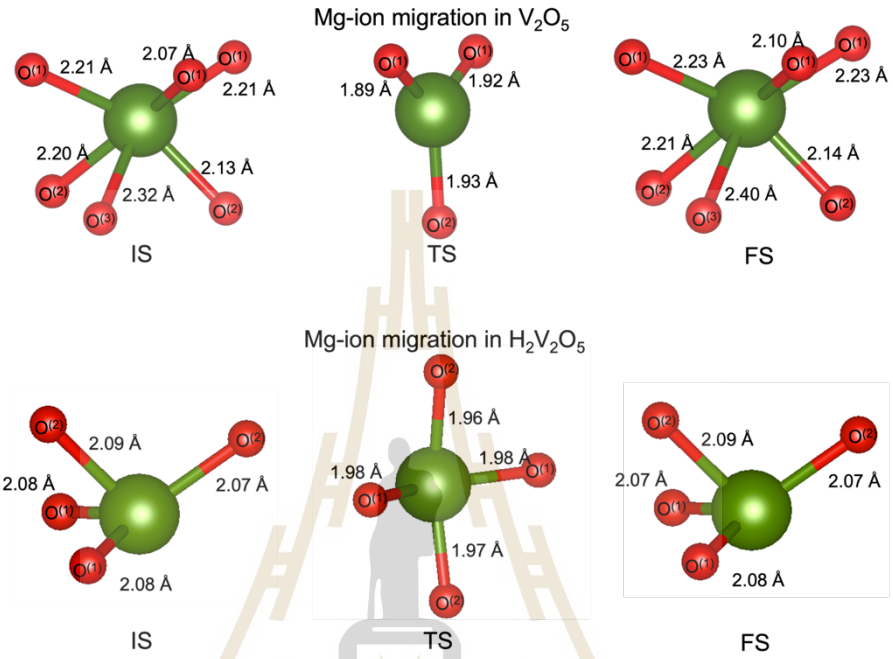

Figure 5.7 O-environmental atom during Mg migration in V_2O_5 and $H_2V_2O_5$. IS, TS and FS represent initial, transition and final state, respectively.

The relaxation structure observed in the TS structure leads to a more stable TS energy, resulting in a lower diffusion barrier and faster kinetics for Mg diffusion. This phenomenon underscores the significant role played by H insertion, as it induces structural changes that enhance Mg diffusion within the lattice. One notable effect is the reduction in the electronegative charge of O upon H insertion at O1, which leads to a larger O1–O1 distance and an expanded diffusion channel.

Our computational findings align with prior DFT studies (Ni et al., 2019) and experimental observations (Wang et al., 2017). Both of these sources suggest that H insertion can indeed improve the kinetics of Mg diffusion. Facilitating ion movement within the H-inserted structure holds the potential to mitigate capacity fading, a phenomenon often attributed to slow diffusion kinetics or trapped ions within the V_2O_5 structure (Huang et al., 2015; Lee et al., 2012; Yao et al., 2018).

5.4 Reference

De Jesus, L. R., Andrews, J. L., Parija, A., and Banerjee, S. (2018). Defining Diffusion Pathways in Intercalation Cathode Materials: Some Lessons from V_2O_5 on Directing Cation Traffic. *ACS Energy Letters, 3*(4), 915-931.

Dong, Y., Jia, M., Wang, Y., Xu, J., Liu, Y., Jiao, L., and Zhang, N. (2020). Long-Life Zinc/Vanadium Pentoxide Battery Enabled by a Concentrated Aqueous ZnSO4 Electrolyte with Proton and Zinc Ion Co-Intercalation. *ACS Applied Energy Materials, 3*(11), 11183-11192.

Huang, X., Rui, X., Hng, H. H., and Yan, Q. (2015). Vanadium Pentoxide-Based Cathode Materials for Lithium-Ion Batteries: Morphology Control, Carbon Hybridization, and Cation Doping. *Particle & Particle Systems Characterization, 32*(3), 276-294.

Kim, S., Shan, X., Abeykoon, M., Kwon, G., Olds, D., and Teng, X. (2021). High-Capacity Aqueous Storage in Vanadate Cathodes Promoted by the Zn-Ion and Proton Intercalation and Conversion-Intercalation of Vanadyl Ions. *ACS Applied Materials & Interfaces, 13*(22), 25993-26000.

Lee, J. W., Lim, S. Y., Jeong, H. M., Hwang, T. H., Kang, J. K., and Choi, J. W. (2012). Extremely stable cycling of ultra-thin V2O5 nanowire–graphene electrodes for lithium rechargeable battery cathodes. *Energy & Environmental Science, 5*(12).

Liu, X., Euchner, H., Zarrabeitia, M., Gao, X., Elia, G. A., Groß, A., and Passerini, S. (2020). Operando pH Measurements Decipher H^+/Zn^{2+} Intercalation Chemistry in High-Performance Aqueous Zn/δ-V_2O_5 Batteries. *ACS Energy Letters, 5*(9), 2979-2986.

Malik, R., Abdellahi, A., and Ceder, G. (2013). A Critical Review of the Li Insertion Mechanisms in LiFePO4Electrodes. *Journal of The Electrochemical Society, 160*(5), A3179-A3197.

Ni, D., Shi, J., Xiong, W., Zhong, S., Xu, B., and Ouyang, C. (2019). The effect of protons on the Mg^{2+} migration in an alpha-V_2O_5 cathode for magnesium batteries: a first-principles investigation. *Physical Chemistry Chemical Physics, 21*(14), 7406-7411.

Suthirakun, S., Genest, A., and Rösch, N. (2018). Modeling Polaron-Coupled Li Cation Diffusion in V_2O_5 Cathode Material. *The Journal of Physical Chemistry C, 122*(1), 150-157.

Wang, F., Fan, X., Gao, T., Sun, W., Ma, Z., Yang, C., Han, F., Xu, K., and Wang, C. (2017). High-Voltage Aqueous Magnesium Ion Batteries. *ACS Central Science, 3*(10), 1121-1128.

Xiao, R., Xie, J., Luo, T., Huang, L., Zhou, Y., Yu, D., Chen, C., and Liu, Y. (2018). Phase Transformation and Diffusion Kinetics of V2O5 Electrode in Rechargeable Li and Mg Batteries: A First-Principle Study. *The Journal of Physical Chemistry C, 122*(3), 1513-1521.

Yao, J., Li, Y., Massé, R. C., Uchaker, E., and Cao, G. (2018). Revitalized interest in vanadium pentoxide as cathode material for lithium-ion batteries and beyond. *Energy Storage Materials, 11*, 205-259.

Zhou, L., Liu, L., Hao, Z., Yan, Z., Yu, X.-F., Chu, P. K., Zhang, K., and Chen, J. (2021). Opportunities and challenges for aqueous metal-proton batteries. *Matter, 4*(4), 1252-1273.

มหาวิทยาลัยเทคโนโลยีสุรนารี

CHAPTER VI
EFFECT OF HYDROGEN INSERTION ON THE STRUCTURAL STABILITY

The crystal structure of V_2O_5 has four phases: α, ε, δ, and γ. Among these phases, α-V_2O_5 is widely employed as a cathode material in metal-ion batteries due to its promising theoretical capacity and stability (Liu et al., 2018). However, it has been observed that during discharge process with a high metal-ion concentration, the α-phase undergoes an irreversible transformation into other phases (Sai Gautam et al., 2015). Previous computational studies have shown that α-V_2O_5 can transform into the δ-V_2O_5 phase when the concentration of Li exceeds 0.75 ($Li_{0.75}V_2O_5$) (McColl et al., 2019; Xiao et al., 2018). This phase transformation is primarily driven by strong electrostatic interactions between the intercalated ions and the V_2O_5 host lattice. Unfortunately, these irreversible phase changes pose a significant challenge, leading to poor battery performance and reduced ion usage. (Liu et al., 2018; McNulty et al., 2014). The weakness of α-V_2O_5 to such transformations at high ion concentrations underscores the necessity for strategies to mitigate these adverse effects and enhance the long-term stability and performance of metal-ion batteries employing V_2O_5 cathodes. In this chapter, we explored the impact of H on the phase transformation of the V_2O_5 structure. Additionally, we investigated the discharge voltage profiles under varying H concentrations in the V_2O_5 structure during Mg insertion.

6.1 Influence of H Insertion on Structural Stability

In this study, we investigated how the insertion of H can help mitigate the phase transition from α-V_2O_5 to δ-V_2O_5 induced by Mg intercalation. To detect the α-δ phase transition, we employed a analytical approach, tracking changes in the puckering angle (θ) of the O1–O2–O1 and the layered angle (ϕ) formed by the V–V–V

layers as we increase the Mg concentration. The pristine α-phase has a puckering angle (θ) of 76° and a layered angle (ϕ) of 90°, while the δ-phase exhibits a puckering angle (θ) of 56° and a layered angle (ϕ) of 80°, as shown in Figure 6.1(a).

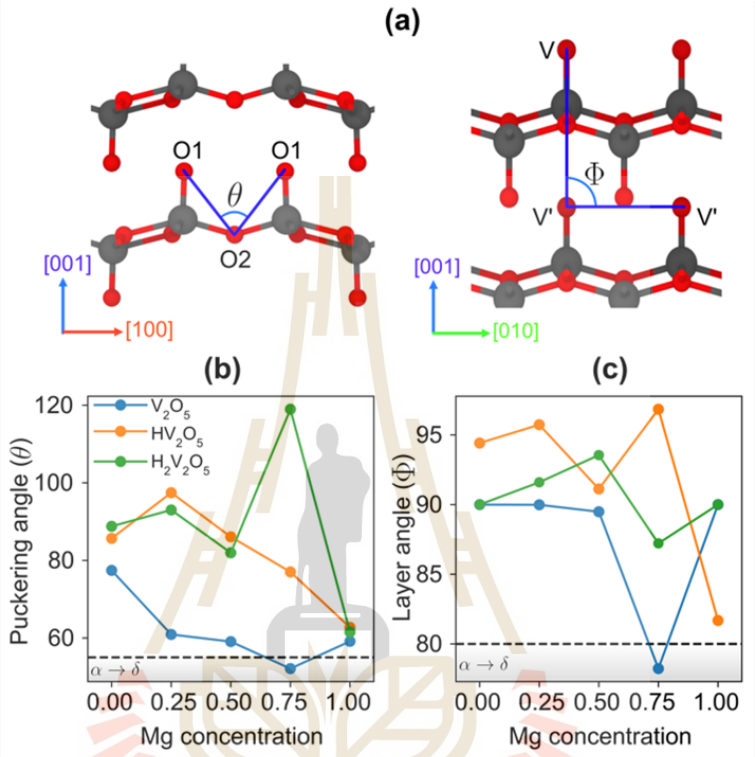

Figure 6.1 (a) Conceptual representation depicting the characterization of the α to δ phase transition through puckering and layered angles. The correlation between intercalated Mg concentrations and (b) puckering as well as (c) layered angles. The introduction of hydrogen prevents the α-δ phase transition.

As depicted in Figure 6.1(b) and (c), our observations indicate that the fully H-inserted structure, known as $H_2V_2O_5$, maintains puckering (62°) and layered angles (90°) that closely resemble those of pristine α-V2O5. This result suggests that H insertion effectively preserves the α-phase, even at high concentrations. The preservation of the α-phase, even under elevated Mg concentrations, holds great promise for improving battery performance and ion utilization in metal-ion battery systems.

With the increasing concentration of Mg, the puckering and layered angles within pristine V_2O_5 gradually deviate from the characteristic values of the α phase and approach those typical of the δ phase. The criteria threshold for this phase transition emerges at $Mg_{0.75}V_2O_5$, where the puckering angle reduces to under 52°, and the layered angle reduces to under 78°. These distortions induced by Mg insertion can be attributed to the strong electrostatic interactions between Mg^{2+} ions and the electronegative O lattice.

Notably, our findings are in agreement with previous computational studies involving V_2O_5-based cathodes used in Li-ion batteries, which have reported a transition from the α to ε phase at Li concentrations varying from 0.3 to 0.7 and to the δ phase at a Li concentration of 0.8 (Zhao et al., 2016). In the context of Mg-ion batteries, a similar transformation to the δ phase occurs at a Mg concentration of 0.75 (Xiao et al., 2018). Furthermore, experimental evidence supports these findings, indicating that lithiated V_2O_5 cathodes undergo an irreversible change to the ω phase at a Li concentration of 3.69.

Remarkably, the introduction of H into the structure proves to be an effective mechanism for mitigating the structural distortions caused by Mg insertion. As shown in Figure 6.1(b) and (c), the puckering and layered angles exhibit less pronounced changes as Mg concentrations increase within the H-inserted structures. These observations suggest that the H-inserted configurations are capable of maintaining their α phases across a wide range of Mg concentrations. This preservation can be attributed to the protonation of O1 atoms caused by H insertion, which weakens the electrostatic interactions between Mg ions and the lattice, thereby reducing structural distortion.

Supporting this explanation, we investigated the Bader charges associated with O1 atoms following protonation. The result reveals a decrease in the average charge transfer into O1 atoms, transitioning from 0.41 to 0.25 and 0.12 electrons when Mg is inserted into HV_2O_5 and $H_2V_2O_5$, respectively. In contrast, the average charge of Mg atoms undergoes a decrease, shifting from +1.72 to +1.69 and +1.68 electrons when inserted into pure V_2O_5, HVO, and $H_2V_2O_5$, respectively. These result suggest that H insertion within the V_2O_5 structure leads to a reduction in charge transfer from the

inserted Mg to the lattice, consequently weakening the interactions between Mg and the lattice.

6.2 The effect of H Insertion on the Discharge Voltage Profiles

Furthermore, our investigation extends to the examination of H insertion's impact on the discharge voltage profiles. This investigation involves the calculation of the open-circuit voltage (OCV) profile, a pivotal aspect of our analysis. The OCV profile is determined at various concentrations of both H and Mg within $H_xV_2O_5$, utilizing the following equation below (Van der Ven et al., 2020).

$$OCV(y) = \frac{E_{Mg_yH_xV_2O_5} - E_{H_xV_2O_5} - eE_{Mg}}{y2e} \quad (6.1)$$

The open-circuit voltage (OCV) profile was computed using the following equation (6.1), where $E_{Mg_yH_xV_2O_5}$ represents the total energy of the Mg-inserted $H_xV_2O_5$ structure, $E_{H_xV_2O_5}$ denotes the total energy of the $H_xV_2O_5$ structure, and E_{Mg} signifies the chemical potential of Mg atoms derived from the bulk Mg structure.

As depicted in Figure 6.2, the discharge voltage of V_2O_5 decreases from 2.69 to 2.52 V as the Mg concentration increases from 0.125 to 1. Subsequently, with the voltage increasing from 2.44 to 2.61 V as the Mg concentration advances from 0.50 to 0.75. These non-monotonic changes in discharge voltage within this concentration range can be attributed to the structural distortions that become more pronounced at high Mg concentrations, as shown in Figure 6.1(b) and (c).

มหาวิทยาลัยเทคโนโลยีสุรนารี

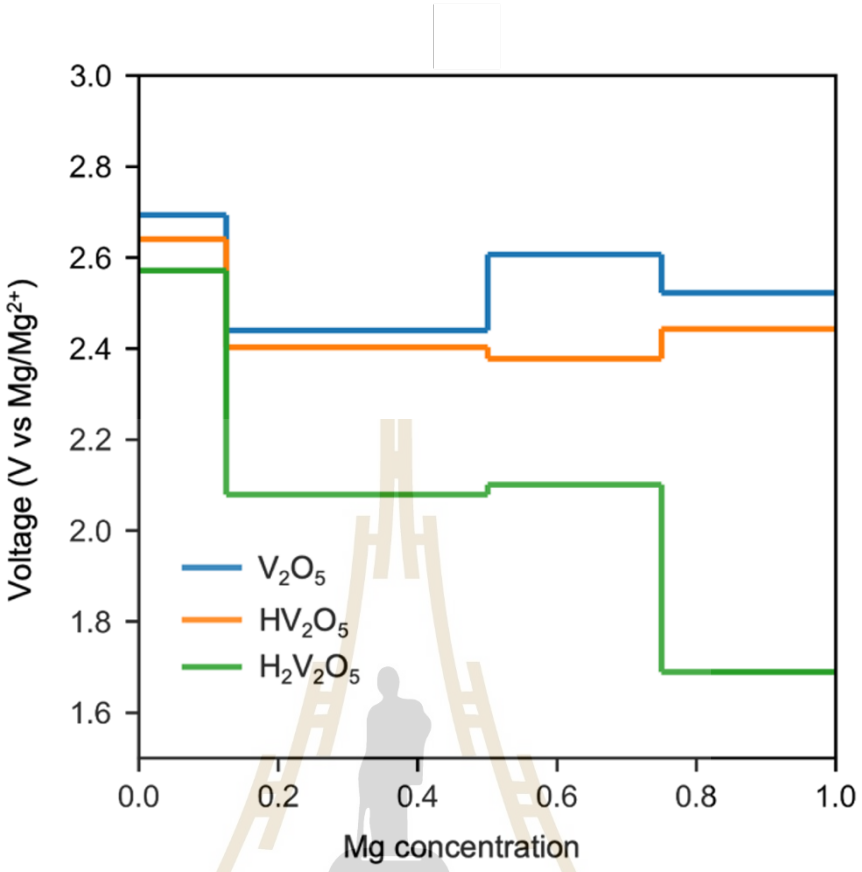

Figure 6.2 Voltage profile of $H_xV_2O_5$ during Mg insertion. The blue, orange and green line represented the voltage profile of $H_xV_2O_5$-based cathode where x=0, 1 and 2, respectively.

The introduction of H atoms leads to a decrease in the initial voltage. Specifically, the OCV of $H_xV_2O_5$, with H concentrations of 0, 1, and 2, exhibits a reduction from 2.69 V to 2.64 V and further down to 2.57 V, respectively. This observation highlights the role of H atoms in reducing the interactions between Mg ions and the α-V_2O_5 lattice. The mechanism behind this reduction can be attributed to the screening effect induced by the protonation of O1 atoms.

Our computed OCV values at a low Mg concentration ($Mg_{0.125}V_2O_5$) align favorably with those reported in other DFT studies, falling within the range of 2.34 to 2.70 V, as summarized in Table 6.1. Furthermore, our calculated OCV values for V_2O_5 (2.52 V) and $H_2V_2O_5$ (1.69 V) are consistent with previous DFT reports, which reported

OCV values of 2.30 V for V_2O_5 and 1.70 V for $H_2V_2O_5$ (Ni et al., 2019). These agreements support the reliability of our computational findings and emphasize their relevance in the context of metal-ion battery systems.

Table 6.1 Compared OCV value of low Mg concentration in V_2O_5-based cathode.

functional	U-J parameter on V center	vdW corection	concentration	voltage	References
PBE	3.5	optPBE-vdW	$Mg_{0.125}V_2O_5$	2.69	This work
PBE	-	D3	$Mg_{0.125}V_2O_5$	2.34	(Zhao et al., 2016)
PBE	3.1	-	$Mg_{0.080}V_2O_5$	2.44	(Sai Gautam et al., 2015)
PBE	4	optPBE-vdW	$Mg_{0.056}V_2O_5$	2.70	(Carrasco, 2014)

In summary, our study has presented evidence that H insertion significantly contributes to the structural stability of V_2O_5 during the process of Mg intercalation. This aligns with experimental data showing extended cycle life and increased capacity when using aqueous electrolytes. (Dong et al., 2020; Liang et al., 2017; Sa et al., 2016). It is hypothesized that the introduction of H serves as a preventive measure against the α-δ phase transition by reducing the electrostatic interactions between Mg ions and the lattice O. This, in turn, contributes to the improved cycling performance of the cathode, as it helps maintain the α phase, where the formation of additional irreversible phases is less likely to occur.

However, it is worth noting that the δ phase has been reported to potentially enhance ion transport kinetics by reducing diffusion barriers (Sai Gautam et al., 2015). Nevertheless, these advantageous effects must be considered alongside the potential for the emergence of other irreversible phases, especially at high Mg concentrations.

The balance between enhanced ion transport and the risk of unfavorable phase transitions highlights the interplay of factors that impact the performance and stability of V_2O_5-based cathodes in metal-ion battery systems.

6.3 Reference

Carrasco, J. (2014). Role of van der Waals Forces in Thermodynamics and Kinetics of Layered Transition Metal Oxide Electrodes: Alkali and Alkaline-Earth Ion Insertion into V_2O_5. *The Journal of Physical Chemistry C, 118*(34), 19599-19607.

Dong, Y., Jia, M., Wang, Y., Xu, J., Liu, Y., Jiao, L., and Zhang, N. (2020). Long-Life Zinc/Vanadium Pentoxide Battery Enabled by a Concentrated Aqueous $ZnSO_4$ Electrolyte with Proton and Zinc Ion Co-Intercalation. *ACS Applied Energy Materials, 3*(11), 11183-11192.

Liang, Y., Jing, Y., Gheytani, S., Lee, K. Y., Liu, P., Facchetti, A., and Yao, Y. (2017). Universal quinone electrodes for long cycle life aqueous rechargeable batteries. *Nature Mater, 16*(8), 841-848.

Liu, X., Zeng, J., Yang, H., Zhou, K., and Pan, D. (2018). V_2O_5-Based nanomaterials: synthesis and their applications. *RSC Advances, 8*(8), 4014-4031.

McColl, K., and Cora, F. (2019). Phase stability of intercalated V_2O_5 battery cathodes elucidated through the Goldschmidt tolerance factor. *Physical Chemistry Chemical Physics, 21*(15), 7732-7744.

McNulty, D., Buckley, D. N., and O'Dwyer, C. (2014). Synthesis and electrochemical properties of vanadium oxide materials and structures as Li-ion battery positive electrodes. *Journal of Power Sources, 267*, 831-873.

Ni, D., Shi, J., Xiong, W., Zhong, S., Xu, B., and Ouyang, C. (2019). The effect of protons on the Mg^{2+} migration in an alpha-V_2O_5 cathode for magnesium batteries: a first-principles investigation. *Physical Chemistry Chemical Physics, 21*(14), 7406-7411.

Sa, N., Wang, H., Proffit, D. L., Lipson, A. L., Key, B., Liu, M., Feng, Z., Fister, T. T., Ren, Y., Sun, C.-J., Vaughey, J. T., Fenter, P. A., Persson, K. A., and Burrell, A. K. (2016). Is alpha-V_2O_5 a cathode material for Mg insertion batteries? *Journal of Power Sources, 323*, 44-50.

Sai Gautam, G., Canepa, P., Abdellahi, A., Urban, A., Malik, R., and Ceder, G. (2015). The Intercalation Phase Diagram of Mg in V_2O_5 from First-Principles. *Chemistry of Materials, 27*(10), 3733-3742.

Van der Ven, A., Deng, Z., Banerjee, S., and Ong, S. P. (2020). Rechargeable Alkali-Ion Battery Materials: Theory and Computation. *Chemical Reviews, 120*(14), 6977-7019.

Xiao, R., Xie, J., Luo, T., Huang, L., Zhou, Y., Yu, D., Chen, C., and Liu, Y. (2018). Phase Transformation and Diffusion Kinetics of V_2O_5 Electrode in Rechargeable Li and Mg Batteries: A First-Principle Study. *The Journal of Physical Chemistry C, 122*(3), 1513-1521.

Zhao, X., Zhang, X., Wu, D., Zhang, H., Ding, F., and Zhou, Z. (2016). Ab initio investigations on bulk and monolayer V_2O_5 as cathode materials for Li-, Na-, K- and Mg-ion batteries. *Journal of Materials Chemistry A, 4*(42), 16606-16611.

มหาวิทยาลัยเทคโนโลยีสุรนารี

CHAPTER VII

CONCLUSIONS

Previous experimental studies suggest that, in the presence of an aqueous electrolyte, water molecules may dissociate at the electrolyte-electrode interface, providing H ions that can intercalate into the V_2O_5 cathode. The incorporation of H ions has been found to enhance the electrochemical performance of the V_2O_5 cathode. In this thesis, we employed density functional theory to investigate the effects of H insertion on the electronic conductivity, ion transport kinetics, and structural stability of the V_2O_5 cathode in Mg-ion batteries. Our computational analysis reveals that the inserted H tends to bind with vanadyl oxygen and donates an extra electron localized at the V center, resulting in the formation of a small polaron. As the H concentration increases, the extra electrons occupy several V centers, leading to occupied states at the top of the valence band and a reduction in the band gap. This enhances the electronic conductivity of the V_2O_5 cathode and accounts for improved charge carriers, thereby potentially increasing the specific capacity of the cathode. Similar electronic structures are observed when Mg ions are inserted, and higher Mg concentrations correspond to smaller band gaps. However, a high content of Mg leads to long-range structural distortion due to strong ion-lattice interaction, which can trigger a phase transition from the α to δ phase. This phase change is undesirable as it can cause irreversible phase transformation, leading to poor cyclability and capacity fading. To address these challenges, the addition of a small amount of water is found to promote Mg diffusion and suppress the phase transition. During the discharge process, dissociated H ions from the aqueous electrolyte can intercalate into the cathode, and the effective barriers of ion-coupled polaron transfer for H and Mg are determined to be 0.49 and 0.93 eV, respectively. This suggests that H can diffuse much faster than Mg in the V_2O_5 cathode. As a result, the cathode is expected to contain a high H content before Mg intercalation, reducing the Mg diffusion barrier from 0.93 to 0.23 eV. The pre-inserted H thus accelerates ion diffusion kinetics and inhibits the α to δ phase

transition upon Mg intercalation. This effect is attributed to the reduction in electrostatic interaction between Mg ions and the lattice, as the vanadyl oxygen becomes less electronegative when it is protonated. Our study not only investigated the effect of H concentration on electronic and kinetic properties but also considered the influence of polaron configuration and structural stability, providing an atomistic understanding of the migration behavior in $H_xV_2O_5$-based cathodes for Mg-ion batteries. While our study focused on first-principles computations, our results align with previous experimental findings on $H_xV_2O_5$ cathodes, suggesting improved electronic conductivity and electrochemical performance. Our insights provide guidance for future experimental investigations, and these findings could be used to rationally design strategies to enhance the electrochemical performance of the V_2O_5 cathode in Mg-ion batteries.

มหาวิทยาลัยเทคโนโลยีสุรนารี

APPENDIX

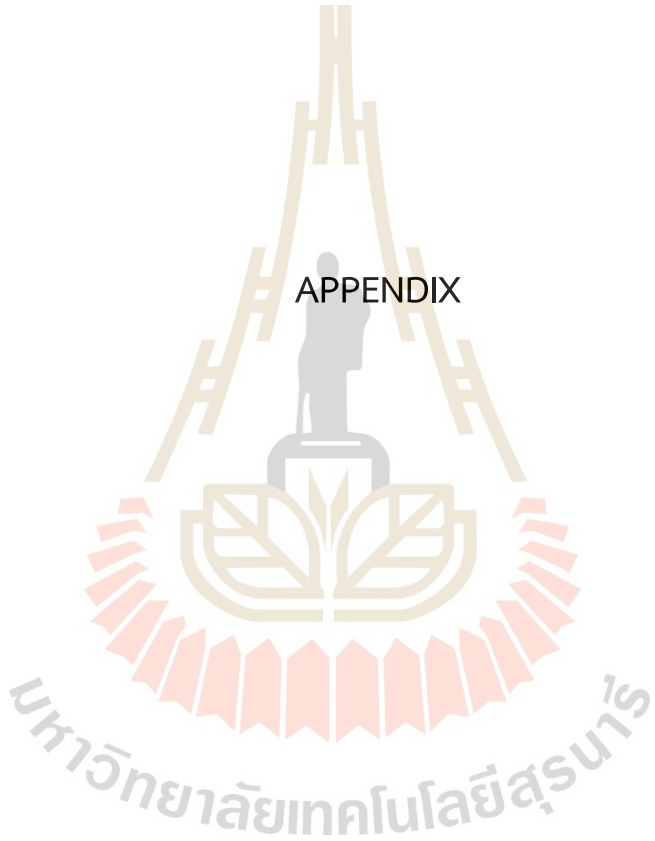

APPENDIX

PUBLICATION AND PRESENTATIONS

A.1 List of publication

- Untarabut, P., Singsen, S., Ngamwongwan, L., Fongkaew, I., Junkaew, A., and Suthirakun, S. (2023). Unraveling the Role of Hydrogen Insertion in Enhancing the Electrochemical Performance of the V_2O_5 Cathode for Mg-Ion Batteries: A First-Principles Study. *ACS Applied Energy Materials, 6*(17), 8666-8676.
- Sunkhunthod, C., Jiamprasertboon, A., Waehayee, A., Untarabut, P., Phonsuksawang, P., Butburee, T., Suthirakun, S., and Siritanon, T. (2023). Enhanced tetracycline photocatalytic degradation of FeO_x/Fe-$Bi_2O_2CO_3$ synthesized by one-step hydrothermal method. *Journal of Alloys and Compounds, 960,* 170632

A.2 List of presentations

Untarabut, P., Singsen, S., Fongkaew, I., Junkaew, A., and Suthirakun, S. (June 2022). On the origin of high performance V_2O_5 cathodes of aqueous Mgion batteries: A computational study. **The Siam Physics Congress 2022 (SPC2022).** Khao Yai Conventional Center (KTCC), Nakhon Ratchasima, Thailand. (Oral presentation)

Manuscript published in The Journal of ACS Applied Energy Materials

(journal impact factor = 6.959)

ACS APPLIED ENERGY MATERIALS

www.acsaem.org Article

Unraveling the Role of Hydrogen Insertion in Enhancing the Electrochemical Performance of the V_2O_5 Cathode for Mg-Ion Batteries: A First-Principles Study

Panupol Untarabut, Sirisak Singsen, Lappawat Ngamwongwan, Ittipon Fongkaew, Anchalee Junkaew,* and Suwit Suthirakun*

Cite This: https://doi.org/10.1021/acsaem.3c00830 Read Online

ACCESS | Metrics & More | Article Recommendations | Supporting Information

ABSTRACT: Vanadium pentoxide, V_2O_5, is a promising candidate for Mg-ion batteries owing to its high theoretical capacity. But sluggish electron−ion conductivity and capacity fading limit its commercialization. Adding a small amount of water into the electrolyte greatly enhances the charge transport kinetics and increases the capacity of the V_2O_5 cathode. It is suggested that water could dissociate and provide H that could be inserted into the cathode, but the role of H insertion remains unclear. In this work, we carried out first-principles computations to explore the effect of H insertion on the electronic conductivity, Mg diffusion kinetics, and structural stability upon Mg intercalation. We find that H insertion at high concentrations greatly reduces the band gap and increases the electronic conductivity of the material. The inserted H could act as a charge carrier, which enhances the capacity of the cathode. The transport kinetics of H is much faster than that of Mg. It is expected that during discharge, the cathode contains a high content of H before Mg intercalation. The preinserted H structure hastens the Mg diffusion by lowering the diffusion barrier of Mg from 0.93 to 0.23 eV. In addition, the fully protonated V_2O_5 cathode greatly suppresses irreversible α to δ phase transition which is considered the main cause of capacity fading. The enhanced ion transport kinetics and suppression of phase transformation stem from the weakened electrostatic interaction between the Mg ion and the lattice oxygen upon the H insertion. These findings could be used to rationally design the strategy to improve the electrochemical performance of the V_2O_5 cathode of Mg-ion batteries.

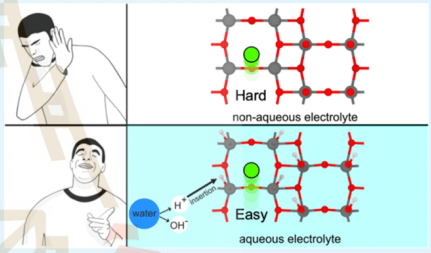

KEYWORDS: *aqueous electrolyte, V_2O_5, first-principles calculations, Mg-ion batteries, H insertion*

1. INTRODUCTION

Mg-ion batteries are proposed as an alternative substitution to partially replace conventional Li-ion cells[1,2] owing to their superior specific (∼2000 mAh/g) and volumetric capacity (∼3800 mAh/mL)[3] with better safety[4,5] and abundance of Mg sources.[6,7] However, divalent Mg^{2+} ions interact too strongly with the host cathode leading to slow charge transport kinetics and low ion utilization.[8] Suitable cathode materials with moderate interaction with Mg ions are needed in order to improve the batteries' performances.

Vanadium pentoxide, V_2O_5, has been proposed as a promising cathode material for several metal-ion batteries, including Mg.[9−14] The V_2O_5 cathode can effectively accommodate Mg ions to form $Mg_xV_2O_5$.[15] Its specific capacity is up to 427 mAh g^{-1} with a Coulombic efficiency of 82% after 2000 cycles and high reversibility.[16] Despite several benefits, its critical problems are the sluggish diffusion kinetics of Mg and capacity fading due to irreversible phase transformation at high Mg contents.[12,17] First-principles studies suggest that the migration barrier of Mg (1.26 eV) is much higher than that of Li (0.35−0.37 eV) in α-V_2O_5.[9,18] Hence, the performance of the V_2O_5-based cathode still needs some improvement.

The addition of aqueous electrolytes is one of the effective strategies that has been applied to enhance the electrochemical properties of the V_2O_5 cathode. Adding a small amount of water stabilizes and increases the capacity of the V_2O_5 cathode.[19−25] Several efforts, both experimentally and computationally, have been made to understand the role of water additives in the electrolyte. It was proposed that water

Received: March 30, 2023
Accepted: August 14, 2023

Downloaded via SURANAREE UNIV OF TECHNOLOGY on August 29, 2023 at 09:03:46 (UTC).
See https://pubs.acs.org/sharingguidelines for options on how to legitimately share published articles.

ACS Publications © XXXX American Chemical Society

https://doi.org/10.1021/acsaem.3c00830
ACS Appl. Energy Mater. XXXX, XXX, XXX−XXX

Manuscript published in The Journal of ACS Applied Energy Materials

(journal impact factor = 6.959)

could be inserted into the lattice that stabilizes the layered V_2O_5 structure by forming a water pillar.[26]

One recent explanation tells that water could dissociate at the electrode/electrolyte interface and yield H^+ and electrons.[27−30] For example, in the case of Zn-ion batteries, the dissociated H^+ and its electron could diffuse into the V_2O_5 structure and protonate lattice O to form $H_xV_2O_5$, which, in turn, improves the capacity of the cathode where H is account for a charge carrier.[20,25] Specifically, the $H_xV_2O_5$ retains its capacity of 425 mAh g^{-1} (91.3%) at 5000 cycles.[25] In addition, for Mg-ion batteries, proton intercalation from an aqueous electrolyte emerges as a promising strategy to enhance the performance of V_2O_5 cathodes. Yanan Xu and co-workers demonstrated the potential of a bilayer-structured vanadium oxide with Mg^{2+} ions and lattice water, showcasing excellent rate performance and an unprecedented cycling life with 80.0% capacity retention after 10,000 cycles.[26] Niya Sa and co-workers further highlighted the compatibility of Mg anodes with V_2O_5 cathodes in low-water-level electrolytes, leading to the reversible Mg deposition and direct evidence of reversible Mg intercalation.[30] These collective findings underscore the importance of proton intercalation and appropriate electrolyte design in optimizing V_2O_5 cathodes for Mg-ion batteries, providing promising prospects for high-energy-density battery applications. Other experiments also support this explanation that electrolyte becomes basic after discharge due to water dissociation and loss of H^+ and electron upon insertion into the cathode as using the operando pH determination method revealing that both H^+ and metal ions intercalate into V_2O_5.[22] A recent computational study reveals that H insertion could improve Mg intercalation by reducing the ion diffusion barriers.[27]

Besides the experimental and computational efforts cited above, the role of H insertion in the structural stability of the V_2O_5 cathode remains unexplored. Hence, we aim to use first-principles tools to systematically study the role of H insertion on the improved electrochemical properties of the V_2O_5 cathode, including the enhanced electronic conductivity, ion transport kinetics, and structural stability. In particular, we discuss its effect on the electronic structures and the enhanced electronic conductivity of the materials. By calculating Mg diffusion barriers considering both ion and polaron transport, we propose that H insertion improves Mg-ion diffusion kinetics. In addition, systematic structural analysis shows that H insertion could prevent the formation of irreversible phases at high Mg contents. The insight obtained from this work can be used to further design strategies to improve the performances of Mg-ion batteries.

2. COMPUTATIONAL DETAILS

All calculations were performed using spin-polarized density functional theory (DFT) as implemented in the Vienna Ab initio Simulation Package (VASP 5).[31] The projector augmented wave method[32] was used to treat the core electrons and ion interactions where the valence electrons were expanded in the plane-wave basis: H 1s, Mg 2s, O 2s2p, and V 3p3d4s, with the kinetic energy cutoff of 500 eV. The generalized gradient approximation (GGA) with the Perdew−Burke−Ernzerhof (PBE) approach was used as the exchange−correlation functional term. The effective Hubbard U value of 3.5 eV was applied for V 3d to partially correct self-interaction errors.[33,34] We used the optPBE-vdW method to correct for the van der Waals interaction between the V_2O_5 layers.[35−37]

Insertion of ions was carried out using the $1 \times 2 \times 2$ V_2O_5 supercell. The Brillouin zone was sampled using the Monkhorst−Pack grid[38] of $4 \times 4 \times 4$ k-points for structural optimization and $12 \times 12 \times 12$ k-points for the electronic density of states (DOS) calculations. The Gaussian smearing method with a smearing width of 0.05 eV was used. The convergence criteria for the self-consistent field and for the force on each atom were set to 10^{-6} eV and 0.02 eV/Å, respectively.

To explore the behavior of Mg and H diffusion, we used a larger $1 \times 3 \times 3$ supercell with the k-points of $4 \times 4 \times 4$ for Brillouin zone sampling. The climbing image nudged elastic band (CI-NEB) method[39] was used to find the diffusion paths and barriers. Relative charges on each atom were determined using Bader charge analyses.[40]

3. RESULTS AND DISCUSSION

3.1. Structural and Electronic Properties of V_2O_5. We used the α-V_2O_5 phase (the orthorhombic with the *Pmmn* space group) as a model. It is one of the most stable phases under operating conditions of metal-ion batteries.[41] Its layered structure possesses a series of VO_5-distorted square pyramids connected via edge- and corner-sharing to form a two-dimensional (2D) layered structure in the *ab* plane, as shown in Figure 1a. Stacking these 2D layers in the normal direction

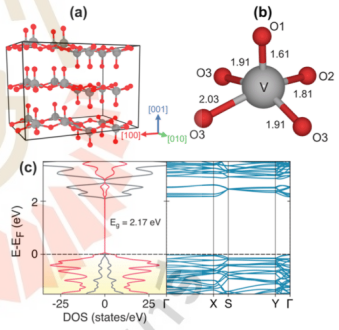

Figure 1. Sketches of (a) $1 \times 2 \times 2$ α-V_2O_5 supercell comprises a series of (b) VO_5 units with three inequivalent oxygen atoms, namely, vanadyl oxygen (O1), bridging oxygen (O2), and edge-sharing oxygen (O3). The labeled numbers are their bond distances in angstrom. (c) Its projected density of states shows a nonmagnetic semiconducting character with an indirect band gap of 2.17 eV. The red and gray solid lines represent the states of oxygen and vanadium, respectively.

yields a three-dimensional framework of α-V_2O_5 where each layer is held together by a weak van der Waals interaction. Such a layered structure can effectively accommodate small cations such as Li,[10,42,43] Na,[44,45] and Mg,[11,46,47] leading to high theoretical capacity when used as a cathode of metal-ion batteries.

Each VO_5 unit comprises three inequivalent O atoms including one vanadyl oxygen atom, O1, with the calculated V−O1 bond distance (d_{V-O1}) of 1.61 Å, one bridging oxygen atom, O2 (d_{V-O2} = 1.81 Å), and two edge-sharing oxygen atoms, O3 (d_{V-O3} = 1.91 Å, 2.03 Å), as shown in Figure 1b. The calculated bond distances are in good agreement with both experimental[48] and other DFT-reported[27,49,50] values

https://doi.org/10.1021/acsaem.3c00830
ACS Appl. Energy Mater. XXXX, XXX, XXX−XXX

Manuscript published in The Journal of ACS Applied Energy Materials

(journal impact factor = 6.959)

with maximum errors of 1.68 and 1.90%, respectively, as summarized in Table 1.

Table 1. Lattice Parameters and V−O Bond Distances in Angstroms of α-V_2O_5 as Obtained from Experimental Characterizations and Computations

α-V_2O_5	our work	computations (PBE + U)[27]	Exp.[48]
a	11.60	11.64	11.69
b	7.27	7.15	7.26
c	4.48	4.43	4.42
V−O1	1.61	1.61	1.58
V−O2	1.81	1.80	1.78
V−O3	1.95	1.95	1.93

Next, we explore the electronic structure of α-V_2O_5 by analyzing the density of states (DOS), as shown in Figure 1c. Our computations reveal that α-V_2O_5 exhibits semiconducting character with a calculated indirect band gap of 2.17 eV, which is consistent with those of the previous DFT+U studies and experimental value, as summarized in Table 2. The calculated

Table 2. Calculated Band Gaps of α-V_2O_5 Using Different Methods

method	E_g (eV)	references
DFT + U (U = 3.5)	2.17	this work
DFT + U (U = 4.0)	2.17	18
DFT + U (U = 2.0)	1.66	27
DFT + U (U = 3.5)	2.18	34
DFT + U (U = 4.0)	2.26	53
hybrid functional (PBE0)	4.04	54
GW approximation	2.3	55
GW approximation	2.89	56
experiment	2.3	48

projected density of states (PDOS) shows a nonmagnetic character with the equivalent number of states of both spin components as shown in Figure 1c. Its valence band is predominated by the O 2p states with some hybridization of the V 3d states, while it is vice versa for the conduction band. The unique character of the split conduction band stems from the deviation of octahedral symmetry of VO_5 units.[51,52]

It is noteworthy that the robust quasiparticle GW approximation and hybrid functional could provide more accurate electronic structures and band gap predictions for several semiconducting materials. Nevertheless, for V_2O_5 as summarized in Table 2, only the GW method could reproduce the experimental band gap, while the hybrid functional significantly overestimates the band gap.

3.2. Insertion of H and Mg. It has been experimentally reported that using aqueous-containing electrolytes could increase the capacity of the Mg-ion batteries.[17,23,57] During the discharge process, water molecules in the electrolyte can dissociate to generate H^+ and OH^-. The H^+ and also Mg ions can then intercalate into the V_2O_5 structure leading to the increased capacity of the cathode,[20,58,59] while the dissociated OH^- remains in the electrolyte as evidenced by the increase in pH upon discharging.[22] Herein, to better understand the effects of H and Mg intercalation on the structural and electronic properties of the V_2O_5 cathode, we inserted these ions into the 1 × 2 × 2 V_2O_5 supercell (Figure 1a) and analyzed the local structure and density of states as a function of ion concentrations. In addition, we calculated the insertion energies, E_{ins}, to determine its stability using the following equation,

$$E_{ins}^{H,Mg} = E_{(H,Mg)V16O40} - E_{V16O40} - \mu_{H,Mg} \quad (1)$$

where E_{V16O40} and $E_{(H,Mg)V16O40}$ are the total energies of the V_2O_5 supercell in the presence and absence of an intercalated H or Mg atom, respectively. $\mu_{H,Mg}$ is the chemical potential of the H or Mg atom taken from their most stable forms, i.e., an isolated H_2 molecule and Mg bulk, respectively.

First, we explore the behavior of H insertion. As shown in Figure 2, we find that H prefers to bind with the vanadyl

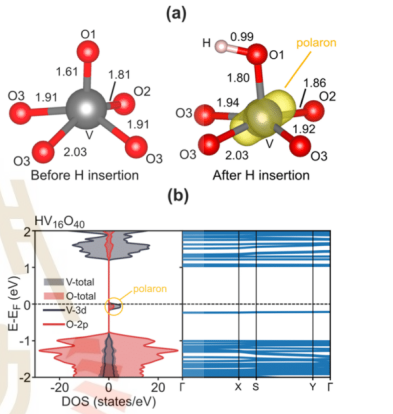

Figure 2. Schematic illustration of the effect of H insertion on (a) slight distortion of a VO_5 unit with electron localization at the V center (yellow isosurface of 0.032 e $Å^{-3}$) known as a small polaron. All of the VO_5 units in the pristine V_2O_5 lattice are identical. The labeled numbers are their bond distances in angstrom. The polaron formation appears as (b) a gap state in the projected density of states and band structure.

oxygen O1 atom with an O−H bond distance of 0.99 Å and insertion energy of −0.64 eV, which is more stable than those at O2 (−0.30 eV) and O3 (−0.14 eV) as detailed in SI Section S1. The bond direction of the O−H bond points to the nearby O1 atom to form a H bond with the distance of 1.82 Å, as shown in Figure S1. This leads to a slight distortion of the VO_5 unit where V−O1, V−O2, and V−O3 bonds are lengthened to 1.80, 1.86, and 1.96 Å, respectively (Figure 2a).

The Bader charge analysis and spin density reveal that, upon insertion, the H atom ionizes and becomes H^+ where 0.63 e^- is transferred to localize at the connected V center, as shown in Figure 2a. The gap state of hybridized V 3d and O 2p also suggests the localization of the electron, as shown in Figure 2b (see also SI section S2). The electron localization accompanied by the local lattice distortion is known as a small polaron formation.[42,43]

It is noteworthy that the H concentration in V_2O_5 as predicted from their calculated formation energies could be up to $H_2V_2O_5$. As detailed in SI section S1, the formation energy of H incorporation at the O1 for $H_2V_2O_5$ (fully hydrogenated at the O1) is highly negative of −0.92 eV. Further H insertion

https://doi.org/10.1021/acsaem.3c00830
ACS Appl. Energy Mater. XXXX, XXX, XXX−XXX

Manuscript published in The Journal of ACS Applied Energy Materials

(journal impact factor = 6.959)

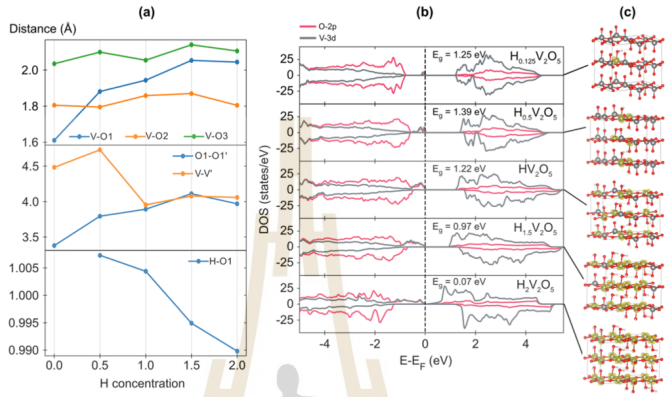

Figure 3. Effects of H contents on (a) local structures of α-V_2O_5 including V−O bond lengths, O1−O1′ and V−V′ distances in the [100] direction (inset) and H−O1 bond lengths (inset) and (b) electronic structures of projected density of states. Increasing H contents reduces the band gaps as (c) the extra electrons from the inserted H occupy V centers, generating states at the top of the valence band as shown in the yellow isosurface of 0.032 e $Å^{-3}$.

will need to protonate the O2 or the O3 sites which are energetically less stable with formation energies of −0.65 and −0.66 eV, respectively.

Next, we increased the H concentrations in the supercell, where the number of H atoms was varied from 4 to 16 corresponding with $H_xV_2O_5$ when x = 0.5 to 2. We find that the average V−O bond distance increases with increasing H concentrations. Predominantly, the V−O1 bond distances significantly increase from 1.61 Å (at x = 0) to 2.04 Å (at x = 2), while other V−O bonds only slightly change. In contrast, the O−H bond tends to be shortened upon the increased H concentration. The results indicate that the higher the H concentration in the V_2O_5 structure, the stronger the O−H bond but the weaker the V−O bond. High H concentrations also affect the distortion of lattice parameters of the α-V_2O_5 host from 11.60, 7.27, and 8.96 Å to 12.29, 7.54, and 8.12 Å ($H_2V_2O_5$) for lattice parameters a, b, and c, respectively; however, according to Jesus and Sai,[43,60] the puckering angle was determined for phase transition investigation that the phase of V_2O_5 will transform from the α phase to the δ phase with puckering angle change from 76° to 54°; we also find that the α-V_2O_5 phase does not change on high H concentration because puckering angle is changed from 77.43° to 88.65°. The increased puckering angle in $H_2V_2O_5$ is due to the repulsive forces introduced by the H ions between the O1 atoms in the crystal lattice.

In addition, the presence of the intercalated H atoms helps expand the ion diffusion channel in the b direction where the distance between the nearest O1−O1 increases from 3.37 to 3.53 Å (Figure 3a). Such an expansion of the diffusion channel could improve the ion transport kinetics of the cathode, which is discussed in Section 3.4. The H-inserted structure is also thermally stable at elevated temperatures, as suggested by ab initio molecular dynamic simulations that the O−H bonds are still intact within the considered simulated time of 1 ps, as detailed in SI Section S3.

To understand the electronic structures of $H_xV_2O_5$, we further analyzed their projected densities of states (PDOS). As shown in Figure 3b, the increased H concentrations narrow the band gap. For example, at x = 0.5, the extra electrons from the inserted H occupy several V centers, creating occupied extra states at the top of the valence band, as shown in the band decomposed charge density in Figure 3c. As the H concentrations increase (x = 1 and 1.5), the extra occupied states expand toward the conduction band leading to smaller band gaps. At the very high concentration of x = 2, the band gap is reduced to only 0.07 eV which is very close to the thermal energy at a room temperature of 0.03 eV. Such a small band gap could imply that the material exhibits a metal-like character at room temperature. The metal-like character was also proposed in the Li-intercalated V_2O_5 systems where the increased Li concentrations could lead to itinerant behavior of extra electrons.[43] The material is then expected to behave like metal at high H contents. Hence, it is suggested based on the computational results that the electronic conductivity of V_2O_5 is greatly improved upon H intercalation during the discharge process. However, our findings demonstrate that while the band gap generally decreases with increasing H concentrations in $H_xV_2O_5$, certain arrangements of H and its polaron can lead to nonsymmetric distributions and localized distortions, resulting in deviations from the general trend of band gap reduction, as detailed in SI section S4.

Then, we studied Mg insertion where two possible ion−polaron configurations were examined, as detailed in SI section S5. We find that the most stable configuration corresponds to the localization of the two electrons from the Mg atom at two V centers with an insertion energy of −5.39 eV. On the other hand, the other configuration with the distribution of the two electrons at four V centers exhibits a less stable insertion energy of −4.87 eV, as shown in Figure S6. The results indicate that upon intercalation, Mg ionizes and provides two electrons localized at the two nearby V centers forming two polarons, as shown in the spin density (Figure 4a) and localized gap states in the PDOS plot (Figure 4b).

The formation of two polarons and electrostatic interactions between Mg^{2+} and electronegative oxygen atoms induce

https://doi.org/10.1021/acsaem.3c00830
ACS Appl. Energy Mater. XXXX, XXX, XXX−XXX

Manuscript published in The Journal of ACS Applied Energy Materials

(journal impact factor = 6.959)

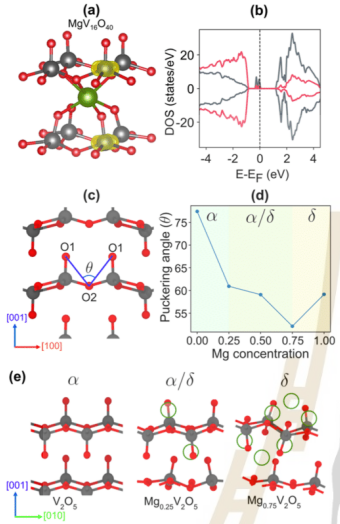

Figure 4. Sketches of (a) the local structure of Mg insertion in the α-V_2O_5. Upon insertion, Mg ionizes and forms two polarons at the two nearby VO_5 units (yellow isosurface) which correspond with the (b) gap states of the projected density of states. At high Mg contents, it induces phase transition from α to δ as characterized by (c) the puckering angle of O1−O2−O1. (d) The puckering angle decreases as the Mg concentration increases, while (e) the structure transforms from the α to δ phase.

greater in-plane distortion than that of H insertion. The two polaronic VO_5 units exhibit in-plane V−O2 and V−O3 bond elongation greater than that of the H insertion by up to 0.1 Å, as detailed in SI Section S2. However, the H insertion leads to greater V−O1 bond lengthening than that of the Mg insertion (1.80 vs 1.67 Å). This is because the inserted H forms a chemical bond with the O1 which in turn weakens the V−O1 bond resulting in a greater bond lengthening.

Due to the large in-plane distortion upon Mg insertion, it is expected that a higher Mg content could lead to long-range distortion and result in structural transformation. Such phase transition was investigated by measuring the puckering angle (θ) of O1−O2−O1 within the layer, as shown in Figure 4c. It has been reported that α-V_2O_5 displays a puckering angle of 76°, while it decreases to 54° when the phase changes to δ-V_2O_5.[60] As shown in Figure 4c−e, we find that the puckering angle decreases from 76° to 52° and 60° when the Mg concentration increases from x = 0 to 0.75 and 1.00, respectively. The results imply that the V_2O_5 phase changes from α to δ at Mg concentration higher than 0.75, as shown in Figure 4d which corresponds with the structures in Figure 4e.

It is noteworthy that at higher Mg concentrations, the electronic structures are similar to those of H insertion where the band gap decreases with increasing Mg concentration and eventually becomes metallic as the occupied extra states reach the conduction band, as shown in Figure S7.

In summary, we find that the electronic property of V_2O_5 has changed from semiconductor to metal-like at high H or Mg contents. This is due to the overlapping of extra states originating from ion insertion. Hence, such insertions greatly improve the electronic conductivity of the cathode. In addition, the phase transition is expected to occur at high Mg contents, while the insertion of H even at high concentrations does not significantly affect long-range lattice distortion.

3.3. H and Mg Diffusion. During the discharge process, the water-containing electrolyte could provide intercalated H in the V_2O_5 cathode.[24,27−29,59,61−63] At the same time, Mg ions from the anode diffuse through the electrolyte and intercalate into the cathode. To determine their diffusion kinetics, both H and Mg, we calculated their diffusion barriers in the 1 × 3 × 3 V_2O_5 supercell. The obtained results could be used to suggest the effect of H insertion on the intercalation behavior of Mg, as further discussed in Sections 3.4 and 3.5.

First, we explored the kinetics of the H diffusion. As discussed in the previous section, H prefers to bind with the vanadyl oxygen, while its electron mainly localizes at the V center forming a polaron at the VO_5 unit and yielding H^+. To describe the diffusion of H, we considered both H^+ and polaron migration from one VO_5 unit to the nearby VO_5 unit in the [010] direction, which is the preferred direction of H and other ion migration in V_2O_5.[27] To account for their coupled movements, we considered three different scenarios, including (i) proton-coupled polaron transfer, (ii) proton diffusion prior to polaron transfer, and (iii) polaron transfer prior to proton diffusion, as schematically shown in Figure 5.

As shown in Figure 5, all considered scenarios exhibit similar effective barriers in the range of 0.5−0.6 eV, with the first scenario, proton-coupled electron transfer, being the most favorable one with a barrier of 0.49 eV (Figure 5a). The other

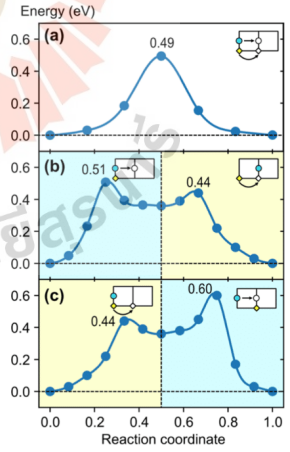

Figure 5. Energy profile of proton and polaron migration in the α-V_2O_5 structure: (a) proton-coupled polaron transfer, (b) proton diffusion prior to polaron transfer, and (c) polaron transfer prior to proton diffusion. The insets schematically define the order of migration where the α-V_2O_5 structure, proton, and polaron are represented by squares, cyan circles, and yellow diamonds, respectively.

https://doi.org/10.1021/acsaem.3c00830
ACS Appl. Energy Mater. XXXX, XXX, XXX−XXX

Manuscript published in The Journal of ACS Applied Energy Materials

(journal impact factor = 6.959)

two scenarios, where the proton and polaron move separately, display somewhat higher effective barriers of 0.51 and 0.60 eV for scenarios (ii) and (iii), respectively (Figure 5b,c). This implies that the proton and its electron prefer to stay close to one another at the same VO_5 unit, where separate movements are less favorable with higher barriers. In other words, Coulombic attraction between ion and electron penalizes such separate movements leading to high-energy configurations and less favorable scenarios. The results are consistent with previous computational works that reported the coupled movements of ions and polarons in V_2O_5[42] and $LiFePO_4$.[64]

Next, we explored the diffusion behavior of Mg. As discussed in Section 3.2, an inserted Mg ionizes and provides two polarons at the two nearby VO_5 units. Like H diffusion, we only considered the diffusion in the [010] direction since it is the most favorable path,[49] as detailed in SI Section S7, and explored their movements in the coupled and separate fashion, as shown in Figure 6. We find that the coupled ion−polaron transfer, involving Mg^{2+} and two polarons, is most favorable with an effective barrier of 0.93 eV (Figure 6a).

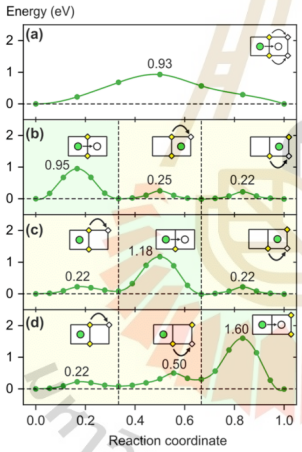

Figure 6. Energy profile of a Mg−two-polaron migration: (a) Mg−two-polaron coupled migration, (b) Mg migration occurs before polaron migration, (c) Mg migration occurs after one polaron migration, and (d) Mg migration occurs after two polarons migration. The insets schematically define the order of migration where the α-V_2O_5 structure, Mg, and polaron are indicated by squares, green circles, and yellow daimons, respectively.

Other scenarios had separate movements of ions and polarons (the schematic is shown in Figure S9) suffering from ion−polaron Coulombic penalties leading to slightly higher effective barriers in the range of 0.95−1.60 eV (Figure 6b,d). As shown in Figure 6b, when the Mg ion moves in the vicinity of the two polarons, it displays only a slightly higher barrier than that of the coupled motion (0.95 vs 0.93 eV). In contrast, when there is only one or no polarons close to the diffusion path, the Mg ion diffuses much more slowly with the barriers of 1.18 and 1.60 eV, respectively (Figure 6c,d). The Coulombic penalty for Mg^{2+} is more pronounced than that for H^+ migration due to the higher net charges of the Mg ion. Our calculated barrier of the preferred diffusion scenario is lower than the previously reported values of 1.28[27] and 1.29 eV.[49] The origin of such differences is unclear due to the absence of polaron configurations in previous computational works.

Overall, the results suggest that H diffuses much faster than Mg with effective barriers of 0.49 and 0.93 eV, respectively. It is expected that at the beginning of the discharge process, H from the dissociated water molecule in the electrolyte first intercalated into V_2O_5, followed by slow Mg diffusion from the anode. The structure of V_2O_5 may contain a significant amount of H before the intercalation of Mg. Such a conclusion is consistent with that observed in experiments of aqueous electrolytes in the V_2O_5-based cathode for Zn-ion batteries.[22,59] In addition, the stable insertion and fast diffusion of H in the lattice could improve the specific capacity of the cathode, where inserted H and its polaron serve as charge carriers.

3.4. Effect of H Insertion on Mg Diffusion Kinetics. As discussed in the previous section, insertion of H from dissociated aqueous electrolytes is much faster than Mg insertion, owing to low diffusion barriers of proton-coupled polaron transfer. It is expected that during the discharge process, the H-inserted structures, $H_xV_2O_5$, are formed prior to Mg intercalation. Hence, in this section, we explored the effect of protonated structures on the diffusion behavior of Mg.

We considered the high concentration of H where all vanadyl oxygen atoms are protonated, corresponding to the $H_2V_2O_5$ structure. The Mg-ion diffusion path is along the [010] direction. The migration of polarons is not considered due to the itinerant behavior of $H_2V_2O_5$ where extra electrons from H are expected to delocalize throughout the lattice as discussed in Section 3.2 and previously reported in highly lithiated V_2O_5.[43]

As shown in Figure 7, at a high concentration of H, the diffusion barrier of Mg is 0.23 eV which is much lower than that in the pristine structure (0.93 eV). This is because H insertion enlarges the diffusion channel in the [010] direction, as discussed in Section 3.2. The transition state (TS) structures reveal that the distances between Mg and nearest O atoms in the H-inserted system are 0.03−0.09 Å greater than that of the pristine system (Figure 7b). Such a more relaxed TS structure yields a more stable TS energy, leading to a lower diffusion barrier and fast kinetics. This also implies that H insertion at O1 reduces the electronegative charge of O which results in the larger O1−O1 distance and expanded diffusion channel. Our calculated results are consistent with a previous DFT study[27] and experimental observations[17] that H insertion could improve the Mg diffusion kinetics. Such facile ion movements in the H-inserted structure could alleviate the capacity fading caused by slow diffusion kinetics or trapped ions in the V_2O_5 structure.[65−67] We also provided the Mg−O distance during Mg migration in Figure S10.

3.5. Effect of H Insertion on the Suppression of Phase Transition upon Mg Intercalation. The V_2O_5 crystal structure processes four different phases, including α, ε, δ, and γ. Among them, α-V_2O_5 has been widely used as cathode materials for metal-ion batteries due to its high theoretical capacity and stability.[68] However, at deep discharge with high ion concentration, it has been reported that the α-phase irreversibly changes to other phases.[60] A previous computational study reveals that α-V_2O_5 could transform to δ-V_2O_5 at Li concentration greater than 0.75 mole ratio

https://doi.org/10.1021/acsaem.3c00830
ACS Appl. Energy Mater. XXXX, XXX, XXX−XXX

Manuscript published in The Journal of ACS Applied Energy Materials

(journal impact factor = 6.959)

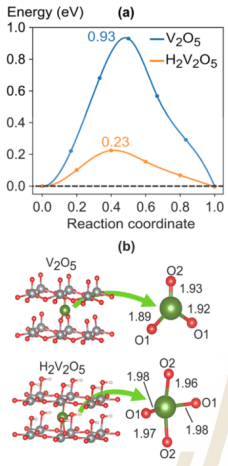

Figure 7. (a) Energy profile of Mg diffusion in the [010] direction in V_2O_5 and $H_2V_2O_5$. (b) Transition state structures of Mg diffusion in the protonated structures are more relaxed with longer Mg−O distances. The labeled bond distances are in angstrom.

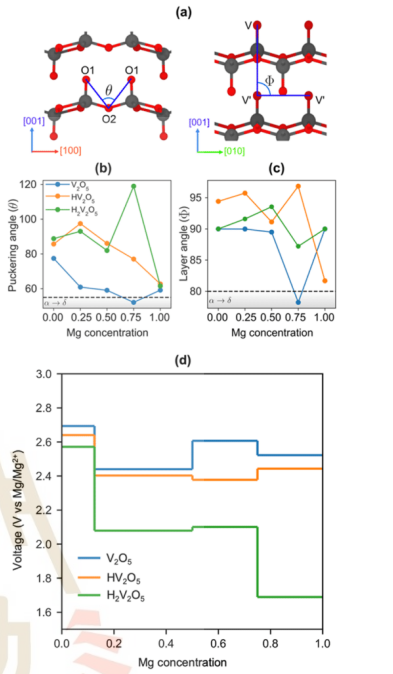

Figure 8. (a) Schematic illustration of puckering and layered angles used to characterize the α to δ phase change. The relationship between intercalated Mg concentrations with (b) puckering and (c) layered angles. H insertion prevents the α–δ phase change. (d) Voltage profile of $H_xV_2O_5$ during Mg insertion.

$(Li_{0.75}V_2O_5)$.[9,46,49] The phase transition is induced by strong electrostatic forces between the intercalated ions and the V_2O_5 host. Such irreversible phase changes lead to poor cyclability of the battery and low ion utilization.[68,69]

Herein, we systematically study the effect of H insertion on the suppression of the α-V_2O_5 phase transition upon Mg intercalation. As shown in Figure 8a, we determine the α–δ phase alteration by monitoring the changes in the puckering angle (θ) of the O1−O2−O1 and layered angle (Φ) of the V−V−V upon increasing of Mg concentrations. The α-phase exhibits the θ of 76° and Φ of 90°, whereas the δ-phase displays the θ of 56° and Φ of 80°. As shown in Figure 8b,c, we find that the fully protonated structure ($H_2V_2O_5$) exhibits puckering (62°) and layered angles (90°) close to the pristine α-V_2O_5, suggesting that H insertion preserved the α-phase even at high concentrations.

As the concentration of Mg increases, the puckering and layered angles of pristine V_2O_5 change from those of the α to δ phase. The phase change is predicted to occur at the concentration of $Mg_{0.75}V_2O_5$ with puckering (52°) and layered angles (78°) smaller than the threshold of the δ phase. Such large distortions upon Mg insertion originate from the strong electrostatic interactions between Mg^{2+} and the electronegative lattice of the O atoms. Our results are consistent with previous computational studies that for the V_2O_5-based cathode used in Li-ion batteries, V_2O_5 was transformed from the α to ε phase at a Li concentration of 0.3−0.7 and to the δ phase at a Li concentration of 0.8. Also, for the Mg-ion batteries, V_2O_5 changes to the δ phase at the Mg concentration of 0.75.[49] Furthermore, an experimental study found that the phase of the lithiated V_2O_5 cathode was irreversibly changed to the ω phase at a Li concentration of 3.[69]

Remarkably, the presence of H in the structure could effectively reduce the distortion upon Mg insertion. As shown in Figure 8b,c, the puckering and layered angles are less affected as the Mg concentrations increase. The H-inserted structures are predicted to maintain their α phases throughout the considered Mg concentrations. This is because the H insertion yields protonated O1 atoms that could weaken the electrostatic interaction between the Mg ion and the lattice, resulting in smaller structural distortion.

Such an explanation is supported by the Bader charges of the atom O1 upon protonation. The average charge transfer into O1 atoms decreases from 0.41 to 0.25 and 0.12 e^- when Mg inserts in HV_2O_5 and $H_2V_2O_5$, respectively. In contrast, the average charge of Mg atoms decreases from +1.72 to +1.69 and +1.68 e^- when they insert into pure V_2O_5, HV_2O_5, and $H_2V_2O_5$, respectively. The results suggest that the H insertion into the V_2O_5 structure reduces charge transfer from the inserted Mg to the lattice, which could lead to weaker Mg−lattice interactions.

In addition, we also investigated the effect of H insertion on the discharge voltage profiles. This can be done by calculating the open-circuit voltage (OCV) profile at different H and Mg concentrations in $H_xV_2O_5$ using the following equation (as described in detail in SI Section S10)

https://doi.org/10.1021/acsaem.3c00830
ACS Appl. Energy Mater. XXXX, XXX, XXX−XXX

Manuscript published in The Journal of ACS Applied Energy Materials

(journal impact factor = 6.959)

$$\mathrm{OCV}(y) = -\frac{E_{\mathrm{Mg}_y\mathrm{H}_x\mathrm{V}_2\mathrm{O}_5} - E_{\mathrm{H}_x\mathrm{V}_2\mathrm{O}_5} - yE_{\mathrm{Mg}}}{y2e} \quad (2)$$

where $E_{\mathrm{Mg}_y\mathrm{H}_x\mathrm{V}_2\mathrm{O}_5}$, $E_{\mathrm{H}_x\mathrm{V}_2\mathrm{O}_5}$, and E_{Mg} are the total energies of the Mg-inserted $H_xV_2O_5$ structure, the $H_xV_2O_5$ structure, and chemical potential of Mg atoms taken from bulk Mg structure, respectively.

As shown in Figure 8d, the discharge voltage of V_2O_5 decreases from 2.69 to 2.52 V as the Mg concentration increases from 0.125 to 1. The voltage then increases from 2.44 to 2.61 V as the Mg concentrations increases from 0.50 to 0.75. The nonmonotonic changes of discharge voltage in this region could be attributed to the structural distortion at high Mg concentrations as depicted in Figure 8b,c.

H insertion could lead to a decrease in the initial voltage. Specifically, the OCV of $H_xV_2O_5$ with H concentrations of 0, 1, and 2 decreases from 2.69 to 2.64 and 2.57 V, respectively. This suggests that the introduction of H atoms weakens the interactions between Mg ions and the α-V_2O_5 lattice. This weakening can be attributed to the screening effect induced by the protonation of O1 atoms. Our calculated OCV values at low Mg concentration ($Mg_{0.125}V_2O_5$) are in good agreement with those reported in other DFT works within the range of 2.34−2.70 V, as summarized in Table S1.[9,60,70] Furthermore, our calculated OCV for V_2O_5 (2.52 V) and $H_2V_2O_5$ (1.69 V) are in agreement with previous computational work with the reported OCV of V_2O_5 (2.30 V) and $H_2V_2O_5$ (1.70 V).[27]

To sum up, our results show that H insertion can improve the structural stability of V_2O_5 upon Mg intercalation. This agrees with the experimentally observed long-life cycle and high capacity when the aqueous electrolyte is used.[19,30,59] It is suggested that the inserted H prevents the α−δ phase transition by reducing the electrostatic interaction between Mg and lattice O, leading to the improved cyclability of the cathode, since it helps maintain the α phase where further irreversible phases are less likely to form. Nevertheless, it has been reported that the δ phase could facilitate ion transport kinetics by lowering the diffusion barriers,[60] but such phase transitions could yield other irreversible phases at high Mg concentrations.

4. CONCLUSIONS

Previous experimental studies suggest that when an aqueous electrolyte is used, water molecules could dissociate at the electrolyte−electrode interface and provide H that can intercalate into the V_2O_5 cathode. The inserted H greatly improves the electrochemical performance of the V_2O_5 cathode. In this work, we employed density functional theory to study the effects of H insertion on the improved electronic conductivity, ion transport kinetics, and structural stability of the V_2O_5 cathode of Mg-ion batteries. Computations reveal that the inserted H prefers to bind with vanadyl oxygen and donates an extra electron localized at the V center, forming a small polaron. As the concentration of H increases, the extra electrons occupy several V centers creating occupied states at the top of the valence band leading to a smaller band gap, which enhances the electronic conductivity of the materials. The inserted H can account for charge carriers which could improve the specific capacity of the cathode.

Similar electronic structures are observed upon Mg insertion; the higher the Mg concentration, the smaller the band gap. Nevertheless, the high content of Mg creates long-range structural distortion due to strong ion−lattice interactions, which could lead to α to δ phase transition. The phase change is not desired, as it could lead to irreversible phase transformation where Mg cannot deintercalate from the cathode. This is the main cause of the poor cyclability and capacity fading.

Adding a small amount of water could promote Mg diffusion and suppress the phase transition. During the discharge process, dissociated H from the aqueous electrolyte can intercalate into the cathode. The effective barriers of ion-coupled polaron transfer for H and Mg are 0.49 and 0.93 eV, respectively. This indicates that H can diffuse much faster than Mg in the investigated system. It is expected that during the discharge process, the cathode contains a high H content before Mg intercalation. The preinserted H significantly reduces the Mg diffusion barrier from 0.93 to 0.23 eV, which greatly hastens the ion diffusion kinetics. In addition, the preinserted H inhibits the α to δ phase transition upon Mg intercalation. This is because it reduces the electrostatic interaction between the Mg ion and the lattice as the vanadyl oxygen becomes less electronegative when it is protonated.

Our study not only investigated the effect of H concentration on electronic and kinetic properties but also considered the influence of polaron configuration and structural stability, providing a comprehensive understanding of the migration behavior in $H_xV_2O_5$-based cathodes for Mg-ion batteries. While our study focused on first-principles computations, our results align with previous experimental findings on $H_xV_2O_5$ cathodes, suggesting improved electronic conductivity and electrochemical performance. Our insights provide valuable guidance for future experimental investigations. These findings could be used to rationally design the strategy to improve the electrochemical performance of the V_2O_5 cathode of Mg-ion batteries.

■ ASSOCIATED CONTENT

Supporting Information

The Supporting Information is available free of charge at https://pubs.acs.org/doi/10.1021/acsaem.3c00830.

H adsorption site verification (Section S1); relation between the d-orbitals of V atoms and polaron formation (Section S2); complex phenomenon in the band gap of $H_xV_2O_5$ (Section S3); thermal stability investigation of the $H_2V_2O_5$ structure (Section S4); MgV_2O_5 configurations (Section S5); electronic property of $Mg_yV_2O_5$ (Section S6); Mg migration in V_2O_5 investigation (Section S8); ion and polaron migration configurations (Section S8); O-environmental atom during Mg migration (Section S9); and open-circuit voltage (OCV) of Mg-ion insertion into $H_xV_{16}O_{40}$ (Section S10) (PDF)

■ AUTHOR INFORMATION

Corresponding Authors

Anchalee Junkaew − *National Nanotechnology Center (NANOTEC), National Science and Technology Development Agency (NSTDA), Pathum Thani 12120, Thailand;* orcid.org/0000-0002-3193-1110; Email: anchalee@nanotec.or.th

Suwit Suthirakun − *School of Chemistry, Institute of Science, Suranaree University of Technology, Nakhon Ratchasima*

https://doi.org/10.1021/acsaem.3c00830
ACS Appl. Energy Mater. XXXX, XXX, XXX−XXX

Manuscript published in The Journal of ACS Applied Energy Materials

(journal impact factor = 6.959)

30000, Thailand; orcid.org/0000-0002-6590-6343; Email: suthirak@sut.ac.th

Authors

Panupol Untarabut – *School of Physics, Institute of Science, Suranaree University of Technology, Nakhon Ratchasima 30000, Thailand*

Sirisak Singsen – *School of Physics, Institute of Science, Suranaree University of Technology, Nakhon Ratchasima 30000, Thailand*

Lappawat Ngamwongwan – *School of Physics, Institute of Science, Suranaree University of Technology, Nakhon Ratchasima 30000, Thailand*

Ittipon Fongkaew – *School of Physics, Institute of Science, Suranaree University of Technology, Nakhon Ratchasima 30000, Thailand*

Complete contact information is available at: https://pubs.acs.org/10.1021/acsaem.3c00830

Notes

The authors declare no competing financial interest.

■ ACKNOWLEDGMENTS

This work was supported by (i) Suranaree University of Technology (SUT), (ii) Thailand Science Research and Innovation (TSRI), (iii) National Science, Research and Innovation Fund (NSRF) (NRIIS Project Numbers 4366696), and (iv) National Research Council of Thailand (Grant Number N42A650325). The authors would like to thank the NSTDA Supercomputer Center (ThaiSC) for computational resources.

■ REFERENCES

(1) Yoo, H. D.; Shterenberg, I.; Gofer, Y.; Gershinsky, G.; Pour, N.; Aurbach, D. Mg Rechargeable Batteries: An on-Going Challenge. *Energy Environ. Sci.* **2013**, *6* (8), 2265.

(2) Orikasa, Y.; Masese, T.; Koyama, Y.; Mori, T.; Hattori, M.; Yamamoto, K.; Okado, T.; Huang, Z. D.; Minato, T.; Tassel, C.; Kim, J.; Kobayashi, Y.; Abe, T.; Kageyama, H.; Uchimoto, Y. High Energy Density Rechargeable Magnesium Battery Using Earth-Abundant and Non-Toxic Elements. *Sci. Rep* **2014**, *4*, No. 5622.

(3) Verma, J.; Kumar, D. Metal-Ion Batteries for Electric Vehicles: Current State of the Technology, Issues and Future Perspectives. *Nanoscale Adv.* **2021**, *3* (12), 3384–3394.

(4) Davidson, R.; Verma, A.; Santos, D.; Hao, F.; Fincher, C.; Xiang, S.; Van Buskirk, J.; Xie, K.; Pharr, M.; Mukherjee, P. P.; Banerjee, S. Formation of Magnesium Dendrites During Electrodeposition. *ACS Energy Lett.* **2019**, *4* (2), 375–376.

(5) Zhao, Y.; Zhang, X.; Xiao, J.; Fan, H.; Zhang, J.; Liu, H.; Liu, Y.; Yuan, H.; Fan, S.; Zhang, Y. Effect of Mg Cation Diffusion Coefficient on Mg Dendrite Formation. *ACS Appl. Mater. Interfaces* **2022**, *14* (5), 6499–6506.

(6) Pavčnik, T.; Bitenc, J.; Pirnat, K.; Dominko, R. Electrochemical Performance of Mg Metal-Quinone Battery in Chloride-Free Electrolyte. *Batteries Supercaps* **2021**, *4* (5), 815–822.

(7) Bae, J.; Park, H.; Guo, X.; Zhang, X.; Warner, J. H.; Yu, G. High-Performance Magnesium Metal Batteries Via Switching the Passivation Film into a Solid Electrolyte Interphase. *Energy Environ. Sci.* **2021**, *14* (8), 4391–4399.

(8) Tian, H.; Gao, T.; Li, X.; Wang, X.; Luo, C.; Fan, X.; Yang, C.; Suo, L.; Ma, Z.; Han, W.; Wang, C. High Power Rechargeable Magnesium/Iodine Battery Chemistry. *Nat. Commun.* **2017**, *8*, No. 14083.

(9) Zhao, X.; Zhang, X.; Wu, D.; Zhang, H.; Ding, F.; Zhou, Z. Ab Initio Investigations on Bulk and Monolayer V2O5 as Cathode Materials for Li-, Na-, K- and Mg-Ion Batteries. *J. Mater. Chem A* **2016**, *4* (42), 16606–16611.

(10) Zhang, X.; Wang, J. G.; Liu, H.; Liu, H.; Wei, B. Facile Synthesis of V(2)O(5) Hollow Spheres as Advanced Cathodes for High-Performance Lithium-Ion Batteries. *Materials* **2017**, *10* (1), 77.

(11) Andrews, J. L.; Mukherjee, A.; Yoo, H. D.; Parija, A.; Marley, P. M.; Fakra, S.; Prendergast, D.; Cabana, J.; Klie, R. F.; Banerjee, S. Reversible Mg-Ion Insertion in a Metastable One-Dimensional Polymorph of V2O5. *Chem* **2018**, *4* (3), 564–585.

(12) Verrelli, R.; Black, A. P.; Pattanathummasid, C.; Tchitchekova, D. S.; Ponrouch, A.; Oró-Solé, J.; Frontera, C.; Bardé, F.; Rozier, P.; Palacín, M. R. On the Strange Case of Divalent Ions Intercalation in V2O5. *J. Power Sources* **2018**, *407*, 162–172.

(13) Murata, Y.; Takada, S.; Obata, T.; Tojo, T.; Inada, R.; Sakurai, Y. Effect of Water in Electrolyte on the Ca2+ Insertion/Extraction Properties of V2O5. *Electrochim. Acta* **2019**, *294*, 210–216.

(14) Cao, J.; Zhang, D.; Yue, Y.; Pakornchote, T.; Bovornratanaraks, T.; Sawangphruk, M.; Zhang, X.; Qin, J. Revealing the Impacts of Oxygen Defects on Zn2+ Storage Performance in V2O5. *Mater. Today Energy* **2021**, *21*, No. 100824.

(15) Rocquefelte, X.; Boucher, F.; Gressier, P.; Ouvrard, G. First-Principle Study of the Intercalation Process in the LixV2O5 System. *Chem. Mater.* **2003**, *15* (9), 1812–1819.

(16) Drosos, C.; Jia, C.; Mathew, S.; Palgrave, R. G.; Moss, B.; Kafizas, A.; Vernardou, D. Aerosol-Assisted Chemical Vapor Deposition of V2O5 Cathodes with High Rate Capabilities for Magnesium-Ion Batteries. *J. Power Sources* **2018**, *384*, 355–359.

(17) Wang, F.; Fan, X.; Gao, T.; Sun, W.; Ma, Z.; Yang, C.; Han, F.; Xu, K.; Wang, C. High-Voltage Aqueous Magnesium Ion Batteries. *ACS Cent Sci.* **2017**, 3 (10), 1121–1128.

(18) Zhou, B.; Shi, H.; Cao, R.; Zhang, X.; Jiang, Z. Theoretical Study on the Initial Stage of a Magnesium Battery Based on a V2O5 Cathode. *Phys. Chem. Chem. Phys.* **2014**, *16* (34), 18578–18585.

(19) Liang, Y.; Jing, Y.; Gheytani, S.; Lee, K. Y.; Liu, P.; Facchetti, A.; Yao, Y. Universal Quinone Electrodes for Long Cycle Life Aqueous Rechargeable Batteries. *Nat. Mater.* **2017**, *16* (8), 841–848.

(20) Wan, F.; Zhang, L.; Dai, X.; Wang, X.; Niu, Z.; Chen, J. Aqueous Rechargeable Zinc/Sodium Vanadate Batteries with Enhanced Performance from Simultaneous Insertion of Dual Carriers. *Nat. Commun.* **2018**, *9* (1), No. 1656.

(21) Wu, X.; Ji, X. Aqueous Batteries Get Energetic. *Nat. Chem* **2019**, *11* (8), 680–681.

(22) Liu, X.; Euchner, H.; Zarrabeitia, M.; Gao, X.; Elia, G. A.; Groß, A.; Passerini, S. Operando Ph Measurements Decipher H+/Zn2+ Intercalation Chemistry in High-Performance Aqueous Zn/Δ-V2O5 Batteries. *ACS Energy Lett.* **2020**, 5 (9), 2979–2986.

(23) Karapidakis, E.; Vernardou, D. Progress on V2O5 Cathodes for Multivalent Aqueous Batteries. *Materials* **2021**, *14* (9), 2310.

(24) Zhou, L.; Liu, L.; Hao, Z.; Yan, Z.; Yu, X.-F.; Chu, P. K.; Zhang, K.; Chen, J. Opportunities and Challenges for Aqueous Metal-Proton Batteries. *Matter* **2021**, *4* (4), 1252–1273.

(25) Cao, J.; Zhang, D.; Yue, Y.; Pakornchote, T.; Bovornratanaraks, T.; Zhang, X.; Zeng, Z.; Qin, J.; Huang, Y. Boosting Zn(2+) Diffusion Via Tunnel-Type Hydrogen Vanadium Bronze for High-Performance Zinc Ion Batteries. *ACS Appl. Mater. Interfaces* **2022**, *14* (6), 7909–7916.

(26) Xu, Y.; Deng, X.; Li, Q.; Zhang, G.; Xiong, F.; Tan, S.; Wei, Q.; Lu, J.; Li, J.; An, Q.; Mai, L. Vanadium Oxide Pillared by Interlayer Mg2+ Ions and Water as Ultralong-Life Cathodes for Magnesium-Ion Batteries. *Chem* **2019**, *5* (5), 1194–1209.

(27) Ni, D.; Shi, J.; Xiong, W.; Zhong, S.; Xu, B.; Ouyang, C. The Effect of Protons on the Mg(2+) Migration in an Alpha-V2O5 Cathode for Magnesium Batteries: A First-Principles Investigation. *Phys. Chem. Chem. Phys.* **2019**, *21* (14), 7406–7411.

(28) Park, M. J.; Yaghoobnejad Asl, H.; Manthiram, A. Multivalent-Ion Versus Proton Insertion into Battery Electrodes. *ACS Energy Lett.* **2020**, *5* (7), 2367–2375.

(29) Zhao, Q.; Liu, L.; Yin, J.; Zheng, J.; Zhang, D.; Chen, J.; Archer, L. A. Proton Intercalation/De-Intercalation Dynamics in Vanadium

https://doi.org/10.1021/acsaem.3c00830
ACS Appl. Energy Mater. XXXX, XXX, XXX–XXX

Manuscript published in The Journal of ACS Applied Energy Materials

(journal impact factor = 6.959)

Oxides for Aqueous Aluminum Electrochemical Cells. *Angew. Chem., Int. Ed. Engl.* **2020**, *59* (8), 3048−3052.
(30) Sa, N.; Wang, H.; Proffit, D. L.; Lipson, A. L.; Key, B.; Liu, M.; Feng, Z.; Fister, T. T.; Ren, Y.; Sun, C.-J.; Vaughey, J. T.; Fenter, P. A.; Persson, K. A.; Burrell, A. K. Is Alpha-V2O5 a Cathode Material for Mg Insertion Batteries? *J. Power Sources* **2016**, *323*, 44−50.
(31) Kresse, G.; Hafner, J. Ab Initio Molecular Dynamics for Liquid Metals. *Phys. Rev. B: Condens. Matter* **1993**, *47* (1), 558−561.
(32) Amadon, B.; Lechermann, F.; Georges, A.; Jollet, F.; Wehling, T. O.; Lichtenstein, A. I. Plane-Wave Based Electronic Structure Calculations for Correlated Materials Using Dynamical Mean-Field Theory and Projected Local Orbitals. *Phys. Rev. B* **2008**, *77* (20), No. 205112.
(33) Dudarev, S. L.; Botton, G. A.; Savrasov, S. Y.; Humphreys, C. J.; Sutton, A. P. Electron-Energy-Loss Spectra and the Structural Stability of Nickel Oxide: An Lsda+U Study. *Phys. Rev. B* **1998**, *57* (3), 1505−1509.
(34) Ngamwongwan, L.; Fongkaew, I.; Jungthawan, S.; Hirunsit, P.; Limpijumnong, S.; Suthirakun, S. Electronic and Thermodynamic Properties of Native Point Defects in V(2)O(5): A First-Principles Study. *Phys. Chem. Chem. Phys.* **2021**, *23* (19), 11374−11387.
(35) Klimes, J.; Bowler, D. R.; Michaelides, A. Chemical Accuracy for the Van Der Waals Density Functional. *J. Phys.: Condens. Matter* **2010**, *22* (2), No. 022201.
(36) Klimeš, J.; Bowler, D. R.; Michaelides, A. Van Der Waals Density Functionals Applied to Solids. *Phys. Rev. B* **2011**, *83* (19), No. 195131.
(37) Perdew, J. P.; Burke, K.; Ernzerhof, M. Generalized Gradient Approximation Made Simple. *Phys. Rev. Lett.* **1996**, *77* (18), 3865−3868.
(38) Monkhorst, H. J.; Pack, J. D. Special Points for Brillouin-Zone Integrations. *Phys. Rev. B* **1976**, *13* (12), 5188−5192.
(39) Henkelman, G.; Uberuaga, B. P.; Jónsson, H. A Climbing Image Nudged Elastic Band Method for Finding Saddle Points and Minimum Energy Paths. *J. Chem. Phys.* **2000**, *113* (22), 9901−9904.
(40) Tang, W.; Sanville, E.; Henkelman, G. A Grid-Based Bader Analysis Algorithm without Lattice Bias. *J. Phys.: Condens. Matter* **2009**, *21* (8), No. 084204.
(41) Delmas, C.; Cognac-Auradou, H.; Cocciantelli, J. M.; Ménétrier, M.; Doumerc, J. P. The LixV2O5 System: An Overview of the Structure Modifications Induced by the Lithium Intercalation. *Solid State Ionics* **1994**, *69* (3), 257−264.
(42) Suthirakun, S.; Genest, A.; Rösch, N. Modeling Polaron-Coupled Li Cation Diffusion in V2O5 Cathode Material. *J. Phys. Chem. C* **2018**, *122* (1), 150−157.
(43) De Jesus, L. R.; Andrews, J. L.; Parija, A.; Banerjee, S. Defining Diffusion Pathways in Intercalation Cathode Materials: Some Lessons from V2O5 on Directing Cation Traffic. *ACS Energy Lett.* **2018**, *3* (4), 915−931.
(44) McNulty, D.; Noel Buckley, D.; O'Dwyer, C. NaV2O5 from Sodium Ion-Exchanged Vanadium Oxide Nanotubes and Its Efficient Reversible Lithiation as a Li-Ion Anode Material. *ACS Appl. Energy Mater.* **2019**, *2* (1), 822−832.
(45) Liu, Q.; Hu, Z.; Chen, M.; Zou, C.; Jin, H.; Wang, S.; Chou, S. L.; Dou, S. X. Recent Progress of Layered Transition Metal Oxide Cathodes for Sodium-Ion Batteries. *Small* **2019**, *15* (32), No. 1805381.
(46) McColl, K.; Cora, F. Phase Stability of Intercalated V2O5 Battery Cathodes Elucidated through the Goldschmidt Tolerance Factor. *Phys. Chem. Chem. Phys.* **2019**, *21* (15), 7732−7744.
(47) Lim, S. C.; Lee, J.; Kwak, H. H.; Heo, J. W.; Chae, M. S.; Ahn, D.; Jang, Y. H.; Lee, H.; Hong, S. T. Unraveling the Magnesium-Ion Intercalation Mechanism in Vanadium Pentoxide in a Wet Organic Electrolyte by Structural Determination. *Inorg. Chem.* **2017**, *56* (14), 7668−7678.
(48) Enjalbert, R.; Galy, J. A Refinement of the Structure of V2O5. *Acta Crystallogr., Sect. C* **1986**, *42* (11), 1467−1469.
(49) Xiao, R.; Xie, J.; Luo, T.; Huang, L.; Zhou, Y.; Yu, D.; Chen, C.; Liu, Y. Phase Transformation and Diffusion Kinetics of V2O5 Electrode in Rechargeable Li and Mg Batteries: A First-Principle Study. *J. Phys. Chem. C* **2018**, *122* (3), 1513−1521.
(50) Parija, A.; Liang, Y.; Andrews, J. L.; De Jesus, L. R.; Prendergast, D.; Banerjee, S. Topochemically De-Intercalated Phases of V2O5 as Cathode Materials for Multivalent Intercalation Batteries: A First-Principles Evaluation. *Chem. Mater.* **2016**, *28* (16), 5611−5620.
(51) Maganas, D.; Roemelt, M.; Havecker, M.; Trunschke, A.; Knop-Gericke, A.; Schlogl, R.; Neese, F. First Principles Calculations of the Structure and V L-Edge X-Ray Absorption Spectra of V2O5 Using Local Pair Natural Orbital Coupled Cluster Theory and Spin-Orbit Coupled Configuration Interaction Approaches. *Phys. Chem. Chem. Phys.* **2013**, *15* (19), 7260−76.
(52) Tolhurst, T. M.; Leedahl, B.; Andrews, J. L.; Marley, P. M.; Banerjee, S.; Moewes, A. Contrasting 1d Tunnel-Structured and 2d Layered Polymorphs of V2O5: Relating Crystal Structure and Bonding to Band Gaps and Electronic Structure. *Phys. Chem. Chem. Phys.* **2016**, *18* (23), 15798−806.
(53) Scanlon, D. O.; Walsh, A.; Morgan, B. J.; Watson, G. W. An Ab Initio Study of Reduction of V2O5 through the Formation of Oxygen Vacancies and Li Intercalation. *J. Phys. Chem. C* **2008**, *112* (26), 9903−9911.
(54) Porsev, V. V.; Bandura, A. V.; Evarestov, R. A. Hybrid Hartree−Fock-Density Functional Theory Study of V2O5 Three Phases: Comparison of Bulk and Layer Stability, Electron and Phonon Properties. *Acta Mater.* **2014**, *75*, 246−258.
(55) Bhandari, C.; Lambrecht, W. R. L.; van Schilfgaarde, M. Quasiparticle Self-Consistentgwcalculations of the Electronic Band Structure of Bulk and MonolayerV2O5. *Phys. Rev. B* **2015**, *91* (12), No. 125116.
(56) Roginskii, E. M.; Smirnov, M. B.; Smirnov, K. S.; Baddour-Hadjean, R.; Pereira-Ramos, J.-P.; Smirnov, A. N.; Davydov, V. Y. A Computational and Spectroscopic Study of the Electronic Structure of V2O5-Based Cathode Materials. *J. Phys. Chem. C* **2021**, *125* (10), 5848−5858.
(57) Gershinsky, G.; Yoo, H. D.; Gofer, Y.; Aurbach, D. Electrochemical and Spectroscopic Analysis of Mg2+ Intercalation into Thin Film Electrodes of Layered Oxides: V2O5 and MoO3. *Langmuir* **2013**, *29* (34), 10964−10972.
(58) Pan, H.; Shao, Y.; Yan, P.; Cheng, Y.; Han, K. S.; Nie, Z.; Wang, C.; Yang, J.; Li, X.; Bhattacharya, P.; Mueller, K. T.; Liu, J. Reversible Aqueous Zinc/Manganese Oxide Energy Storage from Conversion Reactions. *Nat. Energy* **2016**, *1* (5), No. 16039.
(59) Dong, Y.; Jia, M.; Wang, Y.; Xu, J.; Liu, Y.; Jiao, L.; Zhang, N. Long-Life Zinc/Vanadium Pentoxide Battery Enabled by a Concentrated Aqueous Znso4 Electrolyte with Proton and Zinc Ion Co-Intercalation. *ACS Appl. Energy Mater.* **2020**, *3* (11), 11183−11192.
(60) Sai Gautam, G.; Canepa, P.; Abdellahi, A.; Urban, A.; Malik, R.; Ceder, G. The Intercalation Phase Diagram of Mg in V2O5 from First-Principles. *Chem. Mater.* **2015**, *27* (10), 3733−3742.
(61) Mitchell, J. B.; Geise, N. R.; Paterson, A. R.; Osti, N. C.; Sun, Y.; Fleischmann, S.; Zhang, R.; Madsen, L. A.; Toney, M. F.; Jiang, D.-e.; Kolesnikov, A. I.; Mamontov, E.; Augustyn, V. Confined Interlayer Water Promotes Structural Stability for High-Rate Electrochemical Proton Intercalation in Tungsten Oxide Hydrates. *ACS Energy Lett.* **2019**, *4* (12), 2805−2812.
(62) Fleischmann, S.; Sun, Y.; Osti, N. C.; Wang, R.; Mamontov, E.; Jiang, D.-e.; Augustyn, V. Interlayer Separation in Hydrogen Titanates Enables Electrochemical Proton Intercalation. *J. Mater. Chem A* **2020**, *8* (1), 412−421.
(63) Kim, S.; Shan, X.; Abeykoon, M.; Kwon, G.; Olds, D.; Teng, X. High-Capacity Aqueous Storage in Vanadate Cathodes Promoted by the Zn-Ion and Proton Intercalation and Conversion-Intercalation of Vanadyl Ions. *ACS Appl. Mater. Interfaces* **2021**, *13* (22), 25993−26000.
(64) Malik, R.; Abdellahi, A.; Ceder, G. A Critical Review of the Li Insertion Mechanisms in Lifepo4electrodes. *J. Electrochem. Soc.* **2013**, *160* (5), A3179−A3197.

https://doi.org/10.1021/acsaem.3c00830
ACS Appl. Energy Mater. XXXX, XXX, XXX−XXX

Manuscript published in The Journal of ACS Applied Energy Materials

(journal impact factor = 6.959)

(65) Yao, J.; Li, Y.; Massé, R. C.; Uchaker, E.; Cao, G. Revitalized Interest in Vanadium Pentoxide as Cathode Material for Lithium-Ion Batteries and Beyond. *Energy Storage Mater.* **2018**, *11*, 205−259.
(66) Huang, X.; Rui, X.; Hng, H. H.; Yan, Q. Vanadium Pentoxide-Based Cathode Materials for Lithium-Ion Batteries: Morphology Control, Carbon Hybridization, and Cation Doping. *Part. Part. Syst. Charact.* **2015**, *32* (3), 276−294.
(67) Lee, J. W.; Lim, S. Y.; Jeong, H. M.; Hwang, T. H.; Kang, J. K.; Choi, J. W. Extremely Stable Cycling of Ultra-Thin V2O5 Nanowire−Graphene Electrodes for Lithium Rechargeable Battery Cathodes. *Energy Environ. Sci.* **2012**, *5* (12), 9889−9894.
(68) Liu, X.; Zeng, J.; Yang, H.; Zhou, K.; Pan, D. V2O5-Based Nanomaterials: Synthesis and Their Applications. *RSC Adv.* **2018**, *8* (8), 4014−4031.
(69) McNulty, D.; Buckley, D. N.; O'Dwyer, C. Synthesis and Electrochemical Properties of Vanadium Oxide Materials and Structures as Li-Ion Battery Positive Electrodes. *J. Power Sources* **2014**, *267*, 831−873.
(70) Carrasco, J. Role of Van Der Waals Forces in Thermodynamics and Kinetics of Layered Transition Metal Oxide Electrodes: Alkali and Alkaline-Earth Ion Insertion into V2O5. *J. Phys. Chem. C* **2014**, *118* (34), 19599−19607.

มหาวิทยาลัยเทคโนโลยีสุรนารี

https://doi.org/10.1021/acsaem.3c00830
ACS Appl. Energy Mater. XXXX, XXX, XXX−XXX

Abstract submitted in The Siam Physics Congress 2022 (SPC2022)

S2 Condensed Matter Physics - Board: O-S2-19 / **309**

On the origin of high performance V2O5 cathodes of aqueous Mg-ion batteries: A computational study

Author: Panupol Untarabut[None]

Co-authors: Ittipon Fongkaew [1]; Anchalee Junkaew [2]; Sirisak Singsen [3]; Suwit Suthirakun [4]

[1] *School of Physics, Institute of Science, Suranaree University of Technology, Nakhon Rachasima, Thailand 30000*

[2] *National Nanotechnology Center (NANOTEC), National Science and Technology Development Agency (NSTDA), Pathum Thani 12120, Thailand*

[3] *School of Physics, Institute of Science, Suranaree University of Technology, Nakhon Ratchasima, Thailand 30000*

[4] *School of Chemistry, Institute of Science, Suranaree University of Technology, Nakhon Rachasima, Thailand 30000*

Corresponding Author: untarabut.p@gmail.com

Vanadium pentoxide (V2O5) is one of the promising cathode materials for Mg-ion batteries owing to its high capacity, safety, and low toxicity. However, it still suffers from sluggish charge transport kinetics and low stability. To overcome these problems, experiments reported that using aqueous electrolytes dramatically improves ion diffusion and capacity of V2O5-based cathode. Proton from water in the electrolyte may alter battery performance but its role remains unclear. Herein, we used density functional calculations to examine the effect of proton on the improved charge transfer properties and stability of Mg-proton co-intercalation to reveal the role of aqueous electrolyte. We find that protons prefer to intercalate into V2O5 and reside at vanadyl oxygen atoms. Upon proton intercalation, the band gap of V2O5 decreased from 2.17 eV to 0.07 eV suggesting better electronic conductivity. In addition, it improves Mg-ion diffusion where the diffusion barrier is reduced from 0.89 to 0.49 eV in the vicinity of intercalated proton. This work unravels the role of water in electrolyte in the enhanced cathode performance which could be used to better design cathode materials or electrolyte for Mg-ion batteries.

มหาวิทยาลัยเทคโนโลยีสุรนารี

CURRICULUM VITAE

Panupol Untarabut was born on September 10th, 1998 in Roi-et, Thailand. He received his B.Sc. in Physics (first-class honors) in 2020 from the Department of Physics, Faculty of Science, Khon Kaen University, Thailand. He has been granted a scholarship from the Development and Promotion of Science and Technology Talents Project (DPST, THAILAND) since 2017. During his bachelor's degree, he started research in computational materials science dealing with molecular dynamics simulation under the supervision of Assit. Prof. Dr. Kiettipong Banlusan. In 2021, he continued to pursue the master's degree program at the School of Physics, Suranaree University of Technology, Thailand with a DPST scholarship and National Research and Innovation Information System (NRIIS, THAILAND) under the supervision of Asst. Prof. Dr. Suwit Suthirakun and Dr. Ittipon Fongkeaw with research interest in density functional theory for materials investigation. He has published articles in international journals and participated in international conferences during the course of his master's program.

มหาวิทยาลัยเทคโนโลยีสุรนารี